



Simon Prato

Numerical Investigation of TEM Cells and Antenna Coupling

Master Thesis

Studies: Electrical Engineering

submitted to

Graz University of Technology

Supervisor

Dr. Thomas Bauernfeind



Graz, February 2025

Abstract

Electrically small antennas that conduct high-frequency signals often generate substantial electromagnetic emissions, presenting challenges for electromagnetic compatibility. Measurement of these emissions in a TEM cell remains a widely adopted and standardized procedure. In this thesis, a comprehensive theoretical framework is developed to explain the coupling mechanisms between the antenna and the TEM cell. The proposed framework is further supported and examined through detailed numerical analyses.

In the context of these investigations, special focus is laid on electric and magnetic dipole moments, which effectively characterize electrically small radiating sources. The magnitudes of these dipole moments accurately describe the electric and magnetic coupling independently. While established measurement-based methods with the TEM cell for determining these magnitudes exists, this thesis focuses on leveraging the finite element method to eliminate potential inaccuracies arising from the measurement setup and procedure. Furthermore, this study examines near-field shielding of the antennas and their equivalent dipole moments to determine shielding efficiency of materials with different properties.

The findings presented in this thesis contribute to a deeper understanding of how the geometrical and electrical characteristics of antennas influence their coupling behavior and, consequently, the generated dipole moments. This proves useful, for example, when aiming to increase electromagnetic compatibility of an electronic system containing electrically small conducting structures. Additionally, it demonstrates how the determination of equivalent dipole moments assist in the choice of shielding material.

Contents

1	Introduction	1
2	Dipole Theory	2
2.1	Electric Dipoles	2
2.1.1	Infinitesimal Electric Dipoles	2
2.1.2	Small Electric Dipoles	5
2.2	Magnetic Dipoles	6
2.3	Radiated Field	7
2.3.1	Field regions	8
2.3.2	Energy densities and reactances	10
3	Guided Waves	11
3.1	Lorentz Reciprocity Theorem	11
3.2	Green's Function	12
3.2.1	Scalar Green's Function	12
3.2.2	Dyadic Green's Function	13
3.3	Modes in Waveguides	15
3.3.1	Rectangular Waveguides as non-TEM structures	15
3.4	TEM mode in the TEM cell	16
3.4.1	Higher-order modes	18
3.4.2	Field distributions	20
3.5	Radiating Sources in TEM Cells	24
3.5.1	Arbitrary source	24
3.5.2	Equivalent dipole moments	26
3.5.3	Electrically small antennas	28
3.6	Shielding	30
3.6.1	Electromagnetic shielding mechanisms	30
3.6.2	Conductivity, permeability and permittivity in shields	32
3.6.3	ASTM ES7-83 Method	33
3.6.4	Dual TEM cell	34
4	Finite Element Method	35
4.1	Overview	35
4.2	Dividing a computational domain into finite elements	36
4.3	Solving the differential equation	37
4.4	Adaptive solution process	39
5	Numerical Investigations of Antennas in TEM Cells	39
5.1	Simulation Setup and Modeling Assumptions	39
5.1.1	Antenna models	39
5.1.2	TEM cell model	40
5.1.3	Dipole moment models	41
5.1.4	Mesh settings	42
5.1.5	Shielding material models	42
5.1.6	S-parameters and derived data	42

5.1.7	Investigation of Field Regions	44
5.2	Monopole Antenna	45
5.2.1	Setup	45
5.2.2	Equivalent dipole moments	46
5.2.3	Current distribution on septum	46
5.2.4	Feed voltage, current and impedance	47
5.2.5	Output power	49
5.2.6	Equivalent circuit model	50
5.3	Loop antenna	53
5.3.1	Setup	53
5.3.2	Equivalent dipole moments	53
5.3.3	Electrical characteristics	54
5.3.4	Equivalent circuit model	57
5.3.5	Current distribution on septum and higher order modes	58
5.3.6	Influence of antenna's geometry	61
5.4	Loop antenna with gap	62
5.4.1	Setup and geometrical analysis	62
5.4.2	Equivalent dipole moments	63
5.4.3	Electrical characteristics	63
5.5	Inverted-F and center-fed monopole antenna	66
5.5.1	Setup and geometrical analysis	66
5.5.2	Equivalent dipole moments	66
6	Application of Shielding Techniques in TEM Cells	67
6.1	ASTM ES7-83 method	67
6.2	Dual TEM cell	68
6.3	Antennas in shield enclosure	71
6.4	Dipole moments in shield enclosure	73
7	Conclusion	75

List of Figures

2.1	Geometrical arrangement of an infinitesimal electric dipole [3, p. 152].	3
2.2	The geometry of a linear, center-fed wire antenna is depicted with the feed-point located at its center. The feedpoint is represented by a small gap through which a current I_0 is supplied to the antenna [15, p. 417].	6
2.3	The current distribution along a linear wire antenna reaches its maximum at the feedpoint and decreases to zero at the endpoints, located at $d/2$ and $-d/2$ [3, p. 163].	7
2.4	The geometry of a current loop with radius b is shown, where the loop is fed with a current I_0 that generates a magnetic dipole moment \mathbf{m}_m . Alternatively, an equivalent magnetic dipole moment can be produced by a magnetic current I_m flowing perpendicular to the plane of the loop over a distance L	8
2.5	The behavior of Expression 1 and Expression 2 in (2.20) is analyzed as a function of distance r . Here, r is normalized to the radian distance $\lambda/2\pi$, and the magnitudes of both expressions are scaled to unity at the radian distance to facilitate comparison [3, p. 157].	9
2.6	Field regions of an antenna, here specifically a linear wire antenna, although they are applicable for any antenna with dimension d [3, p. 34].	10
3.1	The electric and magnetic fields corresponding to the first dominant TE and TM modes in a rectangular waveguide with perfectly conducting walls.	15
3.2	In this analysis, the Green's function determines the fields within the cross-sectional surface S of the TEM cell, which is shown in light gray and bounded by l . The source exciting these fields is a centrally located electric dipole moment, \mathbf{m}_e	17
3.3	Transverse electric field distributions in the cross section of the TEM cell. .	18
3.4	Geometrical arrangement of the TEM cell, demonstrated with cross sections in the xy -plane and the yz -plane.	19
3.5	Forward transmission coefficients S_{12} of the TEM, TE_{01} , and TE_{10} modes in the TEM cell over frequency.	19
3.6	Electric and magnetic field distributions of the TEM, TE_{01} , and TE_{10} modes in the TEM cell. The magnetic fields are shown along the full length of the cell, while the electric fields are shown at the ports only.	21
3.7	Output power and \mathbf{e}_{TEM}^{\pm} for different electric dipole moment positions and orientations.	23
3.8	The normalized electric field distribution \mathbf{e}_{TEM}^{\pm} in the TEM cell excited with an input power of $1/2$ W at a frequency of 3 GHz.	23
3.9	TEM cell with an arbitrary current source \mathbf{J}_1 along the line τ . \mathbf{E} and \mathbf{H} are the field intensities induced by the current. \mathbf{e}_n^+ and \mathbf{e}_n^- are outgoing fields towards both output ports of the TEM cell. \mathbf{S} indicates the surface, and V the volume of the domain in question.	24
3.10	Field distribution of the TEM mode highlighting the out-of-phase magnetic fields at the output ports.	27

3.11 Sketch of the surfaces S_0, S_1 and S_2 in the TEM cell with an example antenna, coupling through S_0 to the septum over the displacement current $\partial\mathbf{D}/\partial t$	29
3.12 Incident, reflected and transmitted electric field intensities at a shielding material.	31
3.13 Cross section of shielding material in TEM cell	34
3.14 Dual TEM cell with aperture	34
4.1 Tetrahedron with points on the edge and vertices.	36
4.2 Face of the finite element with unknowns	37
4.3 Adaptive solution process	39
5.1 Geometry of an antenna's feedpoint used in simulation. The antenna is fed through a round waveport of diameter 0.46 mm and consists of a PEC wire with a diameter of 0.2 mm. This geometry leads to a reference impedance of $Z_0 \approx 50 \Omega$	40
5.2 Circuit representing the TEM cell, where the capacitance and inductance are split into two separate, equal components $C_T = C_{T1} + C_{T2}$, $L_T = L_{T1} + L_{T2}$ and $C_{T1} = C_{T2}$, $L_{T1} = L_{T2}$. The resistances R_1, R_2 at the output ports model the reference impedance $Z_w \approx 50 \Omega$	41
5.3 Numerical model of a TEM cell containing an electric moment \mathbf{m}_e and a magnetic dipole moment \mathbf{m}_m positioned at the center ($x = 0, y = r = b/4, z = 0$). This setup is used to investigate the specific field regions in which coupling occurs.	44
5.4 Comparison of coupling behavior: (a) The normalized output power produced by dipole moments in the large versus the small TEM cell, and (b) the dipole moments used as the source. The congruence of the power curves demonstrates that the coupling is independent of the cell dimensions.	45
5.5 The geometrical aspects of the cylindrical monopole antenna, as implemented in the simulation model, with the respective electric near-field plot.	46
5.6 The equivalent electric and magnetic dipole moments analytically calculated with Equations (3.46a) to (3.46b). To enable direct comparison with the magnetic dipole moment, the electric dipole moment is weighted with the free space impedance Z_0 , as discussed in subsubsection 5.1.3.	47
5.7 Current surface densities at different frequencies, below and above the cut-off frequency of the TE_{01} -mode.	48
5.8 Magnitude of the voltage and current applied at the feedpoint of the monopole antenna over frequency, derived through the S-parameters with Equations (5.4) to (5.5), with the respective magnitude and phase of the antenna impedance over frequency, derived through the S-parameters with Equation 5.6.	49
5.9 Current distribution at 3 GHz	50
5.10 Current distribution at 1 MHz	50
5.11 The current distribution along the monopole antenna at 3 GHz and 1 MHz.	50
5.12 Electric field in y-direction E_y at $x = 0, y = b/4, z = \pm l/2$, and power at one output port, derived with the S-parameters in Equation 5.2. The output power produced by the monopole antenna is compared to the output power produced by the equivalent dipole moments, to demonstrate validity of the model.	50

5.13	Equivalent circuit for a short electric dipole models the monopole antenna's behavior.	51
5.14	Model of the monopole antenna connected to a feedpoint mounted on a PEC surface with a side length of $\lambda/2$, where λ corresponds to the free-space wavelength of the solution frequency. This configuration enables the investigation of the monopole antenna reactance without influence of the TEM cell.	52
5.15	Circuit representing the TEM cell and the monopole antenna, with the additional components C_k and $M_{A,T1}$, $M_{A,T2}$ modeling their near-field coupling behavior.	52
5.16	Equivalent dipole moments derived by the equivalent circuit depicted in Figure 5.2, compared to the derived dipole moments of the monopole antenna, shown in Figure 5.6. The electric dipole moment \mathbf{m}_e is weighted with η_0 for comparison purposes.	53
5.17	The geometry of the loop antenna assimilates a square with round edges. The height and width of the antenna equal $h = w = 1.6$ mm. The return path leads back to the PEC surface of the TEM cell. The electric near-field shows large a displacement current and voltage drop near the feed-point. It has been derived with a refined mesh on the antenna surface and near the feedpoint, according to the discussion in Section 5.1.4.	54
5.18	The equivalent dipole moments of the loop antenna are derived analytically with Equations (3.46a) to (3.46b), where the electric dipole moment \mathbf{m}_e is weighted with Z_0 to enable comparison with \mathbf{m}_m . The phases of the powers at output ports 1 and 2 are derived from the S-parameters, as discussed in Section 5.1.6. The analysis specifically focuses on the phase shift between the two ports, which provides information about the presence of \mathbf{m}_m and \mathbf{m}_e , as investigated in Section 3.5.2.	55
5.19	Electric field in y-direction E_y at $x = 0, y = b/4, z = \pm l/2$, and the closely related power at one of the output ports, derived with the S-parameters in Equation 5.2. The output power produced by the loop antenna is compared with that generated by the equivalent dipole moments.	55
5.20	Electric and magnetic energy produced by the loop antenna in the TEM cell, derived with Equation 2.24 in the TEM cell volume.	56
5.21	This figure demonstrates the voltage, current and impedance characteristics of the loop antenna. The difference between the current near the feedpoint and that on the return path increases with frequency, indicating a growing occurrence of displacement currents. The current on those paths are determined through magnetic near-field intensity, using Equation 5.8. The voltage across the feedpoint is obtained using Equation 5.5. Magnitude and phase of the impedance of the loop antenna are determined with Equation 5.6.	56
5.22	Equivalent circuits of the small loop antenna.	57
5.23	Model of the loop antenna connected to a feedpoint mounted on a PEC surface with a side length of $\lambda/2$, where λ corresponds to the free-space wavelength of the solution frequency. This configuration enables the investigation of the loop antenna reactance without influence of the TEM cell.	58

5.24	Circuit representing the TEM cell and the loop antenna, with the additional components C_k and $M_{A,T1}$, $M_{A,T2}$ modeling their near-field coupling behavior.	58
5.25	Equivalent dipole moments derived by the equivalent circuit depicted in Figure 5.24, compared to the dipole moments of the loop antenna, shown in Figure 5.18a. The electric dipole moment \mathbf{m}_e is weighted with η_0 for comparison purposes.	59
5.26	Surface current density on the septum induced by the loop antenna for different frequencies and positions of the antenna.	60
5.27	Output power transmitted by the antenna to the output port through the TEM and TE_{01} modes, separately over frequency, determined through the S-parameters with Equation 5.2. At a frequency of $f = 3.21$ GHz a resonance in the TEM cell occurs, leading to the visible peak in the output power produced by the TE_{01} mode.	61
5.28	Dipole moments and output power comparisons of two different loop antenna configurations presented, one with $h = 2.16$ mm, $w = 1.4$ mm and the other with $h = 1.2$ mm, $w = 2.36$ mm. The electric dipole moment \mathbf{m}_e is weighted with Z_0 for comparison purposes.	62
5.29	Geometry of the loop antenna with a gap in the return path inserted in the TEM cell. The gap height is exaggerated for demonstration purposes.	63
5.30	The equivalent dipole moments of the loop antenna with a gap, where the electric dipole moment \mathbf{m}_e is weighted with Z_0 to enable comparison with \mathbf{m}_m . The phases of the powers at output ports 1 and 2 are derived from the S-parameters, as discussed in Section 5.1.6. The analysis specifically focuses on the phase shift between the two ports, which provides information about the presence of \mathbf{m}_m and \mathbf{m}_e , as investigated in Section 3.5.2.	64
5.31	Comparison of dipole moments, where the electric dipole moment \mathbf{m}_e is weighted with η_0 to enable comparison with \mathbf{m}_m , and output power for different gap heights in the loop antenna.	65
5.32	The voltage and current across the feedpoint, together with the related impedance of the loop antenna with gap.	65
5.33	Geometries of IFA and CFM antenna, together with their equivalent dipole moments. the electric dipole moment \mathbf{m}_e is weighted with the free space impedance Z_0 to enable comparison with the magnetic dipole moment \mathbf{m}_m	66
6.1	Shielding effectiveness of a thin sheet of ferrite, barium titanate, and silver as a function of frequency, determined using the ASTM ES7-83 method.	68
6.2	The sum $P_{\text{ref,sum}}$ and difference $P_{\text{ref,diff}}$ of the reference power, measured with an empty aperture and calculated with phase information considered.	69
6.3	The sum $P_{\text{load,sum}}$ and difference $P_{\text{load,diff}}$ of the output power measured at ports 3 and 4 with phase information considered.	70
6.4	Electric SE_{dB}^e and magnetic SE_{dB}^m shielding effectiveness of (a) silver and (b) barium titanate and ferrite, derived according to (3.68a) and (3.68b).	70
6.5	Investigated antennas placed inside a hollow cubic enclosure within the TEM cell.	71
6.6	Radiated power as a function of frequency for the loop and monopole antennas with and without enclosure.	72

6.7	Radiated power as a function of frequency for the loop and monopole antennas with varying enclosure wall thickness.	73
6.8	Electric near-field distribution of the loop antenna at the resonance frequency of 2.5 GHz, with a barium titanate shielding enclosure of 100 μm wall thickness.	73
6.9	Radiated power as a function of frequency for the loop and monopole antenna equivalent dipole moments in enclosures of different materials at a constant wall thickness of 10 μm	74

List of Tables

3.1	Cutoff frequencies of the TE ₀₁ and TE ₁₀ modes for different TEM cell dimensions, derived both through numerical simulation and analytical calculation. The results of these separate methods agree within the precision shown. As expected from (3.27), the TE ₁₀ cutoff frequency depends only on a and is independent of b , consistent with rectangular waveguide theory. The TE ₀₁ cutoff frequency varies with both a and b .	20
6.1	Electromagnetic properties of ferrite, barium titanate, and silver.	67

1 Introduction

In recent years, electronic systems have demonstrated a clear trend toward reduced physical dimensions and increased operating speeds, consequently, higher frequencies are used. As a result, these systems often contain small conducting structures that carry currents and voltages with high amplitudes and frequencies. These structures tend to radiate and are susceptible to electromagnetic radiation, behaving as antennas and causing electromagnetic compatibility (EMC) issues.

Taking EMC into account during the design of electronic systems helps to minimize additional costs and schedule delays that may arise from potential redesigns. Furthermore, it ensures that the product operates reliably when exposed to interference from external sources [29, p. 64]. Consequently, research focusing on all aspects of EMC is conducted regularly. This thesis aims to contribute to these ongoing investigations, specifically through analysis of the previously mentioned small antennas and their coupling behavior in TEM cells. TEM cells are included because they provide a standardized method for measuring electromagnetic emissions under approximate free-space conditions and have been widely used for testing small devices [10, 19, 12].

Several studies have analyzed the coupling behavior of small antennas and devices with TEM cells [32, 22]. Specifically, [21, 20, 36] implement electric and/or magnetic dipole moments to model the radiated fields of such antennas, which provide information about the electric and magnetic coupling with the TEM cell, respectively. The magnitudes of the dipole moments are found by measurements with the TEM cell [32] or numerical analysis [20]. This thesis treats the coupling behavior of small antennas modeled with dipole moments using the latter approach, namely numerical computation using the finite element method. The advantage of this approach is the absence of inaccuracies caused by the measurement setup or related uncertainties, allowing the analysis to focus on the underlying mechanics behind the coupling behavior.

This thesis aims to explain how the electric and magnetic dipole moments of antennas are created and what factors affect them. Understanding this helps design electronic devices that meet EMC requirements and achieve specific coupling behaviors. Additionally, replacing the small antennas with their equivalent dipole moments significantly reduces computational effort, which is particularly advantageous when dealing with large computational domains.

Furthermore, this thesis investigates the shielding efficiency of different materials in the presence of dipole moments. The performance of the shielding material with respect to the electric and magnetic coupling behavior of the antennas, as reflected by the dipole moments, is investigated. The results assist in the selection of appropriate shielding material to effectively reduce emissions produced by the antennas.

To achieve these objectives, this thesis first presents the theoretical foundations of electric and magnetic dipole moments in Section 2. The behavior of electromagnetic waves generated by arbitrary sources in waveguides, specifically the TEM cell, is then discussed in Section 3. Further, background information of electromagnetic shielding and methods to determine shielding effectiveness using the TEM cell are presented. A brief overview of

the finite element method is provided in Section 4.

Subsequently, Section 5 addresses the numerical modeling of antennas and the TEM cell and investigates the generation of electric and magnetic dipole moments for monopole and loop antennas using the theoretical framework developed earlier. This knowledge is applied to three additional antennas, whose analysis delivers results closely related to that of the monopole and loop antennas due to their shared predominantly inductive or capacitive characteristics, which emerge as the primary distinction in the antenna coupling behavior. Equivalent circuits to model capacitive and inductive antennas, together with the TEM cell and their coupling paths, are developed, from which the dipole moments can be investigated in more detail.

Section 6 demonstrates the application of shielding materials in numerical simulations involving dipole moments and electrically small antennas. Lastly, section 7 presents the conclusions and discussion derived from this thesis, along with potential directions for future research.

2 Dipole Theory

2.1 Electric Dipoles

2.1.1 Infinitesimal Electric Dipoles

An electric dipole can be modeled as two tiny charged metal spheres [11, p. 467], or alternatively two capacitor-plates [3, p. 151], connected with a linear wire of length d and diameter a . The charges accelerate along the wire and radiate. In case of an ideal, infinitesimal dipole, the wire is very thin ($a \ll \lambda$) and very small ($d \ll \lambda$) compared to the wavelength λ [3, p. 151, 11, p. 468]. For an antenna to be accurately modeled as an infinitesimal electric dipole, its length must be smaller than a fiftieth of the wavelength ($d < \lambda/50$) [3, p. 156]. They are not very practical, but serve as a basic building block for more complex geometries, or as an excitation source in numerical investigations.

An infinitesimal electric dipole, illustrated in Figure 2.1, is analyzed in detail below. The dipole is aligned with the z -axis, which simplifies the following mathematical investigations. Time variation according to $e^{-j\omega t}$ is assumed and therefore omitted in this thesis. A current flows in the wire, which is spatially uniform throughout the wire. This is expressed as [3, p. 151]

$$\mathbf{I}(z) = \hat{\mathbf{a}}_z I_0. \quad (2.1)$$

To permit a constant current across the wire, which is otherwise physically impossible, capacitor plates are modeled at its ends. The electric dipole moment can be expressed as

$$\mathbf{m}_e = I_0 d \cdot \hat{\mathbf{a}}_z. \quad (2.2)$$

Next, the vector potential \mathbf{A} is determined through

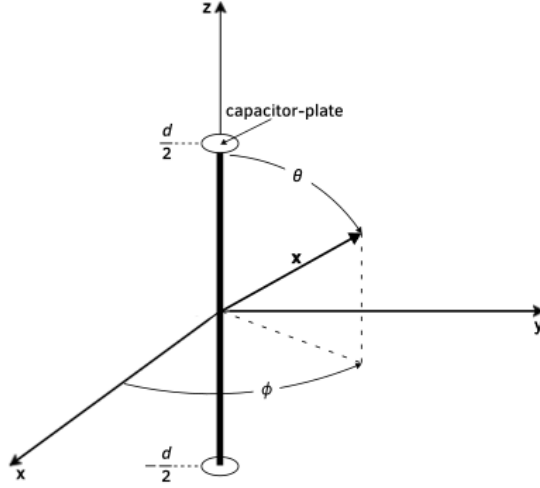


Figure 2.1 Geometrical arrangement of an infinitesimal electric dipole [3, p. 152].

$$\mathbf{A}(\mathbf{x}) = \frac{\mu}{4\pi} \frac{e^{-jkr}}{r} \iiint_V \mathbf{J}(\mathbf{x}') dv', \quad (2.3)$$

where

\mathbf{x}	observation point coordinates $\hat{\mathbf{a}}_x x + \hat{\mathbf{a}}_y y + \hat{\mathbf{a}}_z z$,
\mathbf{x}'	source point coordinates $\hat{\mathbf{a}}_x x' + \hat{\mathbf{a}}_y y' + \hat{\mathbf{a}}_z z'$,
\mathbf{J}	current density in the source region,
r	distance from source to observation point $ \mathbf{x} - \mathbf{x}' $,
μ	permeability of the medium,
$k = 2\pi/\lambda$	wavenumber,
e^{-jkr}	phase factor describing the wave propagation with distance.

For the infinitesimal dipole, the source is located at the origin, so $\mathbf{x}' = \mathbf{0}$ [3, p. 152]. Since the wire is assumed very thin, the volume integral in (2.3) reduces to a line integral along the dipole axis. With the constant current distribution given in (2.12), I_0 can be pulled out of the integral. Evaluating the remaining integral over the dipole length d yields [3, p. 153]

$$\begin{aligned} \mathbf{A}(\mathbf{x}) &= \hat{\mathbf{a}}_z \frac{\mu I_0}{4\pi r} e^{-jkr} \int_{-d/2}^{+d/2} dz' \\ &= \hat{\mathbf{a}}_z \frac{\mu I_0 d}{4\pi r} e^{-jkr}. \end{aligned} \quad (2.4)$$

All other field quantities can be derived from the vector potential \mathbf{A} , such as the electric field intensity \mathbf{E} and magnetic field intensity \mathbf{H} . To simplify this process, the Cartesian components of \mathbf{A} are first transformed into spherical ones. This transformation is given in matrix form as [3, p. 153]

$$\begin{bmatrix} A_r \\ A_\theta \\ A_\phi \end{bmatrix} = \begin{bmatrix} \sin \theta \cos \phi & \sin \theta \sin \phi & \cos \theta \\ \cos \theta \cos \phi & \cos \theta \sin \phi & -\sin \theta \\ -\sin \phi & \cos \phi & 0 \end{bmatrix} \begin{bmatrix} A_x \\ A_y \\ A_z \end{bmatrix}, \quad (2.5)$$

where θ is the polar angle and ϕ is the azimuthal angle of the observation point \mathbf{x} . \mathbf{E} and \mathbf{H} are then expressed by [3, p. 153],

$$\mathbf{H} = \frac{1}{\mu r} \left[\frac{\partial}{\partial r} (r A_\theta) - \frac{\partial A_r}{\partial \theta} \right] \hat{\mathbf{a}}_\phi, \quad (2.6a)$$

$$\mathbf{E} = -j\omega \mathbf{A} - j \frac{1}{\omega \mu \epsilon} \nabla (\nabla \cdot \mathbf{A}). \quad (2.6b)$$

Substituting (2.4) into (2.6a) yields

$$H_r = H_\theta = 0, \quad (2.7a)$$

$$H_\phi = j \frac{k I_0 d \sin \theta}{4\pi r} \left[1 + \frac{1}{jkr} \right] e^{-jkr}, \quad (2.7b)$$

and substituting into Equation (2.6b) yields

$$E_r = \eta \frac{I_0 d \cos \theta}{2\pi r^2} \left[1 + \frac{1}{jkr} \right] e^{-jkr}, \quad (2.8a)$$

$$E_\theta = j\eta \frac{k I_0 d \sin \theta}{4\pi r} \left[1 + \frac{1}{jkr} - \frac{1}{(kr)^2} \right] e^{-jkr}, \quad (2.8b)$$

$$E_\phi = 0, \quad (2.8c)$$

where $\eta = \sqrt{\frac{\mu}{\epsilon}}$ is the wave impedance of the medium in which the waves travel.

The total radiated power of the dipole is obtained by integrating the complex Poynting vector \mathbf{S} over a closed surface surrounding the dipole [3, p. 154]. The real part of the total radiated power provides information about energy transferred by radiation, while the imaginary part about the antenna's reactive behavior. \mathbf{S} is defined by

$$\mathbf{S} = \frac{1}{2} (\mathbf{E} \times \mathbf{H}^*). \quad (2.9)$$

The real power transfer is derived through the time-averaged Poynting vector \mathbf{S}_{av} [3, p. 160], which is calculated by

$$\mathbf{S}_{av} = \frac{1}{2} \Re \{ \mathbf{E} \times \mathbf{H}^* \}. \quad (2.10)$$

The complex power P is derived by integrating \mathbf{S} over a closed surface around the dipole, which leads to [3, p. 154]

$$P_r = \eta \frac{\pi}{3} \frac{|I_0 l|^2}{\lambda} \left[1 - j \frac{1}{(kr)^3} \right]. \quad (2.11)$$

The imaginary part of the power radiated by the infinitesimal electric dipole shows capacitive behavior, as demonstrated by (2.11).

2.1.2 Small Electric Dipoles

Wires that are too long to be modeled as infinitesimal dipoles, but short enough to be considered electrically small ($\lambda/50 < l \leq \lambda/10$), are classified as small physical dipoles [3, pp. 162-163]. These dipoles provide a more accurate and practical representation of linear wire antennas, and are examined in greater detail below.

A current I_0 is fed into the short, center-fed, linear antenna shown in Figure 2.1. The current along the antenna arms $I(z)$ linearly drops to zero [15, p. 412], as visualized in Figure 2.3. Mathematically, it is described by,

$$\mathbf{I}(z) = I_0 \left(1 - \frac{2|z|}{d} \right) \cdot \hat{\mathbf{a}}_z. \quad (2.12)$$

This current distribution differs from that of the infinitesimal dipole, and as a result, the capacitor plates are not required in this model. Additionally, charge accumulates along the antenna due to the linear decrease in current \mathbf{I} . This accumulation is characterized by the charge per unit length, ρ' , which is appropriate for a thin wire. The relationship is derived from the continuity equation, $\partial\rho/\partial t = -\nabla \cdot \mathbf{J}$. In the frequency domain, this becomes $j\omega\rho = -\nabla \cdot \mathbf{J}$. Substituting this into (2.12) yields [15, pp. 410-412].

$$\rho' = \pm \frac{d}{dz} j \frac{I(z)}{\omega} = \pm j \frac{2I_0}{\omega d}. \quad (2.13)$$

ρ' is uniformly distributed along each antenna arm.

Next, the vector potential \mathbf{A} is determined using (2.3). The calculations of \mathbf{A} simplify to [15, p. 410],

$$\mathbf{A}(\mathbf{x}) = \hat{\mathbf{a}}_z \frac{\mu I_0 d}{8\pi r} e^{-jkr} \quad (2.14)$$

The formulation of \mathbf{A} now includes an additional factor of 1/2 compared to the previously derived expression for infinitesimal dipoles in (2.4). This factor arises from the integration of \mathbf{I} : when integrated over the interval $[-d/2, d/2]$, a linearly decreasing \mathbf{I} yields half the value obtained from a constant \mathbf{I} . For the same reason, the electric dipole moment \mathbf{m}_e is also reduced to half of that in (2.2).

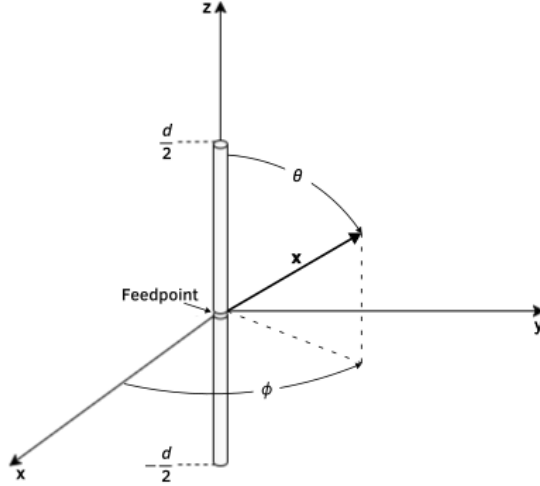


Figure 2.2 The geometry of a linear, center-fed wire antenna is depicted with the feedpoint located at its center. The feedpoint is represented by a small gap through which a current I_0 is supplied to the antenna [15, p. 417].

Furthermore, for the sake of simplicity, it is reasonable to set $\mathbf{x}' = \mathbf{0}$. This approximation has been shown to be sufficient for large r , with the resulting amplitude error remaining negligible even for small r [15, p. 409, 3, pp. 164-168].

The short physical electric dipole described in this section serves as an approximation for the behavior of electrically short antennas. Particular attention must be paid to the excitation method and physical shape, as these factors significantly influence antenna behavior [15, p. 413]. Furthermore, any antenna analyzed using this approach should remain much smaller than the wavelength λ to minimize analytical approximation errors.

2.2 Magnetic Dipoles

The magnetic dipole moment characterizes the strength of a magnetic source. An electrically small current loop fed with a current I_0 can be used to model the magnetic dipole, as demonstrated in Figure 2.4. This approximation is valid provided the overall loop circumference satisfies $2\pi b < \lambda/10$ and the wire is assumed very thin [3, p. 231]. Furthermore, the radiation pattern of the magnetic dipole is equal to that of the electric dipole, with the role of the electric and magnetic fields interchanged [11, p. 254].

The magnetic dipole moment \mathbf{m}_m is given by

$$\mathbf{m}_m = I_m L \cdot \hat{\mathbf{a}}_z. \quad (2.15)$$

Furthermore, the magnetic current I_m and the electric current I_0 in the loop are related with [3, p. 237]

$$I_m L = j A \omega \mu_0 I_0 \quad (2.16)$$

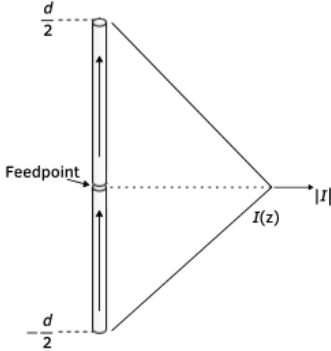


Figure 2.3 The current distribution along a linear wire antenna reaches its maximum at the feedpoint and decreases to zero at the endpoints, located at $d/2$ and $-d/2$ [3, p. 163].

with $A = \pi b^2$ denoting the area of the current loop. Analogous to the separation distance d in the electric dipole, L is the length of the magnetic dipole. The electric and magnetic field intensities \mathbf{E} and \mathbf{H} produced by the dipole and current loop are the same. Thus, the infinitesimal magnetic dipole $I_m L$ and the electrically small current loop $jA\omega\mu_0 I_0$ are equivalent representations [3, p. 237]. The electric field intensity \mathbf{E} of the magnetic dipole is given by

$$E_r = E_\theta = 0, \quad (2.17a)$$

$$E_\phi = -j \frac{k I_m L \sin \theta}{4\pi r} \left[1 + \frac{1}{jkr} \right] e^{-jkr}, \quad (2.17b)$$

and the magnetic field intensity by [3, p. 237]

$$H_r = \frac{I_m L \cos \theta}{2\pi r^2 \eta} \left[1 + \frac{1}{jkr} \right] e^{-jkr}, \quad (2.18a)$$

$$H_\theta = j \frac{k I_m L \sin \theta}{4\pi r \eta} \left[1 + \frac{1}{jkr} - \frac{1}{(kr)^2} \right] e^{-jkr}, \quad (2.18b)$$

$$H_\phi = 0. \quad (2.18c)$$

The complex power density \mathbf{S} can be derived following the same approach as for the electric dipole (see (2.9)). For the magnetic dipole, the imaginary part of \mathbf{S} has the opposite sign compared to the electric dipole. This is the result of the near-field power being inductive in case of the magnetic dipole, while it is capacitive for the electric dipole. The complex power equals [3, p. 238]

$$P_r = \eta \left(\frac{\pi}{12} \right) (kb)^4 |I_0|^2 \left[1 + j \frac{1}{(kr)^3} \right]. \quad (2.19)$$

2.3 Radiated Field

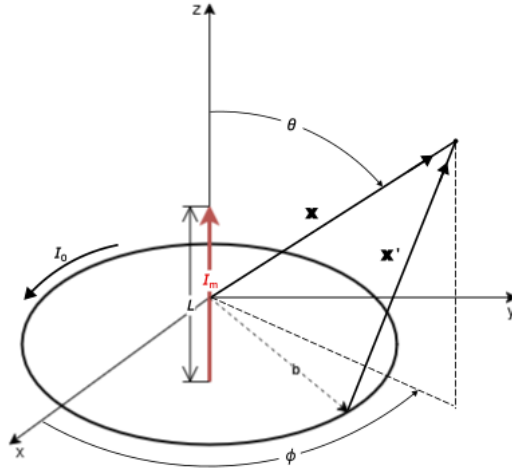


Figure 2.4 The geometry of a current loop with radius b is shown, where the loop is fed with a current I_0 that generates a magnetic dipole moment \mathbf{m}_m . Alternatively, an equivalent magnetic dipole moment can be produced by a magnetic current I_m flowing perpendicular to the plane of the loop over a distance L .

2.3.1 Field regions

This section investigates the field regions of the radiated fields, beginning with the infinitesimal electric dipole, from which the analysis extends analogously to magnetic dipoles. The field quantities \mathbf{E} and \mathbf{H} derived in (2.7) and (2.8) demonstrate that the behavior of the fields depends on the distance r from the dipole [3, p. 156]. This dependence is governed by the terms $1/(jkr)$ and $1/(kr)^2$, which are highlighted for clarity in the expression for E_θ :

$$E_\theta = j\eta \frac{kI_0 d \sin \theta}{4\pi r} \left[1 + \underbrace{\frac{1}{jkr}}_{\text{Expression 1}} - \underbrace{\frac{1}{(kr)^2}}_{\text{Expression 2}} \right] e^{-jkr}, \quad (2.20)$$

where $1/(jkr)$ also appears in E_r and H_ϕ , while $1/(kr)^2$ appears only in E_θ . The variation of Expression 1 and Expression 2 with distance is shown in Figure 2.5.

If the distance $r < \lambda/2\pi$ (or equivalently, $kr < 1$), then Expression 2 dominates over the other terms. Consequently, the energy stored in this region is predominantly imaginary. This region is referred to as the near-field region [3, pp. 156-157].

At distances $r > \lambda/2\pi$ ($kr > 1$), Expression 1 exceeds Expression 2 in magnitude, such that the real part of the energy exceeds the imaginary part. This region is referred to as the intermediate-field region [3, p. 157].

At large distances $r \gg \lambda/2\pi$ ($kr \gg 1$) the energy is predominantly real, reflecting radiated energy propagating outward. This region is referred to as the far-field region [3, p. 157].

At $r = \lambda/2\pi$ ($kr = 1$), Expression 1 and Expression 2 attain equal magnitudes, a distance referred to as the radian distance [3, pp. 156-160]. The radian distance thus represents a critical transition between field regions, as shown in Figure 2.5.

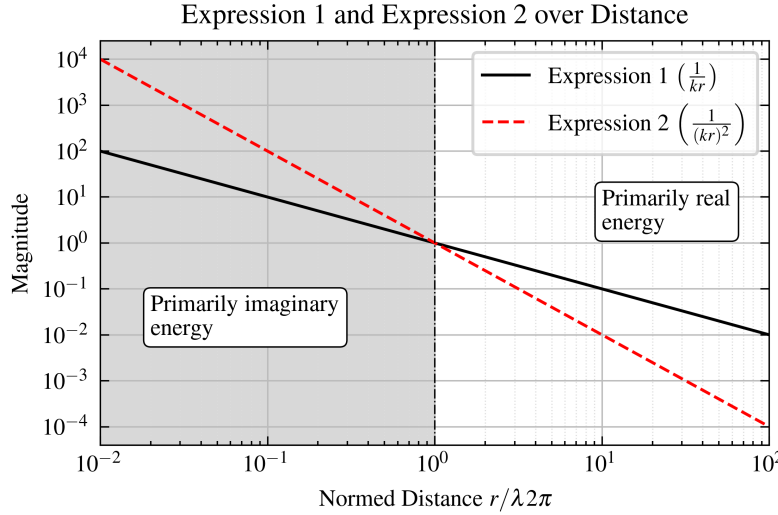


Figure 2.5 The behavior of Expression 1 and Expression 2 in (2.20) is analyzed as a function of distance r . Here, r is normalized to the radian distance $\lambda/2\pi$, and the magnitudes of both expressions are scaled to unity at the radian distance to facilitate comparison [3, p. 157].

For antennas that cannot be approximated as electrically small, the field region boundaries depend on the antenna's physical dimensions rather than the wavelength alone. The regions for such an antenna are shown in Figure 2.6.

The radiating near-field occurs at distances larger than approximately r_1 and the far-field region at approximately r_2 , which are defined as [3, p. 34]

$$r_1 = 0.62\sqrt{d^3/\lambda}, \quad (2.21a)$$

$$r_2 = 2d^2/\lambda, \quad (2.21b)$$

where d is the largest dimension of the antenna.

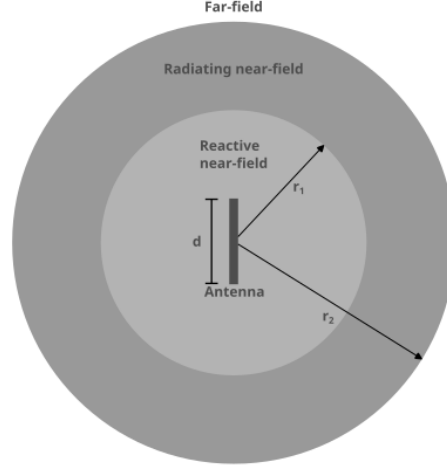


Figure 2.6 Field regions of an antenna, here specifically a linear wire antenna, although they are applicable for any antenna with dimension d [3, p. 34].

2.3.2 Energy densities and reactances

The electric energy density w_e is defined as

$$w_e = \frac{1}{2} \mathbf{E} \cdot \mathbf{D}, \quad (2.22)$$

while the magnetic energy density w_m is given by

$$w_m = \frac{1}{2} \mathbf{B} \cdot \mathbf{H}. \quad (2.23)$$

By applying the constitutive relations $\mathbf{D} = \epsilon \mathbf{E}$ and $\mathbf{B} = \mu \mathbf{H}$, and summing the contributions from (2.22) and (2.23), the total electromagnetic energy density w_{em} is obtained with [11, p. 330]

$$w_{\text{em}} = \frac{1}{2} \left(\underbrace{\epsilon E^2}_{\text{Electric energy } w_e} + \underbrace{\frac{1}{\mu} B^2}_{\text{Magnetic energy } w_m} \right). \quad (2.24)$$

Integrating w_{em} over a given volume yields the total electromagnetic energy W_{em} contained within that region. Similarly, integrating w_e provides the total electric energy W_e , and integrating w_m gives the total magnetic energy W_m .

The reactance of an electrically short antenna is directly related to the electric and magnetic energy densities, w_e and w_m . Therefore, the electric and magnetic energy stored can be represented by a lumped capacitor and inductor, respectively. This antenna's equivalent inductance and capacitance can be determined using the relationships [11, pp. 107, 328]

$$L = 2 \frac{W_m}{I^2}, \quad (2.25a)$$

$$C = 2 \frac{W_e}{V^2}, \quad (2.25b)$$

where V and I denote the terminal voltage and current.

3 Guided Waves

3.1 Lorentz Reciprocity Theorem¹

Let two source pairs $\mathbf{J}_1, \mathbf{M}_1$ and $\mathbf{J}_2, \mathbf{M}_2$ exist in a volume V , bounded by the closed surface S . The medium in V is linear and isotropic. The source pairs generate fields $\mathbf{E}_1, \mathbf{H}_1$ and $\mathbf{E}_2, \mathbf{H}_2$, respectively, with the same frequency. The fields and source pairs can then be related with [3, p. 145, 8, p. 49]

$$-\nabla \cdot (\mathbf{E}_1 \times \mathbf{H}_2 - \mathbf{E}_2 \times \mathbf{H}_1) = \mathbf{E}_1 \cdot \mathbf{J}_2 + \mathbf{H}_2 \cdot \mathbf{M}_1 - \mathbf{E}_2 \cdot \mathbf{J}_1 - \mathbf{H}_1 \cdot \mathbf{M}_2. \quad (3.1)$$

Integrating Equation 3.1 over V , and converting the volume integral to a surface integral with the divergence theorem, leads to [3, p. 145, 8, p. 50]

$$\begin{aligned} & -\oint\int_S (\mathbf{E}_1 \times \mathbf{H}_2 - \mathbf{E}_2 \times \mathbf{H}_1) \cdot d\mathbf{s}' \\ &= \iiint_V (\mathbf{E}_1 \cdot \mathbf{J}_2 + \mathbf{H}_2 \cdot \mathbf{M}_1 - \mathbf{E}_2 \cdot \mathbf{J}_1 - \mathbf{H}_1 \cdot \mathbf{M}_2) \cdot dv'. \end{aligned} \quad (3.2)$$

This integral equation relates the coupling of different source points. Additionally, if one of these sources is set to zero, the respective source point can serve as an observation point. Setting all sources to zero allows investigation of the coupling of modal fields in a waveguide to other modes, as the following example shows. Suppose the volume V does not contain sources $\mathbf{J}_1 = \mathbf{M}_1 = \mathbf{J}_2 = \mathbf{M}_2 = \mathbf{0}$. Then, the source-free Lorentz Reciprocity theorem reduces to the condition that the modes in the waveguide must fulfill [3, pp. 145-146]:

$$\nabla \cdot (\mathbf{E}_1 \times \mathbf{H}_2 - \mathbf{E}_2 \times \mathbf{H}_1) = 0, \quad (3.3a)$$

$$\oint\int_S (\mathbf{E}_1 \times \mathbf{H}_2 - \mathbf{E}_2 \times \mathbf{H}_1) \cdot d\mathbf{s}' = 0. \quad (3.3b)$$

Another application arises when investigating a volume V confined by a perfectly conducting surface S , in which the linear current densities \mathbf{J}_1 and \mathbf{J}_2 flow. Because $\mathbf{n} \times \mathbf{E}_1 = \mathbf{n} \times \mathbf{E}_2 = 0$ along the surface S , the surface integral in Equation 3.2 vanishes, leading to

¹This section follows closely the treatment in: Robert E. Collin, *Field Theory of Guided Waves*, IEEE Press, 2015 and Constantine A. Balanis, *Antenna theory: Analysis and design*, Wiley, 1997.

$$\mathbf{E}_1 \cdot \mathbf{J}_2 = \mathbf{E}_2 \cdot \mathbf{J}_1. \quad (3.4)$$

This is the Rayleigh-Carson form of the Lorentz reciprocity theorem [8, p. 50]. It states that the component of \mathbf{E}_1 along \mathbf{J}_2 is equal to the component of \mathbf{E}_2 along \mathbf{J}_1 , and vice versa [8, p. 50].

In summary, the Lorentz Reciprocity theorem is useful for deriving reciprocal aspects of waveguides, finding orthogonal properties of modes, investigating fields generated by currents and dipole moments in waveguides [8, p. 50], among several other examples. This theorem will be employed often throughout the remainder of this thesis.

3.2 Green's Function²

3.2.1 Scalar Green's Function

The Green's function describes the response of a linear differential operator L to a point source of unit strength. It is briefly introduced here through an example of solving Poisson's equation with boundary conditions, as this concept will be applied in later analysis. The general form for a Green's function of a given problem is [1, p. 512]

$$LG(\mathbf{x}, \mathbf{x}') = -\delta(\mathbf{x} - \mathbf{x}'). \quad (3.5)$$

A point source of unit strength is generally modeled with a delta function δ at a certain point in one-dimensional space. In multi-dimensional space, a product of delta functions is used.

Once (3.5) is solved for a point source of unit strength and the corresponding Green's function G is determined for the specific problem, u can be solved for any given source distribution f [1, p. 512].

$$Lu(\mathbf{x}) = f(\mathbf{x}). \quad (3.6)$$

This is accomplished by superposing the responses to point sources of unit strength, as in [1, p. 512]

$$u(\mathbf{x}) = \iiint_V G(\mathbf{x}, \mathbf{x}') f(\mathbf{x}') dv', \quad (3.7)$$

where integration is performed over the source point variables x', y', z' .

One application of the Green's function is solving Poisson's equation. The scalar potential ϕ can be calculated from a density of charge distribution ρ by using the Green's function of this specific problem. If there are no boundaries present, it takes the form [1, pp. 510-511, 8, p. 56]

²This section follows closely the treatment in: R. E. Collin, *Field Theory of Guided Waves*, IEEE Press, 2015 and G. B. Arfken and H. J. Weber, *Mathematical Methods for Physicists*, Academic Press, 2013

$$\nabla^2 \phi(\mathbf{x}) = -\frac{\rho(\mathbf{x})}{\epsilon}, \quad (3.8a)$$

$$\phi(\mathbf{x}) = \frac{1}{4\pi\epsilon} \iiint_V \frac{\rho(\mathbf{x}')}{|\mathbf{x} - \mathbf{x}'|} dv'. \quad (3.8b)$$

The Green's function for this problem is given by

$$G(\mathbf{x}, \mathbf{x}') = \frac{1}{4\pi|\mathbf{x} - \mathbf{x}'|}, \quad (3.9)$$

which represents the potential at position \mathbf{x} due to a unit point charge located at \mathbf{x}' . In this context, the input function is $u = \phi$ and the source function is $f = -\rho/\epsilon$ [1, pp. 510-511].

Solutions in different volumes of interest V_1, V_2, \dots, V_n can be matched across their shared surfaces S_1, S_2, \dots, S_n by imposing appropriate boundary conditions on the shared surfaces. This fact is useful when later investigating field propagation in the TEM cell, where a separation of regions significantly simplifies the analysis. Applying Green's second identity to Poisson's equation provides a means of enforcing such a boundary condition upon the surrounding surface S of a volume V [1, p. 511, 8, p. 57],

$$\iiint_V (\phi \nabla_{\mathbf{x}'}^2 G - G \nabla_{\mathbf{x}'}^2 \phi) dv' = \oint_S \left(\phi \frac{\partial G}{\partial n} - G \frac{\partial \phi}{\partial n} \right) d\mathbf{s}'. \quad (3.10)$$

Let \mathbf{n} denote the unit outward normal vector to the surface S , and let $\frac{\partial}{\partial n}$ denote the corresponding normal derivative $\nabla G \cdot \mathbf{n} = \frac{\partial G}{\partial n}$. The operator $\nabla_{\mathbf{x}'}^2$ differentiates with respect to the source vector \mathbf{x}' due to x', y', z' being the integrands. Inserting $\nabla^2 \phi = -\rho/\epsilon$ from (3.8a) and $\nabla^2 G = -\delta$ from (3.5) leads to [8, p. 58]

$$\phi = \frac{1}{\epsilon} \iiint_V \rho(\mathbf{x}') G(\mathbf{x}, \mathbf{x}') dv' + \oint_S \left(G \frac{\partial \phi}{\partial n} - \phi \frac{\partial G}{\partial n} \right) d\mathbf{s}'. \quad (3.11)$$

The scalar potential ϕ or its normal derivative to the surface, $\partial\phi/\partial n$, can be specified on the boundary. If only one of these quantities is known on the boundary surface, the Green's function can be adapted so that the unknown quantity vanishes. When ϕ is defined over the entire boundary, Dirichlet boundary conditions are satisfied. Conversely, when $\partial\phi/\partial n$ is defined over the entire boundary, Neumann boundary conditions apply [8, pp. 55-59].

3.2.2 Dyadic Green's Function

While the scalar Green's function is effective for solving one-dimensional differential equations, the dyadic Green's function $\bar{\mathbf{G}}$ is more appropriate for addressing three-dimensional problems. In general, the dyadic Green's function relates a vector source to a vector response. This is demonstrated when solving the vector Helmholtz equation, as shown in [8, p. 91]

$$\nabla^2 \mathbf{A} + k^2 \mathbf{A} = -\mu \mathbf{J}. \quad (3.12)$$

When $\mu \mathbf{J}$ is replaced by a unit vector source $(\hat{\mathbf{a}}_x + \hat{\mathbf{a}}_y + \hat{\mathbf{a}}_z) \delta(\mathbf{x} - \mathbf{x}')$, the solution for \mathbf{A} in (3.12) in free space is

$$(\hat{\mathbf{a}}_x + \hat{\mathbf{a}}_y + \hat{\mathbf{a}}_z) \frac{e^{-jk|\mathbf{x}-\mathbf{x}'|}}{4\pi|\mathbf{x}-\mathbf{x}'|}. \quad (3.13)$$

By definition, this constitutes a vector Green's function [8, pp. 91-92].

Each component of the current distribution \mathbf{J} generates fields through a linear relation. This relationship can effectively be represented by dyadics, which are linear mappings between vectors. The dyadic Green's function is therefore introduced and defined as

$$\begin{aligned} \bar{\mathbf{G}} = & G_{xx} \hat{\mathbf{a}}_x \hat{\mathbf{a}}_x + G_{xy} \hat{\mathbf{a}}_x \hat{\mathbf{a}}_y + G_{xz} \hat{\mathbf{a}}_x \hat{\mathbf{a}}_z + \\ & G_{yx} \hat{\mathbf{a}}_y \hat{\mathbf{a}}_x + G_{yy} \hat{\mathbf{a}}_y \hat{\mathbf{a}}_y + G_{yz} \hat{\mathbf{a}}_y \hat{\mathbf{a}}_z + \\ & G_{zx} \hat{\mathbf{a}}_z \hat{\mathbf{a}}_x + G_{zy} \hat{\mathbf{a}}_z \hat{\mathbf{a}}_y + G_{zz} \hat{\mathbf{a}}_z \hat{\mathbf{a}}_z. \end{aligned}$$

Each component of the current vector \mathbf{J} is associated with one unit vector of the Green's function, i.e. J_x with $\hat{\mathbf{a}}_x$, J_y with $\hat{\mathbf{a}}_y$ and J_z with $\hat{\mathbf{a}}_z$ [8, p. 92]. Consequently, the field generated by a current component in a given direction is determined by the corresponding column of the dyadic Green's function. For example, if only a current component J_x is present, the field components A_x , A_y , and A_z are obtained from the Green's function's elements G_{xx} , G_{yx} and G_{zx} .

The dyadic Green's function is defined as the solution of

$$\nabla^2 \bar{\mathbf{G}}(\mathbf{x}, \mathbf{x}') + k^2 \bar{\mathbf{G}} = -\bar{\mathbf{I}} \delta(\mathbf{x} - \mathbf{x}'). \quad (3.14)$$

In free space, a commonly used form of the dyadic Green's function is given by [8, p. 92]

$$\bar{\mathbf{G}}(\mathbf{x}, \mathbf{x}') = \bar{\mathbf{I}} \frac{e^{-jk|\mathbf{x}-\mathbf{x}'|}}{4\pi|\mathbf{x}-\mathbf{x}'|}, \quad (3.15)$$

where $\bar{\mathbf{I}}$ is a unit dyadic. The free-space case is presented here to provide an overview. Dyadic Green's functions can also be derived for bounded geometries, such as waveguides, by implementing appropriate boundary conditions.

The fields \mathbf{A} generated by arbitrary \mathbf{J} can be expressed with the dyadic Green's function as

$$\mathbf{A}(\mathbf{x}) = \mu \iiint_V \bar{\mathbf{G}}(\mathbf{x}, \mathbf{x}') \mathbf{J}(\mathbf{x}') d\mathbf{x}'. \quad (3.16)$$

Each component of \mathbf{J} drives a combination of components in \mathbf{A} . Dyadics capture this component-wise coupling and simplify the notation [8, p. 92].

3.3 Modes in Waveguides

3.3.1 Rectangular Waveguides as non-TEM structures

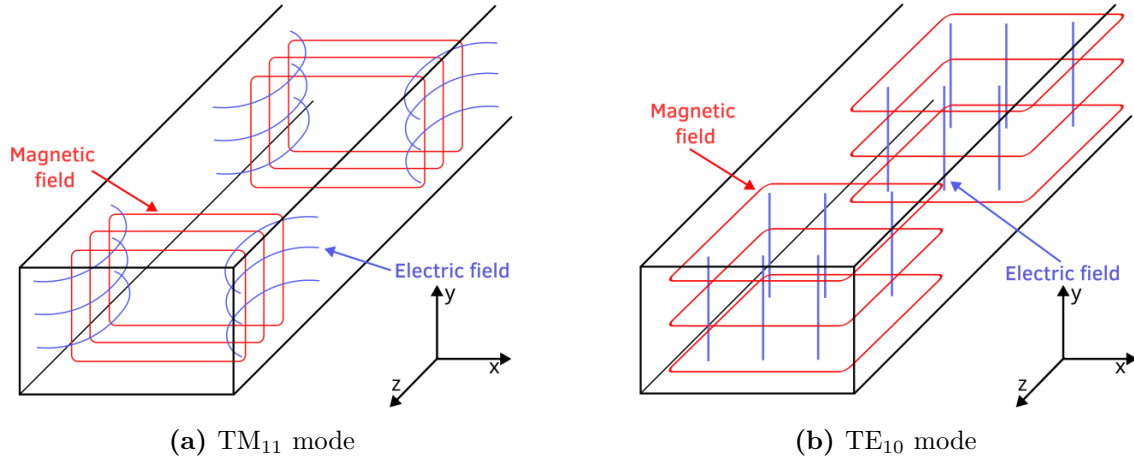


Figure 3.1 The electric and magnetic fields corresponding to the first dominant TE and TM modes in a rectangular waveguide with perfectly conducting walls.

Waveguides with perfectly conducting walls support only TE and TM modes. The field distributions for the two primary dominant modes are depicted in Figure 3.1.

The physical impossibility of TEM propagation within these structures is a direct consequence of Maxwell's equations. Following the analytical framework established in [11, pp. 425-427], we demonstrate this by first decomposing the electric field intensity \mathbf{E} and magnetic field intensity \mathbf{H} into their longitudinal and transverse components, assuming wave propagation in the z -direction:

$$\mathbf{E} = (E_x \cdot \hat{\mathbf{a}}_x + E_y \cdot \hat{\mathbf{a}}_y + E_z \cdot \hat{\mathbf{a}}_z) e^{-jkz}, \quad (3.17a)$$

$$\mathbf{H} = (H_x \cdot \hat{\mathbf{a}}_x + H_y \cdot \hat{\mathbf{a}}_y + H_z \cdot \hat{\mathbf{a}}_z) e^{-jkz}. \quad (3.17b)$$

Next, applying Faraday's and Ampère-Maxwell law to (3.17a) and (3.17b) yields [11, p. 426]

$$\nabla \times \mathbf{E} = \begin{pmatrix} \frac{\partial}{\partial y} E_z - jk E_y \\ jk E_x - \frac{\partial}{\partial x} E_z \\ \frac{\partial}{\partial x} E_y - \frac{\partial}{\partial y} E_x \end{pmatrix} = \begin{pmatrix} -j\omega B_x \\ -j\omega B_y \\ -j\omega B_z \end{pmatrix}, \quad (3.18a)$$

$$\nabla \times \mathbf{B} = \begin{pmatrix} \frac{\partial}{\partial y} B_z - jk B_y \\ jk B_x - \frac{\partial}{\partial x} B_z \\ \frac{\partial}{\partial x} B_y - \frac{\partial}{\partial y} B_x \end{pmatrix} = \begin{pmatrix} \frac{j\omega}{\mu\epsilon} E_x \\ \frac{j\omega}{\mu\epsilon} E_y \\ \frac{j\omega}{\mu\epsilon} E_z \end{pmatrix}. \quad (3.18b)$$

For a TEM mode, the longitudinal field components vanish $E_z = H_z = 0$. Consequently, (3.18a) and (3.18b) reduce to the following conditions for the transverse electric field components:

$$\frac{\partial}{\partial x} E_x + \frac{\partial}{\partial y} E_y = 0 \quad \text{Derived from Gauss' law,} \quad (3.19)$$

$$\frac{\partial}{\partial y} E_x - \frac{\partial}{\partial x} E_y = 0 \quad \text{Derived from Faraday's law.} \quad (3.20)$$

Since the solutions in (3.19) and (3.20) cannot satisfy the rectangular waveguide's boundary conditions, a TEM mode cannot propagate.

3.4 TEM mode in the TEM cell³

In contrast to the rectangular waveguide, a TEM cell supports the propagation of TEM waves. Moreover, the TEM mode is inherently excited by the geometry of the TEM cell, and is therefore referred to as the essential mode. Higher-order TE and TM modes, which arise only due to non-uniformities in the TEM cell, are termed non-essential modes [17].

The TEM mode in the TEM cell is derived using a procedure presented in [34, 36]. This approach involves determining the Green's function for the longitudinal field components, H_z and E_z , of both the TE and TM modes in a rectangular waveguide. The Green's function satisfies the wave equations and boundary conditions of the waveguide, and is constructed as described in Section 3.2.1, with

$$(\nabla^2 + k_t^2)G_j(\mathbf{x}_t, \mathbf{x}'_t) = -\delta(\mathbf{x}_t - \mathbf{x}'_t), \quad (3.21a)$$

$$\frac{\partial G_j(\mathbf{x}_t, \mathbf{x}'_t)}{\partial n} = 0. \quad (3.21b)$$

The wave number is separated into transverse and longitudinal components, $k^2 = k_t^2 + k_z^2$. Equation (3.21b) specifies the boundary conditions on the perfectly conducting walls and septum of the TEM cell, as well as on the gaps, as illustrated in Figure 3.2. The index j indicates the chamber to which the Green's function applies ($j = 1$ for the upper chamber, $j = 2$ for the lower chamber). The source points are denoted by $\mathbf{x}'_t = (\hat{\mathbf{a}}_x x' + \hat{\mathbf{a}}_y y')$, and the observation points by $\mathbf{x}_t = (\hat{\mathbf{a}}_x x + \hat{\mathbf{a}}_y y)$. These coordinates are transformed to depend on the wave number k instead of the z -coordinate, which significantly simplifies the derivation of the Green's function, as only a two-dimensional surface must be considered.

The waveguide is excited by an infinitesimal electric dipole moment, centrally located and oriented along the y -axis. Solving for H_z and applying Green's second identity yields [36, p. 5]

³This section follows closely the treatment in: P. F. Wilson et al., *Excitation of a TEM cell by a Vertical Electric Hertzian Dipole*, National Bureau of Standards, 1981

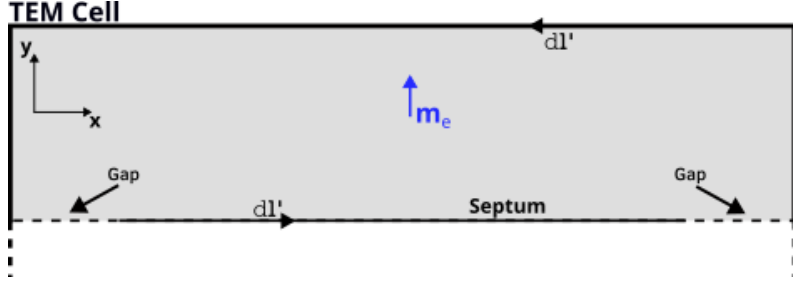


Figure 3.2 In this analysis, the Green's function determines the fields within the cross-sectional surface S of the TEM cell, which is shown in light gray and bounded by l . The source exciting these fields is a centrally located electric dipole moment, \mathbf{m}_e .

$$\int_l \left(G_j(\mathbf{x}_t, \mathbf{x}'_t) \frac{\partial H_z(\mathbf{x}_t)}{\partial n} - H_z(\mathbf{x}'_t) \frac{\partial G_j(\mathbf{x}_t, \mathbf{x}'_t)}{\partial n} \right) d\mathbf{l}' = \quad (3.22)$$

$$= H_z(\mathbf{x}_t) - \int_S G_j(\mathbf{x}_t, \mathbf{x}'_t) \frac{\partial J_y(\mathbf{x}'_t)}{\partial x'} d\mathbf{s}', \quad (3.23)$$

Here, S denotes the waveguide cross-section and l its boundary. Applying the boundary condition (3.21b) to the perfectly conducting septum and walls reduces the boundary integrals to those over the gaps. The electric dipole is then substituted into (3.23), and continuity of H_z and $\partial H_z / \partial y$ across these gaps is enforced. The normal vector in the gap region is oriented along the y -direction, $n = \pm \mathbf{y}$. Accordingly, the line element in the integrand becomes $d\mathbf{l}' = dx'$. The right-hand side of (3.23) is integrated by parts. Finally, assuming that the electric dipole moment is located in the upper chamber, only G_1 needs to be considered. For the boundary, a combined Green's function accounts for field continuity between the chambers $G(x, x') = G_1(x, 0, x', 0) + G_2(x, 0, x', 0)$. Altogether, this yields [36, pp. 5-6]

$$\int_{\text{gaps}} G(x, x') \frac{\partial H_z(x', 0)}{\partial y'} dx' = -\mathbf{m}_e \frac{\partial G_1(x, 0, \mathbf{x}'_t)}{\partial x'}. \quad (3.24)$$

Solving for the Green's function G provides a solution for the longitudinal magnetic field intensity H_z of the TE mode. An analogous procedure can be used to determine the longitudinal electric field intensity E_z of the TM mode. As shown in [36], the total field distribution is then given by the superposition of the TE and TM mode fields, thereby demonstrating the excitation of the TEM mode. The transverse fields \mathbf{E}_t and \mathbf{H}_t can then be derived from the longitudinal field components H_z and E_z . They are related to H_z by [36, p. 3]

$$\mathbf{E}_t(\mathbf{x}_t) = \frac{j\omega\mu_0}{k_t^2} \nabla_t H_z(\mathbf{x}_t) \times \hat{\mathbf{a}}_z, \quad (3.25a)$$

$$\mathbf{H}_t(\mathbf{x}_t) = -\frac{jk_z}{k_t^2} \nabla_t H_z(\mathbf{x}_t), \quad (3.25b)$$

and to E_z by

$$\mathbf{E}_t(\mathbf{x}_t) = -\frac{jk_z}{k_t^2} \nabla_t E_z(\mathbf{x}_t), \quad (3.26a)$$

$$\mathbf{H}_t(\mathbf{x}_t) = \frac{-j\omega\epsilon_0}{k_t^2} \nabla_t E_z(\mathbf{x}_t) \times \hat{\mathbf{a}}_z, \quad (3.26b)$$

where $\nabla_t = \hat{\mathbf{a}}_x \partial/\partial x + \hat{\mathbf{a}}_y \partial/\partial y$ denotes the transverse gradient operator.

3.4.1 Higher-order modes

To determine the usable frequency range of the TEM cell shown in Figure 3.4, the cutoff frequencies of its higher-order modes are examined. Among these, the TE₁₀ and TE₀₁ modes are of primary interest as they exhibit the lowest cutoff frequencies. Their transverse electric field distributions are illustrated in Figure 3.3, while Figure 3.6 shows the electric and magnetic field distributions along the TEM cell for each mode. As shown there, the TEM mode exhibits the highest phase velocity, reflected in the large number of periods along the cell, and its magnetic field has no longitudinal component. In contrast, the TE₀₁ and TE₁₀ modes possess longitudinal magnetic field components. For the TE₀₁ mode, these are concentrated near the side walls and are therefore not directly shown in Figure 3.6. For a thin septum ($t/b \ll 0.1$), the cutoff frequencies of modes with even n

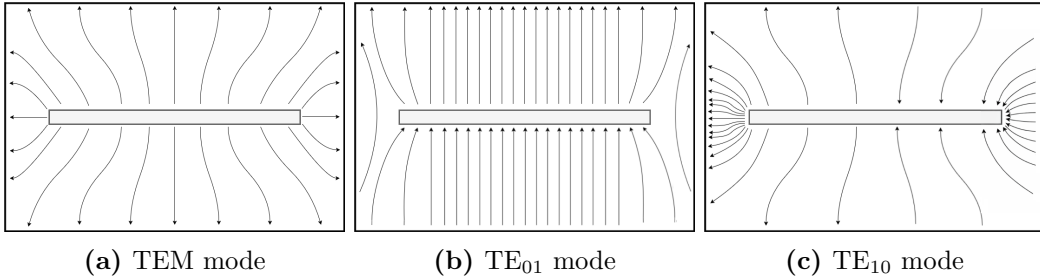


Figure 3.3 Transverse electric field distributions in the cross section of the TEM cell.

subscripts, i.e. TE_{m,2n} and TM_{m,2n} modes, can be approximated by the cutoff frequency expression for rectangular waveguides [35]

$$f_c = \frac{c}{2} \sqrt{\left(\frac{m}{a}\right)^2 + \left(\frac{n}{b}\right)^2}, \quad (3.27)$$

where c is the speed of light, and $m \geq 0$ and $n \geq 0$ are the integer mode indices along the a - and b -directions, respectively. Applying (3.27) to a TEM cell with $a = 40$ mm, $b = 24$ mm, $g = 5$ mm, and $t = 0.1$ mm yields the cutoff frequency of the TE₁₀ mode of $f_{c,10} = 3.75$ GHz. For modes with odd n subscripts, such as the TE₀₁ mode, analytical approximations are given in [39]. Although omitted here due to their complexity, these expressions yield $f_{c,01} = 3.12$ GHz for the TE₀₁ mode.

To validate the analytically derived cutoff frequencies, the forward transmission coefficients S_{12} between the output ports of the TEM cell are computed numerically over frequency and shown in Figure 3.5. The cutoff frequency f_c is identified as the lowest frequency at which undisturbed mode propagation occurs, corresponding to $S_{12} = 0$ dB. The numerically

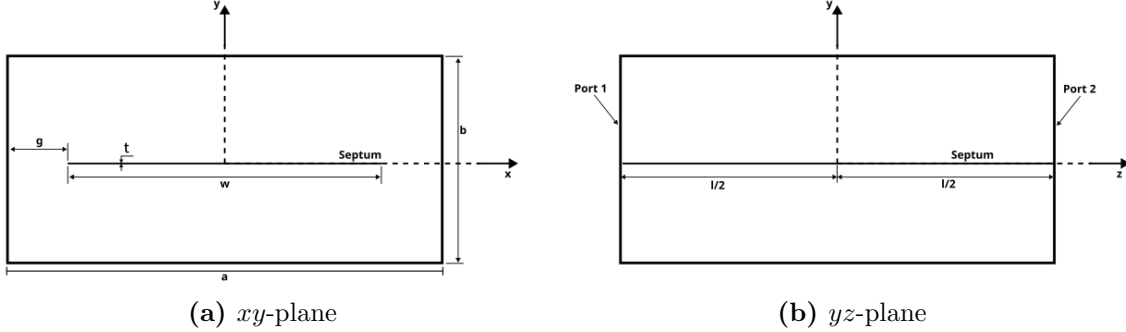


Figure 3.4 Geometrical arrangement of the TEM cell, demonstrated with cross sections in the xy -plane and the yz -plane.

determined cutoff frequencies of the TE_{10} and TE_{01} modes, $f_{c,10} = 3.75$ GHz and $f_{c,01} = 3.12$ GHz, agree well with the analytical values obtained from (3.27) and [39], respectively.

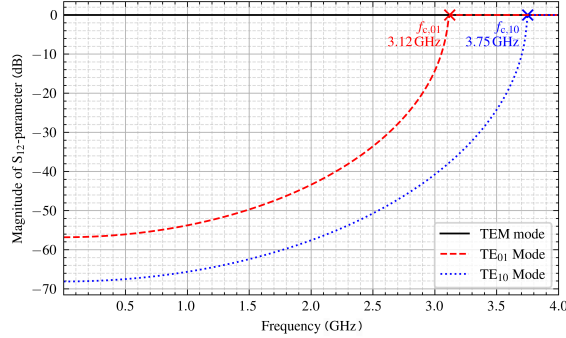


Figure 3.5 Forward transmission coefficients S_{12} of the TEM, TE_{01} , and TE_{10} modes in the TEM cell over frequency.

Once these higher-order modes are excited, their behavior is governed by the tapered sections at the output ports of the TEM cell. While the TEM mode propagates through these transitions with negligible reflection, higher-order TE and TM modes are reflected at the tapers. Consequently, the TEM cell acts as a high- Q cavity resonator for these modes, with resonances occurring at electrical lengths of $\frac{\lambda}{2}$ and its integer multiples [35]. Numerical investigations of TEM cell models including tapered sections are presented in [17], while analytical approximations of the resulting resonance frequencies are given in [35]. As the further investigations in this thesis focus on mode propagation independent of the tapered sections, the latter are omitted from the simulation models and Figure 3.4.

In a physical TEM cell, wave propagation in the TEM mode may excite higher-order TE and TM modes due to material discontinuities or finite conductivity of the conducting plates [18]. Such discontinuities force the electric and magnetic fields to develop a component in the direction of propagation, thereby exciting TE and TM modes and introducing measurement uncertainties. These uncertainties are absent in numerical analysis, which

is one of the key reasons why simulation is preferred over measurements with a physical TEM cell in this thesis.

Table 3.1 lists the cutoff frequencies of the TE₀₁ and TE₁₀ modes determined numerically and analytically for different TEM cell dimensions. The remainder of this thesis focuses on a TEM cell with $a = 40$ mm and $b = 24$ mm, for which the cutoff frequencies are $f_{c,01} = 3.12$ GHz and $f_{c,10} = 3.75$ GHz, respectively.

a (mm)	b (mm)	TE ₀₁ f_c (GHz)	TE ₁₀ f_c (GHz)
80	24	1.89	2.05
40	24	3.12	3.75
40	48	2.10	3.75

Table 3.1 Cutoff frequencies of the TE₀₁ and TE₁₀ modes for different TEM cell dimensions, derived both through numerical simulation and analytical calculation. The results of these separate methods agree within the precision shown. As expected from (3.27), the TE₁₀ cutoff frequency depends only on a and is independent of b , consistent with rectangular waveguide theory. The TE₀₁ cutoff frequency varies with both a and b .

3.4.2 Field distributions

The normalized electric field intensity of the TEM mode is given as $\mathbf{e}_{\text{TEM}}^{\pm} = e_{\text{TEM},x}^{\pm} \hat{\mathbf{a}}_x + e_{\text{TEM},y}^{\pm} \hat{\mathbf{a}}_y + e_{\text{TEM},z}^{\pm} \hat{\mathbf{a}}_z$ and normalized to \sqrt{W} . The x - and y -component of $\mathbf{e}_{\text{TEM}}^{\pm}$ are analytically approximated by

$$e_{\text{TEM},x}^{\pm} = \frac{4}{a} Z_w^{1/2} \sum_{m_o=1}^{\infty} \frac{\sinh M(b/2 - py)}{\sinh Mb/2} \cdot \sin Mx \sin Ma/2 J_0(Mg), \quad (3.28a)$$

$$e_{\text{TEM},y}^{\pm} = p \frac{4}{a} Z_w^{1/2} \sum_{m_o=1}^{\infty} \frac{\cosh M(b/2 - py)}{\sinh Mb/2} \cdot \cos Mx \sin Ma/2 J_0(Mg). \quad (3.28b)$$

Z_w denotes the characteristic impedance of the TEM cell output port, a its width and b its height. The sign-function is defined as $p = 1$ above the septum and $p = -1$ below it. The parameter $M = m_o \pi / 2a$, and g denotes the gap width between the septum and the conducting wall. The index $m_o = 1, 3, 5, \dots$ iterates over odd integers. Both expressions are derived in [36] using the procedure described in Section 3.4. Analytical expressions for higher-order modes are provided in [34] and not investigated further in this thesis.

In case of higher-order modes propagating, the analysis of the field distribution is conducted with the following assumptions. Each of the propagating modes is assumed to be orthogonal to each other,

$$\iint \mathbf{e}_n^{\pm} \times \mathbf{h}_m^{\pm} d\mathbf{s}' = 0 \quad \text{if } n \neq m, \quad (3.29)$$

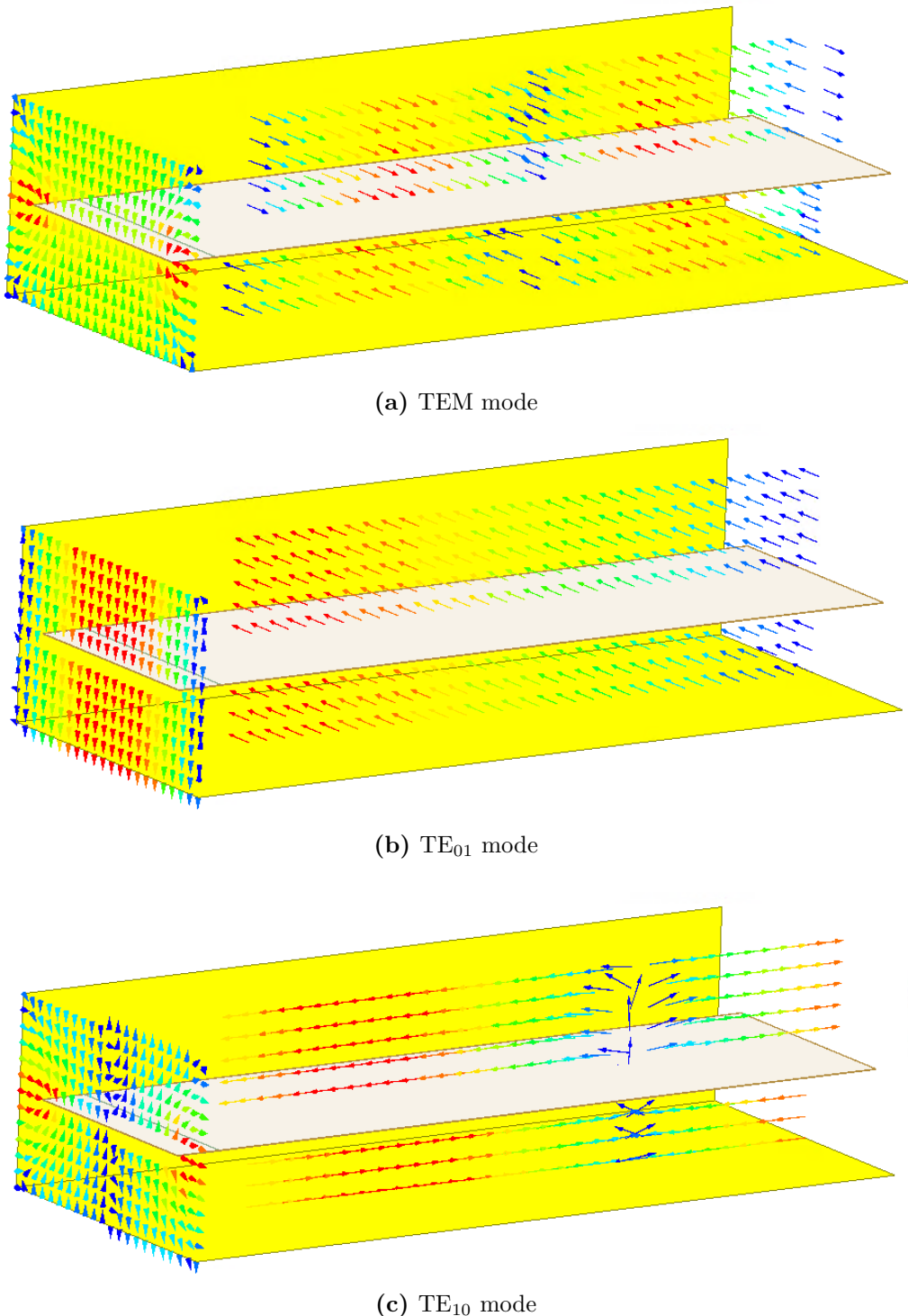


Figure 3.6 Electric and magnetic field distributions of the TEM, TE₀₁, and TE₁₀ modes in the TEM cell. The magnetic fields are shown along the full length of the cell, while the electric fields are shown at the ports only.

with \mathbf{e}_n^\pm and \mathbf{h}_n^\pm being the function vectors of the normalized electric and magnetic field intensities of the n -th mode in transverse direction [8, p. 359]. This indicates that the modes do not couple with each other, which is the case in a uniform waveguide with perfectly conducting walls, as discussed in Section 3.4.1. Furthermore, each mode is normalized to \sqrt{W} as shown by

$$\iint \mathbf{e}_n^\pm \times \mathbf{h}_n^\pm ds' = 1. \quad (3.30)$$

Throughout, the superscripts ‘+’ and ‘−’ denote propagation along the positive and negative z -direction, respectively. The radiated fields along the positive z -direction can be described by a summation of normal modes, as in [8, p. 360]

$$\mathbf{E}^+ = \sum_n a_n \mathbf{e}_n^+, \quad (3.31a)$$

$$\mathbf{H}^+ = \sum_n a_n \mathbf{h}_n^+. \quad (3.31b)$$

The fields propagating along the negative z -direction are expressed by [8, p. 360]

$$\mathbf{E}^- = \sum_n b_n \mathbf{e}_n^-, \quad (3.32a)$$

$$\mathbf{H}^- = \sum_n b_n \mathbf{h}_n^-, \quad (3.32b)$$

where \mathbf{h}_n^\pm is the normalized magnetic field intensity. The model expansion coefficients for the forward and backward propagating waves, a_n and b_n , have units of \sqrt{W} and weight \mathbf{e}_n^\pm and \mathbf{h}_n^\pm of the corresponding mode. The field intensities at the outputs \mathbf{E}^\pm and \mathbf{H}^\pm are therefore decomposed into several propagating mode fields, each weighted with the corresponding coefficients. The derivation of a_n and b_n is discussed in Section 3.5.

The normalized magnetic field intensity \mathbf{h}_n^\pm is derived in an analogous manner to \mathbf{e}_n^\pm . For the TEM mode, $\mathbf{h}_{\text{TEM}}^\pm$ can also be directly obtained from $\mathbf{e}_{\text{TEM}}^\pm$ with

$$\mathbf{h}_{\text{TEM}}^\pm = \pm \frac{1}{\eta_0} \hat{\mathbf{a}}_z \times \mathbf{e}_{\text{TEM}}^\pm, \quad (3.33)$$

where $\eta_0 \approx 377 \Omega$ is the free-space wave impedance.

The normalized electric field intensity $\mathbf{e}_{\text{TEM}}^\pm$ of the TEM mode is a key parameter for determining the coupling between a source and the output ports of the TEM cell, as derived using the Lorentz reciprocity theorem discussed in Section 3.1. For example, Figure 3.7a shows the output power generated by an electric dipole moment \mathbf{m}_e oriented along the y -direction. The dipole is displaced along the x -axis at the center height between

the septum and the upper wall of the TEM cell, which has a width of $a = 40$ mm and a height of $b = 24$ mm.

The normalized electric field component in the y -direction $e_{\text{TEM},y}^{\pm}$ reaches its maximum magnitude at the center of the TEM cell, according to (3.28b). The integral form of the Lorentz reciprocity theorem in (3.2) states that this results in the largest output power. This behavior is confirmed by the results shown in Figure 3.7a. Analogously, the output power shown in Figure 3.7b is largest close to the TEM cell wall if the dipole moment is oriented in the x -direction. Analysis of the field distribution is therefore useful to explain coupling behavior of electrically small antennas or dipole moments displaced within the TEM cell.

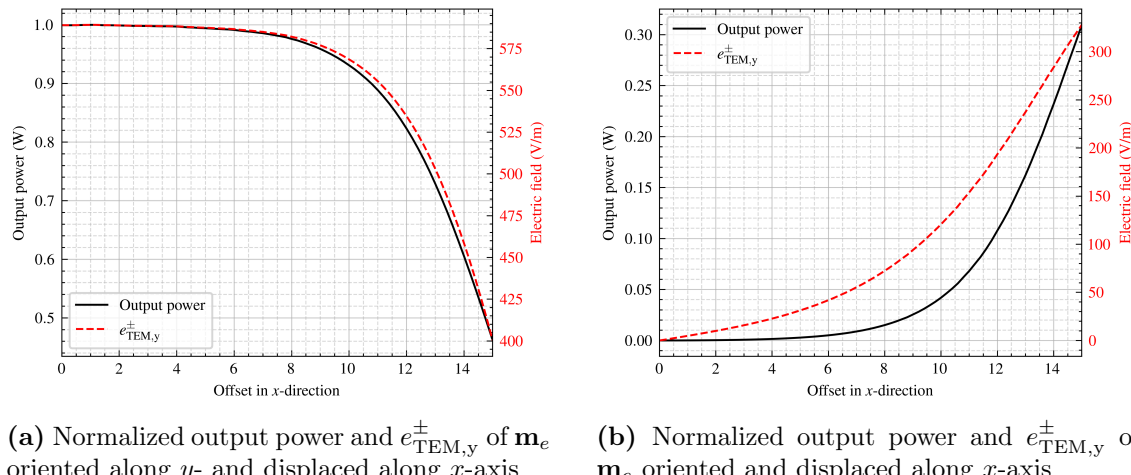


Figure 3.7 Output power and e_{TEM}^{\pm} for different electric dipole moment positions and orientations.

For this reason, Figure 3.8 shows the normalized electric field intensity in the TEM cell for both the x - and y -direction.

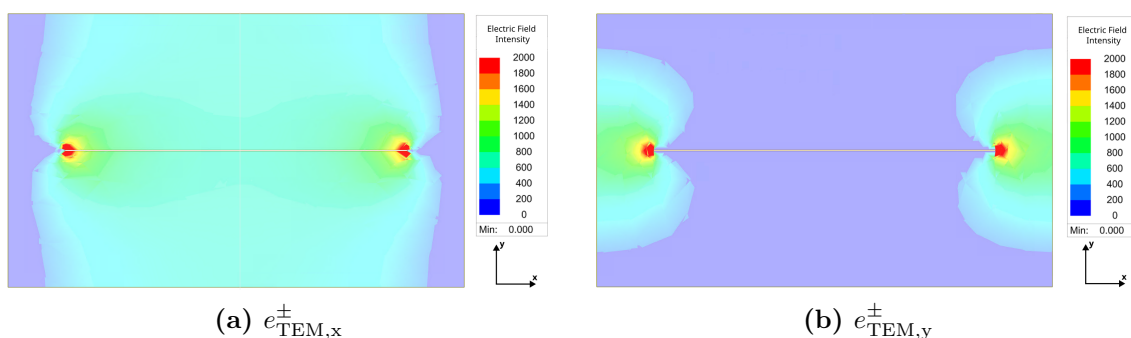


Figure 3.8 The normalized electric field distribution e_{TEM}^{\pm} in the TEM cell excited with an input power of $1/2$ W at a frequency of 3 GHz.

The normalized electric field of the TEM mode at $x = 0$ is constant along the y -axis, as confirmed by both the analytical result of (3.28b) and numerical simulation. For a TEM

cell width $a = 40$ mm and height $b = 24$ mm, this field equals $\mathbf{e}_{\text{TEM}}^{\pm} = 589.25 \text{ V/m } \hat{\mathbf{a}}_y$.

3.5 Radiating Sources in TEM Cells

3.5.1 Arbitrary source

Suppose a current \mathbf{J}_1 excites the TEM cell, as shown in Figure 3.9. Normally, such a current would require external fields to drive it, however, these are neglected here. Only the fields \mathbf{E} and \mathbf{H} radiated by \mathbf{J}_1 are considered. These fields satisfy Maxwell's equations [8, p. 360]:

$$\nabla \times \mathbf{E} = -j\omega\mu_0 \mathbf{H}, \quad (3.34a)$$

$$\nabla \times \mathbf{H} = j\omega\epsilon_0 \mathbf{E} + \mathbf{J}_1. \quad (3.34b)$$

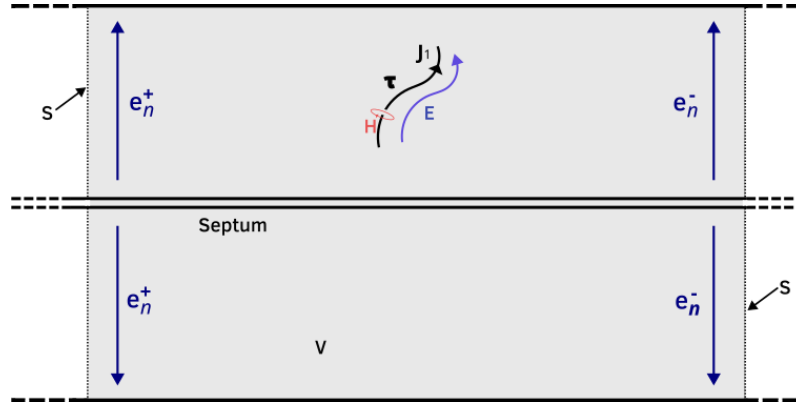


Figure 3.9 TEM cell with an arbitrary current source \mathbf{J}_1 along the line τ . \mathbf{E} and \mathbf{H} are the field intensities induced by the current. \mathbf{e}_n^+ and \mathbf{e}_n^- are outgoing fields towards both output ports of the TEM cell. \mathbf{S} indicates the surface, and V the volume of the domain in question.

Applying the integral form of the Lorentz reciprocity theorem in (3.2) with $\mathbf{J}_2 = \mathbf{M}_1 = \mathbf{M}_2 = 0$ yields

$$\iint_S (\mathbf{e}_n^{\pm} \times \mathbf{H} - \mathbf{E} \times \mathbf{h}_n^{\pm}) d\mathbf{s}' = \iiint V \mathbf{J}_1 \cdot \mathbf{e}_n^{\pm} dv'. \quad (3.35)$$

Using the modal expansions (3.31a) to (3.32b) for the fields \mathbf{E} and \mathbf{H} radiated by \mathbf{J}_1 leads to

$$\begin{aligned}
& \iint_S (\mathbf{e}_n^+ \times \mathbf{H} - \mathbf{E} \times \mathbf{h}_n^+) d\mathbf{s}' = \\
&= \iint_S (\mathbf{e}_n^+ \times \sum_m a_m \mathbf{h}_m^+ - \sum_m a_m \mathbf{e}_m^+ \times \mathbf{h}_n^+) d\mathbf{s}' \\
&= \sum_m a_m \iint_S (\mathbf{e}_n^+ \times \mathbf{h}_m^+ - \mathbf{e}_m^+ \times \mathbf{h}_n^+) d\mathbf{s}'.
\end{aligned} \tag{3.36}$$

Due to the orthogonality condition in (3.29) and the normalization in (3.30), the coefficients of each mode can be evaluated separately with

$$\begin{aligned}
& \iint_S (\mathbf{e}_n^+ \times \mathbf{H} - \mathbf{E} \times \mathbf{h}_n^+) d\mathbf{s}' = \\
&= a_n \iint_S (\mathbf{e}_n^+ \times \mathbf{h}_n^+ - \mathbf{e}_n^+ \times \mathbf{h}_n^+) d\mathbf{s}' = -2a_n.
\end{aligned} \tag{3.37}$$

The coefficient b_n of the fields \mathbf{e}_n^- and \mathbf{h}_n^- is evaluated in the same manner:

$$b_n = -\frac{1}{2} \iiint \mathbf{J}_1 \cdot \mathbf{e}_n^- dv' \tag{3.38}$$

Assuming only the TEM mode can propagate, combining (3.30) with the fields \mathbf{e}_{TEM} and \mathbf{h}_{TEM} with their respective coefficients a_{TEM} , b_{TEM} leads to [38]

$$P_{\text{out1}} = \iint_S \langle \mathbf{S} \rangle d\mathbf{s}' = \iint_S \frac{1}{2} \Re \{ (a \cdot \mathbf{e}_{\text{TEM}}^\pm) \times (a \cdot \mathbf{h}_{\text{TEM}}^\pm)^* \} d\mathbf{s}' = \frac{|a_{\text{TEM}}|^2}{2}, \tag{3.39a}$$

$$P_{\text{out2}} = \iint_S \langle \mathbf{S} \rangle d\mathbf{s}' = \iint_S \frac{1}{2} \Re \{ (b \cdot \mathbf{e}_{\text{TEM}}^\pm) \times (b \cdot \mathbf{h}_{\text{TEM}}^\pm)^* \} d\mathbf{s}' = \frac{|b_{\text{TEM}}|^2}{2}. \tag{3.39b}$$

The Poynting vector $\langle \mathbf{S} \rangle$ of the TEM mode in Equations (3.39a) to (3.39b) does not have an imaginary component,

$$\langle \mathbf{S} \rangle = \mathbf{e}_{\text{TEM}}^\pm \times \mathbf{h}_{\text{TEM}}^\pm = \Re \{ \mathbf{e}_{\text{TEM}}^\pm \times (\mathbf{h}_{\text{TEM}}^\pm)^* \}. \tag{3.40}$$

Equations (3.39a) to (3.39b) demonstrate that the coefficients a_{TEM} and b_{TEM} are directly related to the output power. Consequently, the output power can be directly linked to the electric and magnetic field distribution of the TEM mode, and vice versa.

3.5.2 Equivalent dipole moments

Equations (2.2) and (3.35) relate the electric dipole moment \mathbf{m}_e with a given source current \mathbf{J}_1 flowing through an infinitesimal wire, yielding [32]

$$\begin{pmatrix} a_n \\ b_n \end{pmatrix} = -\frac{1}{2} \mathbf{m}_e \cdot \mathbf{e}_n^\pm. \quad (3.41)$$

If this arbitrary current distribution forms an infinitesimal loop, the source can be represented by a magnetic dipole moment \mathbf{m}_m . This leads to [8]

$$\begin{aligned} \begin{pmatrix} a_n \\ b_n \end{pmatrix} &= - \oint_C \mathbf{e}_n^\pm d\mathbf{l} \\ &= - \iint_S \nabla \times \mathbf{e}_n^\pm ds' \\ &= j\omega\mu_0 \iint_S \mathbf{h}_n^\pm ds' \\ &= j\omega\mu_0 \mathbf{m}_m \cdot \mathbf{h}_n^\pm \end{aligned} \quad (3.42)$$

This formulation assumes that the magnetic field strength \mathbf{h}^\pm does not change over the loop area. This is the case for electrically small loops. Otherwise, the magnetic field strength \mathbf{h}^\pm must be considered in the integration process of (3.42) [8].

If several modes are propagating, it is useful to determine the coefficients a_n and b_n weighting the modes in (3.31a) and (3.32b). In this case, the orthogonality property in (3.29) can be used to derive [8]

$$2a_n = - \int_C \boldsymbol{\tau} \cdot \mathbf{e}_n^- dl, \quad (3.43a)$$

$$2b_n = \int_C \boldsymbol{\tau} \cdot \mathbf{e}_n^+ dl. \quad (3.43b)$$

The wire follows the curve C , and $\boldsymbol{\tau}$ is the tangential vector along that curve.

In the presence of both a magnetic and an electric dipole moment, their contributions can be summed, resulting in [32]

$$\begin{pmatrix} a_n \\ b_n \end{pmatrix} = \frac{1}{2} (-\mathbf{m}_e \cdot \mathbf{e}_n^\pm + j\omega\mu_0 \mathbf{m}_m \cdot \mathbf{h}_n^\pm). \quad (3.44)$$

For the TEM mode, the relation between $\mathbf{e}_{\text{TEM}}^\pm$ and $\mathbf{h}_{\text{TEM}}^\pm$ expressed in (3.33) yields a simplified form of (3.44), written as [32]

$$\begin{pmatrix} a_{\text{TEM}} \\ b_{\text{TEM}} \end{pmatrix} = -\frac{1}{2} (\mathbf{m}_e \pm jk\mathbf{m}_m \times \mathbf{z}) \cdot \mathbf{e}_{\text{TEM}}^\pm. \quad (3.45)$$

Equation (3.45) proves useful in later investigations, as it requires knowledge of only $\mathbf{e}_{\text{TEM}}^{\pm}$ to determine the dipole moments. The complex magnitude of the dipole moments m_e and m_m is separately derived by

$$m_e = \frac{a_{\text{TEM}} + b_{\text{TEM}}}{e_{\text{TEM}}^{\pm}}, \quad (3.46a)$$

$$m_m = j \frac{a_{\text{TEM}} - b_{\text{TEM}}}{k_0 e_{\text{TEM}}^{\pm}}. \quad (3.46b)$$

The individual components of the electric field for a given mode $\mathbf{e}_n^{\pm} = e_{n,x}^{\pm} \cdot \hat{\mathbf{a}}_x + e_{n,y}^{\pm} \cdot \hat{\mathbf{a}}_y + e_{n,z}^{\pm} \cdot \hat{\mathbf{a}}_z$ can be analyzed separately by examining the output power of the TEM cell. For example, the components of \mathbf{m}_e are derived with

$$m_{ex} = \frac{2\sqrt{P_x}}{e_{n,x}^{\pm}}, \quad (3.47a)$$

$$m_{ey} = \frac{2\sqrt{P_y}}{e_{n,y}^{\pm}}. \quad (3.47b)$$

P_x and P_y describe the power measured at one output port induced by the respective component of the dipole moment [32].

For the TEM mode, an electric dipole placed in the TEM cell leads to output power with the same phase at both ports. This directly results from the symmetric field distribution of the TEM mode leading to the same $\mathbf{e}_{\text{TEM}}^{\pm}$ component at the output ports. In contrast, a magnetic dipole results in a phase shift of $\pm\pi$. This difference arises from the phase shift of the magnetic fields at the output ports, $\mathbf{h}_{\text{TEM}}^+$ and $\mathbf{h}_{\text{TEM}}^-$, as illustrated in Figure 3.10.

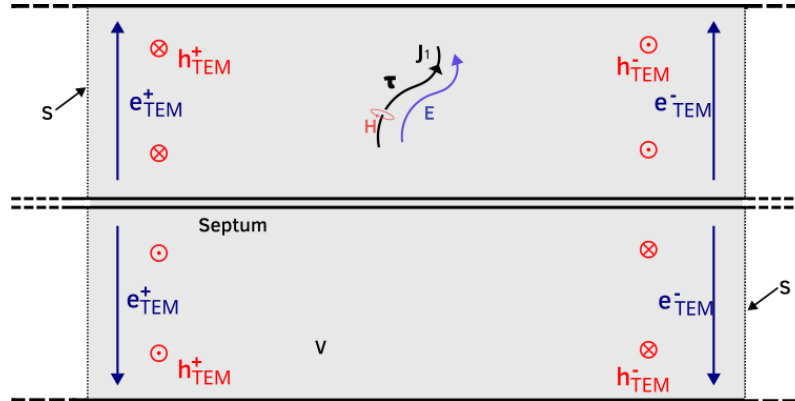


Figure 3.10 Field distribution of the TEM mode highlighting the out-of-phase magnetic fields at the output ports.

For the next higher-order mode TE_{01} , the situation is reversed. An electric dipole moment leads to a phase shift of $\pm\pi$, while a magnetic dipole moment produces no phase shift. This behavior is again due to the phase shift occurring now between the electric field

intensities at the output ports, $\mathbf{e}_{\text{TE01}}^+$ and $\mathbf{e}_{\text{TE01}}^-$, while there is no phase shift between the magnetic field intensities, $\mathbf{h}_{\text{TE01}}^+$ and $\mathbf{h}_{\text{TE01}}^-$.

It is assumed that the dipole moments are positioned halfway along the septum in z -direction. A shift in z -direction introduces a phase shift between the output port powers, consequently altering the results derived above.

3.5.3 Electrically small antennas

The electric field coupling with an electrically small antenna can be expressed as [8, p. 361]

$$2a_n = - \int_C \boldsymbol{\tau} I(l) \cdot \mathbf{e}_n^+ dl. \quad (3.48a)$$

$$2b_n = - \int_C \boldsymbol{\tau} I(l) \cdot \mathbf{e}_n^- dl. \quad (3.48b)$$

Since the antenna is electrically small, the electric field \mathbf{e}_n^\pm is assumed to be constant in C . Furthermore, if the current I is constant along C , it does not have to be considered in the integration. Integrating over the closed loop simplifies to [8, p. 361]

$$2a_n = - \oint_C \mathbf{e}_n^+ \cdot \boldsymbol{\tau} dl = j\omega\mu_0 \iint_S \mathbf{h}_n^+ d\mathbf{s}' = V_n^+, \quad (3.49a)$$

$$2b_n = - \oint_C \mathbf{e}_n^- \cdot \boldsymbol{\tau} dl = j\omega\mu_0 \iint_S \mathbf{h}_n^- d\mathbf{s}' = V_n^-. \quad (3.49b)$$

The induced voltage V_n^+ is related to the fields \mathbf{e}_n^+ and \mathbf{h}_n^+ at the output port located in positive z -direction, while the induced voltage V_n^- is related to the fields at the other output port \mathbf{e}_n^- and \mathbf{h}_n^- . For the TEM mode, the total induced voltage equals $V_{\text{TEM}} = V_{\text{TEM}}^- - V_{\text{TEM}}^+$. The relation to the magnitude of the magnetic dipole moment m_m is expressed as

$$m_m = \frac{a_{\text{TEM}} - b_{\text{TEM}}}{e_{\text{TEM}}^\pm \cdot k_0} = \frac{V_{\text{TEM}}}{e_{\text{TEM}}^\pm \cdot k_0}. \quad (3.50)$$

For the TE₀₁ mode, the total induced voltage equals $V_{\text{TE01}} = V_{\text{TE01}}^- + V_{\text{TE01}}^+$.

In the general case, a magnetic dipole moment \mathbf{m}_m producing fields characterized with coefficients a_n and b_n models the magnetic coupling behavior of any electrically small antenna yielding the same coefficients. Consequently, deriving an equivalent magnetic dipole moment \mathbf{m}_m of an electrically small antenna is possible by measuring a_n and b_n at the output ports.

In a similar manner to Equations (3.48a) and (3.48b), a constant magnetic field \mathbf{h}_n^\pm along a magnetic current I_m following a curve C makes the following expression possible:

$$2a_n = - \int_C \boldsymbol{\tau} I_m(l) \cdot \mathbf{h}_n^+ dl, \quad (3.51a)$$

$$2b_n = - \int_C \boldsymbol{\tau} I_m(l) \cdot \mathbf{h}_n^- dl. \quad (3.51b)$$

Analogous to Equations (3.49a) and (3.49b), I_m is assumed to be constant and C to form a closed loop, leading to

$$2a_n = - \oint_C \mathbf{h}_n^- \cdot \boldsymbol{\tau} dl = -j\omega\epsilon_0 \iint_{S_0} \mathbf{e}_n^+ d\mathbf{s}', \quad (3.52a)$$

$$2b_n = - \oint_C \mathbf{h}_n^+ \cdot \boldsymbol{\tau} dl = -j\omega\epsilon_0 \iint_{S_0} \mathbf{e}_n^- d\mathbf{s}'. \quad (3.52b)$$

Now, the surfaces S_1 and S_2 are defined, which are depicted in Figure 3.11. Surface S_1 starts from S_0 and runs parallel to the electric field \mathbf{e}_n^\pm , extending infinitely. A total surface is defined as $S = S_0 + S_1 + S_2$, where S_2 closes the total surface around S_1 at infinity.

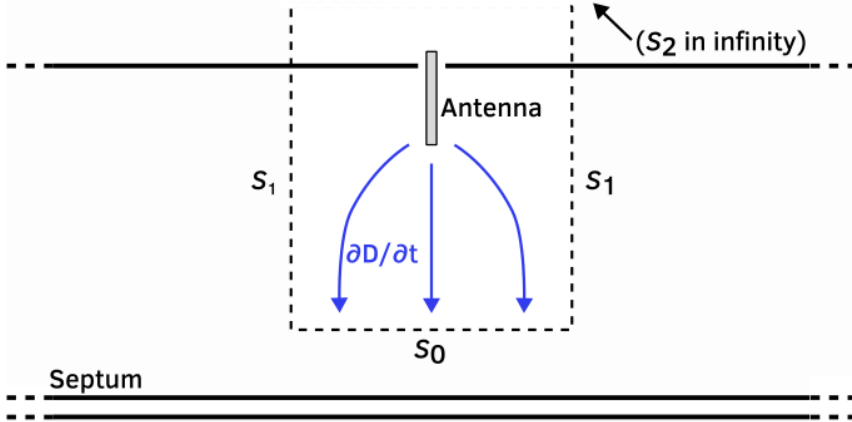


Figure 3.11 Sketch of the surfaces S_0 , S_1 and S_2 in the TEM cell with an example antenna, coupling through S_0 to the septum over the displacement current $\partial\mathbf{D}/\partial t$.

Consequently, Equations (3.52a) and (3.52b) can be written with the newly defined closed surface S as

$$j\omega\epsilon_0 \iint_S \mathbf{e}_n^\pm \cdot d\mathbf{s}' = j\omega\epsilon_0 \iint_{S_0} \mathbf{e}_n^\pm \cdot d\mathbf{s}' + \underbrace{j\omega\epsilon_0 \iint_{S_1} \mathbf{e}_n^\pm \cdot d\mathbf{s}'}_{=0} + \underbrace{j\omega\epsilon_0 \iint_{S_2} \mathbf{e}_n^\pm \cdot d\mathbf{S}}_{=0}. \quad (3.53)$$

Inserting Gauss' law $\nabla \cdot \mathbf{E} = \frac{\rho}{\epsilon_0}$ leads to

$$-j\omega\epsilon_0 \iint_S \mathbf{e}_n^\pm \cdot d\mathbf{s}' = -j\omega\epsilon_0 \iiint_V \nabla \cdot \mathbf{e}_n^\pm \cdot dv' = -j\omega \iiint_V \rho_n^\pm \cdot dv'. \quad (3.54)$$

With the continuity equation $j\omega\rho = -\nabla \cdot \mathbf{J}$ this yields

$$2a_n = -j\omega \iiint_V \rho_n^+ \cdot dv' = \iiint_V \nabla \cdot \mathbf{J}_n^+ \cdot dv' = \oint_S \mathbf{J}_n^+ \cdot d\mathbf{s}' = I_n^+, \quad (3.55a)$$

$$2b_n = -j\omega \iiint_V \rho_n^- \cdot dv' = \iiint_V \nabla \cdot \mathbf{J}_n^- \cdot dv' = \oint_S \mathbf{J}_n^- \cdot d\mathbf{s}' = I_n^-. \quad (3.55b)$$

For the TEM mode, the electric dipole moment magnitude m_e can be expressed in terms of the total current $I_{\text{TEM}} = I_{\text{TEM}}^+ + I_{\text{TEM}}^-$ by substituting (3.55a) and (3.55b) into (3.46a), yielding

$$m_e = \frac{a_{\text{TEM}} + b_{\text{TEM}}}{e_{\text{TEM}}^\pm} = \frac{I_{\text{TEM}}}{e_{\text{TEM}}^\pm}. \quad (3.56)$$

An electric dipole moment \mathbf{m}_e producing fields characterized with coefficients a_n and b_n models the electric coupling behavior of any electrically small antenna yielding the same coefficients. Consequently, deriving an equivalent \mathbf{m}_e of an electrically small antenna is possible by measuring a_n and b_n at the output port, analogous to the case of \mathbf{m}_m .

The physical meaning of I_n is the electrical current passing between the septum and the dipole via capacitive coupling, representing the displacement current. In summary, the magnetic dipole moment arises from the induced voltage on the septum, whereas the electric dipole moment results from the coupling displacement current.

3.6 Shielding

3.6.1 Electromagnetic shielding mechanisms

The following section outlines the fundamental theory of electromagnetic shielding. Throughout this thesis, all materials are assumed to be linear and isotropic.

A commonly used figure of merit for quantifying the shielding capability of a material is the electromagnetic shielding effectiveness SE . It is defined as the ratio of the incident to the transmitted electric field amplitude, expressed on a logarithmic scale in decibels as in [9, 16, p. 63]

$$SE_{\text{dB}} = 20 \log_{10} \left(\frac{E_i}{E_t} \right), \quad (3.57)$$

where E_i and E_t denote the magnitudes of the incident and transmitted electric field, respectively, as shown in Figure 3.12. An analogous expression holds for the magnetic field components. Higher values of SE_{dB} indicate greater attenuation of the electromagnetic field.

An electromagnetic wave incident on a shielding material may be partially reflected at the surface, partially absorbed within the material, and reflected multiple times internally before the remainder is transmitted. The total shielding effectiveness is determined by [16, p. 63]

$$SE_{\text{dB}} = R_{\text{dB}} + A_{\text{dB}} + B_{\text{dB}}, \quad (3.58)$$

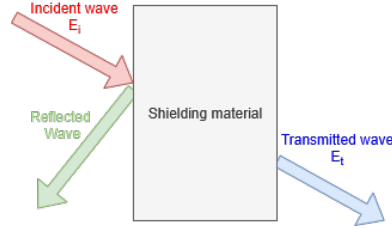


Figure 3.12 Incident, reflected and transmitted electric field intensities at a shielding material.

according to Schelkunoff's approach to shielding [30]. Absorption losses A_{dB} arise from waves propagating through the shield, R_{dB} denotes reflections at the material's surface, and B_{dB} is a correction factor that accounts for multiple reflections within the shield [9].

Reflections contribute most significantly to a material's shielding effectiveness [16, p. 1]. They are characterized by the reflection coefficient R . For a material to reflect incident fields, it must possess free charge carriers. For this reason, highly conductive materials, such as metals, reflect the majority of incident electromagnetic waves.

Reflections are caused by wave impedance mismatch between two materials. It is common practice to normalize the wave impedance η_n by the free-space wave impedance η_0 when determining the reflection coefficient R . At the interface between free space and a shielding material, this yields [8, p. 183]

$$R = \frac{\eta_n - 1}{\eta_n + 1}. \quad (3.59)$$

The normalized wave impedance is given by

$$\eta_n = \frac{1}{\eta_0} \sqrt{\frac{j\omega\mu}{\sigma + j\omega\epsilon}}. \quad (3.60)$$

Electric fields dominate in the near-field region of electric dipoles, as discussed in Section 2.1 and demonstrated with (2.11). Consequently, the wave impedance in this region is very high. For effective shielding by reflection, the shielding material should possess high permittivity and high conductivity to achieve a low impedance (see Equation 3.60), creating the necessary impedance mismatch for reflection [16, p. 67].

In contrast, magnetic fields are predominant in the near-field region of magnetic dipoles, as demonstrated with Section 2.2, specifically with (2.19). A high conductivity shields well against high-frequency magnetic fields due to the creation of counter-acting eddy currents [16, p. 112]. Low-frequency magnetic fields are difficult to shield, and the most common approach is the redirection of magnetic flux lines due to high permeability of the shielding material [16, pp. 112-113].

The portion of the electromagnetic wave that is not reflected is subject to absorption within the shielding material. This phenomenon is described by A_{dB} and accounts for

an exponentially decreasing amplitude of an electromagnetic wave in a lossy medium. In conductive materials, this phenomenon is closely related to the skin depth.

The skin effect describes the interaction of electromagnetic waves with conductors, causing eddy currents to form on the surface. To investigate this phenomenon, the complex wavenumber is introduced $\tilde{k} = k + j\kappa$, which assists in mathematically describing waves propagating in lossy materials. The imaginary part κ is expressed as

$$\kappa = \omega \sqrt{\frac{\epsilon\mu}{2}} \left[\sqrt{1 + \left(\frac{\sigma}{\epsilon\omega} \right)^2} - 1 \right]^{1/2}. \quad (3.61)$$

The skin depth d is described by

$$d = 1/\kappa. \quad (3.62)$$

For highly conductive materials ($\sigma \gg \epsilon\omega$) the skin depth is $d \propto 1/\sqrt{\omega}$. Therefore, high-frequency electromagnetic waves do not penetrate deeply into conductive materials, due to the free electrons associated with high conductivity absorbing the waves with eddy currents on the material's surface and transforming the energy into heat. A material's permeability further reduces the skin depth due to the increased susceptibility to eddy currents [16, p. 104].

For non-conductive materials, absorption depends on the electric loss factor [16, pp. 102-103], as further described in Section 3.6.2.

Upon reaching the far end of the shielding material, re-reflections can occur. When the material thickness is greater than the skin depth, the correction factor for this effect B_{dB} can be neglected. When the material thickness is smaller than the skin depth, however, the internal reflections reduce the shielding effectiveness by destructively interfering with the reflected waves, and the value of B_{dB} is negative [16, p. 1].

3.6.2 Conductivity, permeability and permittivity in shields

When molecules in a material are exposed to an electric field, they become polarized. This property is characterized by the material's permittivity ϵ . Exposure to a magnetic field causes the spins of electrons within atoms to align with the field, described by the material's permeability μ . When these electric and magnetic fields vary with time, the molecules continuously move and realign, resulting in the movement of charges, which is quantified by the conductivity σ . The energy lost in this dynamic process is dissipated as heat [2, p. 68].

The electric field pushes charges in polarizable molecules apart. This separation of charges may be described as an electric dipole, depending on the separation distance and the charge. Under alternating electric fields, the movement of charges contributes to σ . This phenomenon is called dielectric hysteresis. It is quantified by the loss tangent $\tan \delta_e$, and defined as [2, pp. 73-74]

$$\tan \delta_e = \frac{\sigma_s}{\omega \epsilon'} + \frac{\epsilon''}{\epsilon'}. \quad (3.63)$$

There, σ_s is the static conductivity, indicating the conductivity of the material for constant fields over time. The complex part of the permittivity ϵ'' describes the lossy part of the dielectric material, specifically relevant for alternating fields over time. The real part of the permittivity is lossless and is denoted by ϵ' , and corresponds to the material's ability to store electric energy [23]. The overall complex permittivity is therefore $\epsilon = \epsilon' + j\epsilon''$.

The loss tangent therefore relates the conductivity of a material to the real permittivity. A dielectric with low losses has a much larger displacement current than conduction current density ($\tan \delta_e \ll 1$). The opposite is true for a good conductor ($\tan \delta_e \gg 1$) [2].

Analogous to polarizable materials, there are also magnetizable lossy materials, which are characterized by a complex permeability $\mu = \mu' + j\mu''$. The real part of the permeability μ' describes the material's ability to store magnetic energy, while μ'' describes the magnetic losses [23]. The complex permeability can also be described by a magnetic loss tangent $\tan \delta_m$, as shown in

$$\tan \delta_m = \frac{\mu''}{\mu'}. \quad (3.64)$$

The loss tangent is very low for the majority of materials. Ferrites are a notable exception and are commonly used to attenuate high-frequency signals [2, p. 80].

3.6.3 ASTM ES7-83 Method

The ASTM ES7-83 method is used to determine the shielding effectiveness of shielding materials in far-field conditions. The shielding material is inserted into a TEM cell around the septum. Ideally, the shielding material forms a continuous connection with the TEM cell [27].

In this method, two measurements are performed at the output ports of the TEM cell. In the first measurement, an empty TEM cell is excited and a reference output voltage U_{ref} is measured. In the second, the TEM cell is loaded with the shielding material, and the output voltage U_{load} is again noted. The shielding effectiveness SE_{dB} is then derived with the obtained measurement values by [27]

$$SE_{\text{dB}} = 20 \cdot \log \left(\frac{U_{\text{ref}}}{U_{\text{load}}} \right). \quad (3.65)$$

When applying numerical analysis in combination with this method, it is more convenient to define a reference output power P_{ref} for an unloaded TEM cell, and an output power for the loaded case P_{load} . This leads to a similar expression,

$$SE_{\text{dB}} = 10 \cdot \log \left(\frac{P_{\text{ref}}}{P_{\text{load}}} \right). \quad (3.66)$$

Figure 3.13b shows the cross section of this shielding material, which is inserted into the TEM cell. In Figure 3.13a the shielding material can be seen wrapped around the septum.

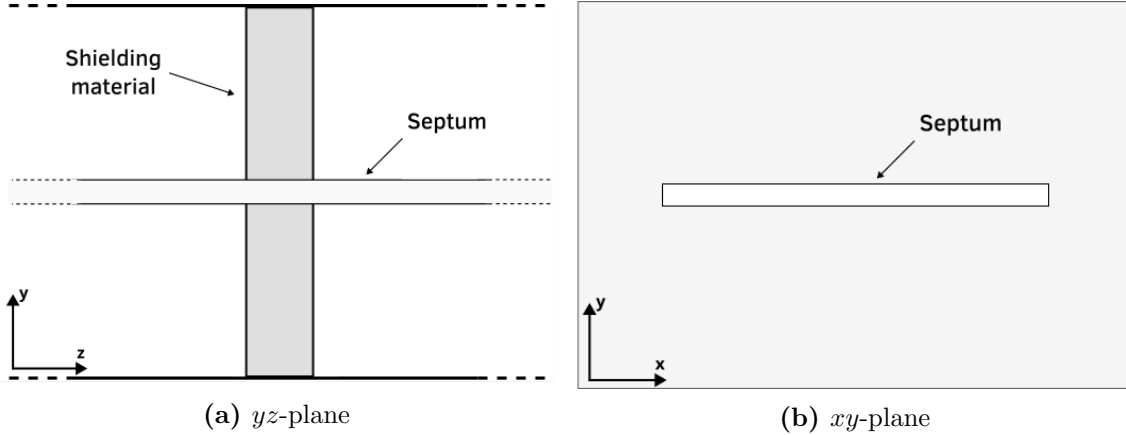


Figure 3.13 Cross section of shielding material in TEM cell

Then, the S-parameters derived in the simulations are used to determine the output powers P_{ref} and P_{load} . By exciting the TEM cell with a power of 1 W, the reference power is $P_{\text{ref}} = 1 \text{ W}$. The measured power is then derived through

$$P_{\text{load}} = P_{\text{ref}} \cdot 10^{S_{12,\text{dB}}/10}. \quad (3.67)$$

3.6.4 Dual TEM cell

The shielding effectiveness of a material may also be determined using a dual TEM cell shown in Figure 3.14. The two cells are connected through an aperture, which can be filled with the shielding material or left empty. The upper TEM cell is excited through port 1, and acts as a driving cell, transmitting power through the aperture. Port 2 is loaded with the reference impedance $Z_w \approx 50 \Omega$. The second TEM cell functions as a receiver, collecting power at its output ports [27].

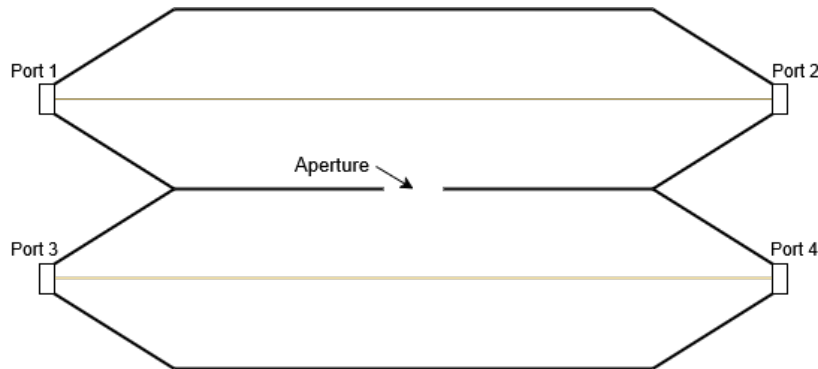


Figure 3.14 Dual TEM cell with aperture

If the aperture is electrically small, its coupling may be described by an electric and a

magnetic dipole moment. Their magnitude is related to the electric and magnetic coupling between the TEM cells over the aperture. Therefore, the electric and magnetic coupling can be determined separately by adding or subtracting the output powers of the receiving TEM cell [27, 38]. Consequently, an electric shielding effectiveness SE_{dB}^e and a magnetic shielding effectiveness SE_{dB}^m can be calculated with

$$SE_{dB}^e = 10 \log \left(\frac{P_{ref,sum}}{P_{load,sum}} \right), \quad (3.68a)$$

$$SE_{dB}^m = 10 \log \left(\frac{P_{ref,diff}}{P_{load,diff}} \right). \quad (3.68b)$$

Separating the electric and magnetic shielding effectiveness is useful when applying shielding materials in the near field of electric or magnetic dipole moments. For shielding a magnetic dipole moment, the SE_{dB}^m value is considered significant [38], whereas for an electric dipole moment, the SE_{dB}^e value is relevant.

4 Finite Element Method

4.1 Overview

The calculation of electromagnetic fields poses significant challenges, as it requires solving differential equations over a computational domain that, for arbitrary geometries, generally cannot be solved analytically. Ansys HFSS (High-Frequency Simulation Software) addresses this challenge, and as it is used as the basis of the simulations presented in Section 4, a dedicated description of its underlying methodology is given in the following section.

HFSS employs the Finite Element Method (FEM) as its underlying numerical technique. Following the Rayleigh-Ritz-Galerkin approach, the general idea is to approximate the solution as a linear combination of basis functions, such that the governing differential equation is satisfied as closely as possible. This reformulates the problem of solving a differential equation into a system of algebraic equations that can be efficiently processed computationally. In principle, a suitable set of basis functions exists for which the solution converges to the exact result. In practice, however, the number of basis functions employed across the computational domain must be kept finite, due to limitations in computational resources [33].

FEM achieves this by subdividing the computational domain into a finite number of smaller subregions, referred to as finite elements, within each of which a basis function is defined. A linear combination of these basis functions is then determined such that the governing differential equations are satisfied across the entire domain. In regions where the approximation error exceeds a threshold level, the accuracy can be improved by further subdividing the elements containing the largest error values. This process is repeated iteratively until the error falls below a prescribed threshold, yielding a sufficiently accurate solution.

4.2 Dividing a computational domain into finite elements

The differential equation to be solved is expressed as

$$\nabla \times \left(\frac{1}{\mu_r} \nabla \times \mathbf{E} \right) - k_0^2 \epsilon_r \mathbf{E} = 0 \quad \text{in } V, \quad (4.1)$$

where the variable k_0 is the wave number of free space and equals $k_0 = \omega \sqrt{\epsilon_0 \mu_0}$ [7, 24, 6].

The wave equation is solved over a computational domain V , which is subdivided into a collection of finite elements referred to as a mesh. Each node in this mesh is assigned polynomial basis functions, which are weighted to approximate the real solution. Tetrahedral finite elements have been shown to be particularly well-suited for this purpose, as they are geometrically flexible and enable the construction of complete polynomial approximation functions [31].

Ansys HFSS employs an adaptive finite element mesh generator that automatically discretizes arbitrary three-dimensional geometries. The Delaunay tessellation algorithm serves as the underlying meshing strategy. It efficiently generates the mesh to represent geometrically irregular structures by ensuring that no vertex of the mesh lies inside the circumsphere of any tetrahedron. It further permits boundary conditions to be applied recursively to the derived mesh. Iterative mesh refinement can additionally be carried out without introducing any distortion to the original geometry [7].

Figure 4.1 shows one such tetrahedron. At the edge midpoints, the field components normal to the respective edge and lying on the face of the element are stored, while at the vertex points, the field components tangential to the edges are stored. The field value at any point within the tetrahedron is then obtained by interpolating from the nodal values using the associated basis functions.

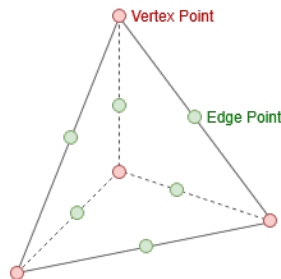


Figure 4.1 Tetrahedron with points on the edge and vertices.

The finite elements used in HFSS are known as tangential vector finite elements. Their advantage is that the tangential components of the field are enforced to be continuous across the boundaries between adjacent tetrahedra. Specifically, the electric field intensity assigned to an edge is constrained to be aligned with that edge, making it tangential to the element. Adjacent elements sharing this edge therefore contain the same electric field intensity, ensuring continuity of the tangential electric field intensity across element boundaries. The boundary conditions imposed by Maxwell's equations are thereby automatically satisfied. In addition, Dirichlet boundary conditions can be enforced along the

edges of the mesh [24].

The finite element is described as

$$H_1^{(\text{dim}=3)}(\text{curl}) = \left\{ \mathbf{u} \mid \mathbf{u} \in [L_2(V)]^3, \nabla \times \mathbf{u} \in [P_1(V)]^3 \cap D(V) \right\}, \quad (4.2)$$

where $L_2(V)$ is a set of square integrable functions and P_1 a set of piecewise linear functions in the discretized domain V [25]. The vector field within each element is denoted as \mathbf{u} . $D(V)$ is a set of divergence-free functions. The vectors \mathbf{u} used in the finite element are therefore continuous in the normal direction, square integrable, and have a curl describable by piecewise linear functions.

Figure 4.2 shows the finite element with the unknown vectors assigned at each node, where only one face is shown for clarity. The variables u_i^j and u_j^i are imposed across element boundaries, therefore guaranteeing tangential continuity at boundaries. Additionally, they inherently define a linear polynomial along the shared edge, meaning that they describe a gradient of the field in this direction. This relationship is expressed as

$$\mathbf{u} \cdot \mathbf{t}_{ij} = \frac{1}{l_{ij}} (u_i^j - u_j^i), \quad (4.3)$$

where \mathbf{t}_{ij} is the unit vector tangent to the edge from node i to node j and l_{ij} is the length of this edge.

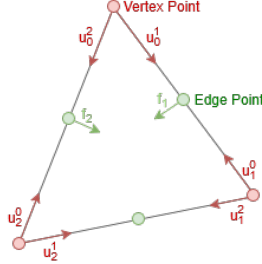


Figure 4.2 Face of the finite element with unknowns

Two additional unknowns are introduced, f_1 and f_2 , which are assigned to two of the three edge points on a given face. Contrary to the variables u_i^j , the facial unknowns f_i are only assigned locally at each element and do not propagate across boundaries. Their purpose is to introduce a quadratic polynomial representation for the field component normal to the edges, which in turn yields a linear approximation for the curl of the unknown vector field $\nabla \times \mathbf{u}$, providing sufficient accuracy for the solution. The total vector field of the element is then obtained by superposition of all nodes' vector contributions.

4.3 Solving the differential equation

A testing function \mathbf{W}_n is defined, by which (4.1) is multiplied. Integrating over the whole test volume then leads to

$$\int_V \left(\mathbf{W}_n \cdot \nabla \times \left(\frac{1}{\mu_r} \nabla \times \mathbf{E} \right) - k_0^2 \epsilon_r \mathbf{W}_n \cdot \mathbf{E} \right) dv' = 0. \quad (4.4)$$

This yields N equations, indexed by $n = 1, 2, \dots, N$, one for each finite element in the domain V . This is a standard procedure in FEM, and is achieved by orthogonalizing the residual of (4.1) with respect to the test functions \mathbf{W}_n [26].

Applying the vector identity $\nabla \cdot (\mathbf{a} \times \mathbf{b}) = (\nabla \times \mathbf{a}) \cdot \mathbf{b} - \mathbf{a} \cdot (\nabla \times \mathbf{b})$ to the first term of (4.4) yields a weak form of the equation, that is, a reformulation of the original partial differential equation in which the order of the derivatives is reduced [7, 14]. This procedure also introduces boundary terms, permitting the incorporation of Neumann boundary conditions [26]. The boundary terms appear on the right-hand side of the resulting expression,

$$\int_V \left[(\nabla \times \mathbf{W}_n) \cdot \frac{1}{\mu_r} \nabla \times \mathbf{E} - k_0^2 \epsilon_r \mathbf{W}_n \cdot \mathbf{E} \right] dv' = \underbrace{\oint_{\partial V} \left(\mathbf{W}_n \times \frac{1}{\mu_r} \nabla \times \mathbf{E} \right) \cdot d\mathbf{s}'}_{\text{Boundary term}}. \quad (4.5)$$

The electric field \mathbf{E} is represented as a superposition of basis functions. Applying Galerkin's method, in which the basis functions are chosen equal to the test functions \mathbf{W}_n , this superposition takes the form

$$\mathbf{E} = \sum_m^N x_m \mathbf{W}_m, \quad (4.6)$$

where x_m are the corresponding weighting coefficients. Determining these coefficients for all elements yields the electric field \mathbf{E} across the entire computational domain. Through this procedure, FEM reduces the wave equation given in (4.1) to a linear matrix equation of the form $Ax = b$, where A is a known $N \times N$ matrix, b encodes the port excitations, and x is the vector of unknown coefficients. The matrix A is expressed as

$$\begin{aligned} A_{ij} = & \int_V \nabla \times \mathbf{W}_i \frac{1}{\mu_r} \nabla \times \mathbf{W}_j dv' \\ & - k_0^2 \int_V \mathbf{W}_i \epsilon_r \mathbf{W}_j dv' \\ & + jk_0 \left(\frac{\eta_0}{\eta_s} \right) \oint_{\partial V} \mathbf{n} \times \mathbf{W}_i \cdot \mathbf{n} \times \mathbf{W}_j d\mathbf{s}'. \end{aligned} \quad (4.7)$$

The boundary term is expressed in terms of the surface impedance η_s , where η_s defines the ratio of the electric field intensity to the magnetic field intensity at the boundary. Since the basis functions are defined to vanish outside their associated elements, the resulting matrix A is sparse, as entries corresponding to non-overlapping test and basis functions

are identically zero. This sparsity significantly reduces the computational cost of solving the system. Once the electric field has been obtained, all other electromagnetic quantities of interest can be derived from it.

4.4 Adaptive solution process

Each finite element is assigned a solved electric field that approximates the true solution within that element. The error associated with each element is assessed by evaluating (4.1) for the solved field, yielding a residual as expressed by

$$\nabla \times \left(\frac{1}{\mu_r} \nabla \times \mathbf{E}_{\text{solved}} \right) - k_0^2 \epsilon_r \mathbf{E}_{\text{solved}} = \text{residual}. \quad (4.8)$$

Elements exhibiting the largest residuals represent the greatest local deviation from the true solution, and are therefore identified as the regions of highest error.

Regions of the mesh exhibiting large errors are refined by splitting the tetrahedral finite elements into smaller ones, allowing the FEM solver to recalculate the fields in these regions with higher precision and thus reducing the residual. The smaller element size and higher spatial resolution consequently improve the accuracy with which the finite elements represent the fields [5]. An alternative approach to improving accuracy is to increase the polynomial order of the basis functions within elements of large residual, without further subdividing them.

To determine when the iterative refinement process has converged to a sufficiently accurate solution, a convergence threshold must be defined. The criterion used is the Max ΔS parameter, which is evaluated by comparing the S-parameters of the analyzed structure between two consecutive iterations. If the change in S-parameters falls below this threshold following a mesh refinement, the solution is considered to have converged and the iterative process is terminated. This process is shown in Figure 4.3.

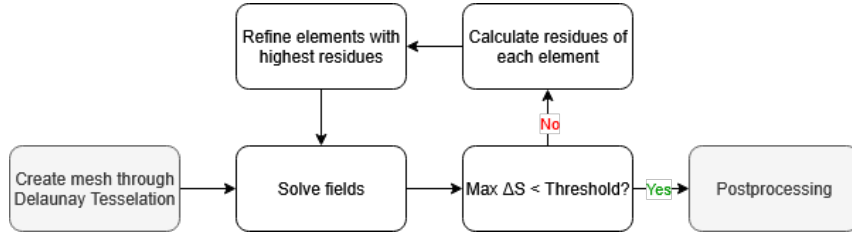


Figure 4.3 Adaptive solution process

5 Numerical Investigations of Antennas in TEM Cells

5.1 Simulation Setup and Modeling Assumptions

5.1.1 Antenna models

Every antenna is excited through a round waveport feedpoint, shown in Figure 5.1. The feedpoint provides an incident wave of unit power (1 W). The antenna wires are modeled

as perfect electric conductors (PECs) with a diameter of 0.2 mm. The geometry is intentionally kept simple, with the cylindrical wires pointing either in x -, y - or z -direction, without combining multiple orientations, which isolates orientation-dependent coupling effects.

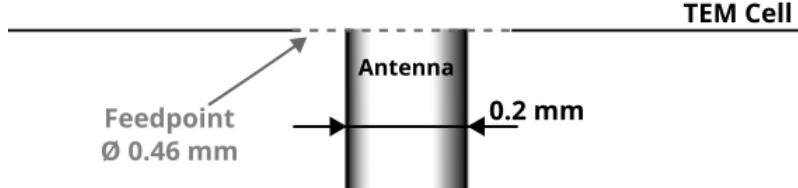


Figure 5.1 Geometry of an antenna's feedpoint used in simulation. The antenna is fed through a round waveport of diameter 0.46 mm and consists of a PEC wire with a diameter of 0.2 mm. This geometry leads to a reference impedance of $Z_0 \approx 50 \Omega$.

The investigations in this thesis focus on the coupling behavior of antennas. All conducting surfaces are modeled as PECs to remove the influence of lossy conductors, which are especially significant due to the Skin-effect. Conductor losses contribute to the power consumption of the small loop antenna, for example, and are significantly larger than the radiated power [3, p. 231].

Neglecting conductor losses increases the quality factor of the model. As a consequence, resonance effects can appear more pronounced than in a physically lossy implementation. This limitation must be considered when interpreting the numerical results.

The first two antennas investigated are the monopole (Section 5.2) and the loop antenna (Section 5.3), which represent the most fundamental antenna types producing electric and magnetic dipole moments, respectively. Other electrically small antennas yield similar results depending on whether they are capacitive or inductive. Capacitive antennas are analogous to the monopole, while inductive antennas are analogous to the loop antenna, with both analogies extending to their respective equivalent circuits, meaning the same coupling and impedance behavior applies.

5.1.2 TEM cell model

The TEM cell model used, shown in Figure 3.4, has a width of $a = 40$ mm, a height of $b = 24$ mm and a length of $l = 100$ mm. The cut-off frequencies of higher-order modes are demonstrated in Figure 3.5. In the following numerical investigations focusing on the TEM mode, the frequency range of interest spans from 1 MHz to 3 GHz. If the TE_{01} mode is included in the investigations, the upper limit of the frequency range is extended to 3.3 GHz.

The cell walls and septum are modeled as PECs. In the TEM cell simulation model, the tapered transition sections at the ports are omitted. As discussed in Section 3.4.1, this simplification removes the physical cutoff imposed by the tapered transitions, permitting higher-order modes to propagate freely, thereby facilitating investigations of their coupling behavior with the antennas and dipole moments. The reference impedances of the output ports equal $Z_w \approx 50 \Omega$.

Upon exciting the output ports, the electric and magnetic energy W_e and W_m stored in the TEM cell are derived by (2.24). The current and voltage at the output ports are found with (5.4) and (5.5), respectively. The capacitance and inductance of the TEM cell are then given by (2.25a) and (2.25b). The extracted TEM cell reactances are found to be approximately constant over frequency, yielding values of $C_T = 6.74 \text{ pF}$ and $L_T = 16.25 \text{ nH}$.

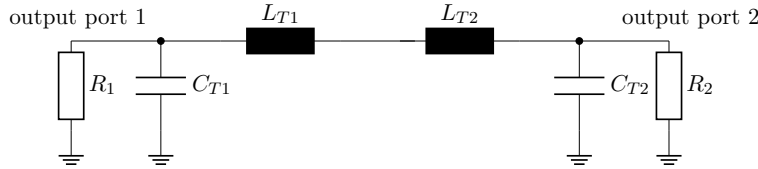


Figure 5.2 Circuit representing the TEM cell, where the capacitance and inductance are split into two separate, equal components $C_T = C_{T1} + C_{T2}$, $L_T = L_{T1} + L_{T2}$ and $C_{T1} = C_{T2}$, $L_{T1} = L_{T2}$. The resistances R_1, R_2 at the output ports model the reference impedance $Z_w \approx 50 \Omega$.

5.1.3 Dipole moment models

The dipole moments implemented in the numerical simulations are infinitesimally small and exhibit the behaviors discussed in Section 2.1.1 and Section 2.2. Consequently, all previous discussions and conclusions derived in this thesis regarding dipole moments are directly applicable to the dipole moment models employed in the following numerical investigations.

A magnetic dipole moment can be expressed equivalently as either an electric current I_0 flowing in a loop or a magnetic current I_m along a line, as described in (2.16). For the following numerical investigations, the magnetic dipole moment is taken in the form given in (2.15), which represents an equivalent formulation in terms of a magnetic current I_m along an infinitesimal line.

The electric and magnetic dipole moments are placed at the center of the TEM cell at $x = 0$, $y = b/2$, $z = 0$. As discussed in Section 3.4.2, $\mathbf{e}_{\text{TEM}}^\pm$ has only a y -component at this location, while $\mathbf{h}_{\text{TEM}}^\pm$ has only an x -component. Consequently, the equivalent electric dipole moment \mathbf{m}_e is oriented exclusively along the y -direction, and the magnetic dipole moment \mathbf{m}_m along the x -direction. Placing \mathbf{m}_m and \mathbf{m}_e at the center of the TEM cell therefore significantly simplifies the modeling of electrically small antennas with equivalent dipole moments, as only one component of each dipole moment must be considered. This assumption holds as long as only the TEM mode occurs and must be revised once higher-order modes propagate. Unless otherwise stated, this configuration is adopted throughout all numerical investigations presented in this thesis.

When normalizing to the free-space wave impedance η_0 , \mathbf{m}_e can be interchanged with an equivalent \mathbf{m}_m and vice-versa [15, p. 414]. Therefore, normalizing either \mathbf{m}_e or \mathbf{m}_m to the free-space wave impedance η_0 enables a meaningful comparison between them.

5.1.4 Mesh settings

The mesh determines the resolution of the field quantities over the computational domain. Since electrically small conductors are involved, implementing small mesh elements in their proximity is necessary for accurate modeling of near-fields. Adaptive meshing algorithms may fail to refine these regions, due to the low impact of these near-fields on the solution of the overall computational domain. Consequently, adjusting mesh element sizes does not significantly influence the overall solution of the model, but greatly improves the accuracy of near-field investigations.

The maximum mesh element length in error-prone volumes is adjusted until the obtained results show a reasonably low amount of numerical artifacts. Critical regions are commonly located near feedpoints and along edges of small conductors, where large field intensities occur within small spatial regions. The simulation models created for this thesis use roughly 15 elements on the surfaces of such critical volumes to achieve a reasonable representation of these regions while avoiding excessively large meshes.

Lastly, it is best practice to select the upper limit of the investigated frequency range as the solution frequency. This choice produces the largest spatial field changes, forcing the adaptive mesh process to generate a high-resolution mesh. Results at frequencies below the solution frequency are computed on the same mesh, which is finer than strictly necessary at those frequencies, providing additional accuracy. This procedure is applied for every numerically derived frequency-dependent result presented in this thesis.

5.1.5 Shielding material models

The numerical investigation of large computational domains containing thin shielding material requires a large number of mesh elements for accurate representation of fields around the shield. Especially in the analysis of the ASTM ES7-83 method in Section 6.1, accurately resolving the thin shielding material requires a large number of mesh elements, resulting in high computational effort. A solution is to impose boundary conditions on the shielding material's surface, as described in [4].

In this approach, the shielding material is removed from the computational domain and replaced by boundary conditions imposed on its surface. The simulator assumes plane wave propagation normal to the surface, which is a good approximation for the shielding material in the ASTM ES7-83 method, since its surfaces are oriented perpendicular to the wave propagating within the TEM cell.

5.1.6 S-parameters and derived data

The TEM cell containing an antenna is modeled as a three-port network. The two output ports of the TEM cell are denoted as ports 1 and 2, while the antenna feedpoint is marked as port A. The behavior of this system is fully characterized by its scattering matrix, given as

$$[S] = \begin{bmatrix} S_{11} & S_{12} & S_{1A} \\ S_{21} & S_{22} & S_{2A} \\ S_{A1} & S_{A2} & S_{AA} \end{bmatrix}. \quad (5.1)$$

The coupling between the antenna and the two ports of the TEM cell is described by S-parameters, specifically the forward transmission coefficients S_{A1} and S_{A2} . The phases of the forward transmission coefficients Φ_{A1} and Φ_{A2} provide information on the phase shift between the incident wave at port A, and the transmitted wave at output ports 1 and 2. This phase shift influences the magnitude of the magnetic and electric dipole moments, as discussed in Section 3.5.2. The magnitude of this coefficient is equal for both ports, $|S_{A1}| = |S_{A2}|$, provided that the antenna is positioned sufficiently far from the output ports. The power transferred from the antenna P_A to the output ports P_1 and P_2 is derived through

$$P_A = \frac{P_1}{10^{S_{A1,\text{dB}}/10}} = \frac{P_2}{10^{S_{A2,\text{dB}}/10}}. \quad (5.2)$$

If the normalized electric field distribution of the TEM mode $\mathbf{e}_{\text{TEM}}^{\pm}$ is unknown, it may be directly derived from the electric field intensity at the output port by setting the excitation power to $P_1 = P_2 = 1/2$ W, as demonstrated by (3.39a) and (3.39b). For example, the uniformly distributed, normalized electric field of the TEM mode along the y-axis at the center of the TEM cell ($z = 0, x = 0$) is derived by

$$|a_{\text{TEM}}| \cdot \mathbf{e}_{\text{TEM}}^+(x = 0, y, z = 0) = \frac{\sqrt{P_1 Z_0}}{b/2}. \quad (5.3)$$

The peak value of the current through the feedpoint is calculated with the S-parameters:

$$I_A = \sqrt{2P_A} \frac{(1 - S_{AA})}{\sqrt{Z_0}}, \quad (5.4)$$

where P_A is the incident power wave applied to the feedpoint, and is set to unit power (1 W) as stated previously in Section 5.1.1. The peak voltage at the feedpoint is analogously given by

$$V_A = \sqrt{2P_A}(1 - S_{AA})\sqrt{Z_0}. \quad (5.5)$$

Another method to derive voltages and currents at arbitrary points in the computational domain is by integration of field intensities. Sufficient mesh refinement in the integration region is necessary to reduce numerical errors, as discussed in Section 5.1.4. The impedance seen from the antenna feedpoint is:

$$Z_A = Z_0 \frac{1 + S_{AA}}{1 - S_{AA}}. \quad (5.6)$$

5.1.7 Investigation of Field Regions

This section investigates whether the frequency-dependent non-linear behavior is intrinsic to the antenna's geometry or whether it is influenced by the dominant coupling field region within the TEM cell.

To isolate these effects, a numerical analysis was conducted using two TEM cells of significantly different sizes, as shown in Figure 5.3. By scaling the cell geometry while maintaining a constant characteristic impedance, the physical distance r between the source and the septum changes, thereby shifting the $k \cdot r$ factor across the frequency spectrum. If the normalized output power remains consistent between the two configurations, it confirms that the coupling mechanism is invariant to the specific field region and is primarily defined by the source's dipole moments.

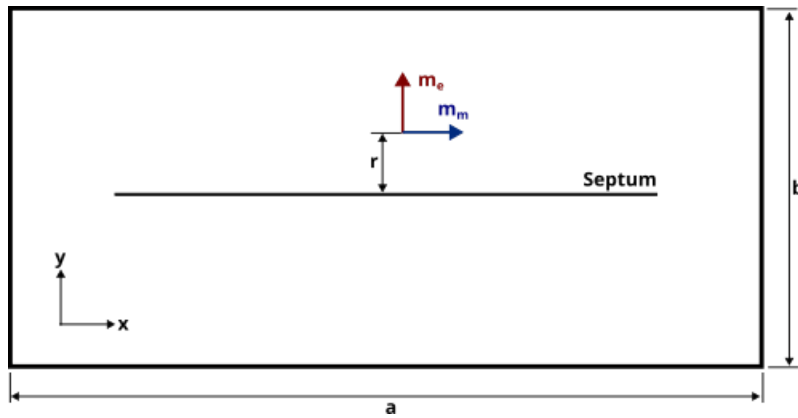


Figure 5.3 Numerical model of a TEM cell containing an electric moment \mathbf{m}_e and a magnetic dipole moment \mathbf{m}_m positioned at the center ($x = 0, y = r = b/4, z = 0$). This setup is used to investigate the specific field regions in which coupling occurs.

The investigation compares a large TEM cell ($a = 40$ mm, $b = 24$ mm) against a small TEM cell ($a = 10$ mm, $b = 6$ mm). Both configurations are designed to maintain a characteristic impedance of $Z_0 \approx 50\Omega$. Electric and magnetic dipole moments with the frequency-dependent magnitudes shown in Figure 5.4b were placed in both cells.

The resulting output power, normalized to unity for comparison, is presented in Figure 5.4a. The close agreement between the power curves of the small and large cells indicates that the varying field regions have a negligible impact on the output power shape. The invariance of the normalized output power with respect to geometric scaling suggests that the dominant coupling mechanism is governed by the source dipole moments rather than by field-region transitions. The influence of frequency-dependent field-region transitions on the coupling behavior is therefore not considered further, and the following investigations focus exclusively on near-field coupling.

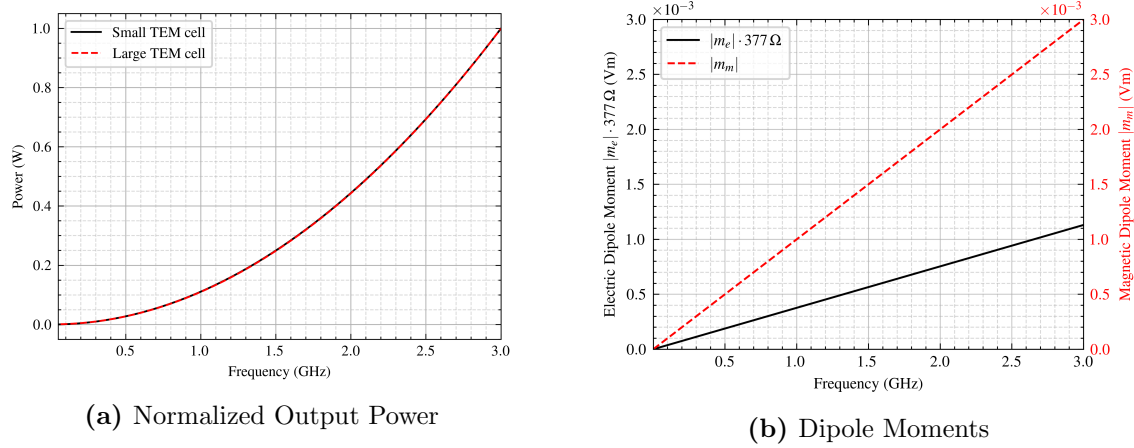


Figure 5.4 Comparison of coupling behavior: (a) The normalized output power produced by dipole moments in the large versus the small TEM cell, and (b) the dipole moments used as the source. The congruence of the power curves demonstrates that the coupling is independent of the cell dimensions.

5.2 Monopole Antenna

5.2.1 Setup

The monopole antenna is the simplest antenna capable of generating an electric dipole moment, and is therefore analyzed first to isolate this radiation mechanism. As shown in Figure 5.5b, it is installed inside the TEM cell and connected to a feed point on the top wall. The current flowing through the antenna is aligned with the electric field of the TEM mode, thereby producing an electric dipole moment according to (3.48a) and (3.48b), which are further investigated in Section 5.2.2.

The antenna has a physical length of 5 mm, making it electrically short across the entire frequency range of interest (up to 6 GHz). Below 1.25 GHz, the antenna is well approximated as an infinitesimal electric dipole, as discussed in Section 2.1.1. At higher frequencies, up to 6 GHz, the finite current distribution along the wire becomes non-negligible, and the antenna is instead treated as a small electric dipole, as described in Section 2.1.2.

Numerically, the near-field distribution exhibits strong displacement currents near the feed point and at the antenna tip. To accurately resolve these localized field concentrations, the mesh element size is reduced in both regions.

Because the electric dipole moment dominates the radiation mechanism, power transfer to the output ports occurs exclusively through displacement current coupling to the septum, as demonstrated in Section 3.5.3. The induced septum current is analyzed in Section 5.2.2 for two cases, including the propagation of the TEM mode alone, and exclusive propagation of the TE₀₁ mode.

As an open-circuit structure, the monopole antenna exhibits capacitive behavior. Its effect on the frequency dependence of the feed voltage, current, and input impedance is discussed in Section 5.2.4. The output power produced by the antenna is compared against that of

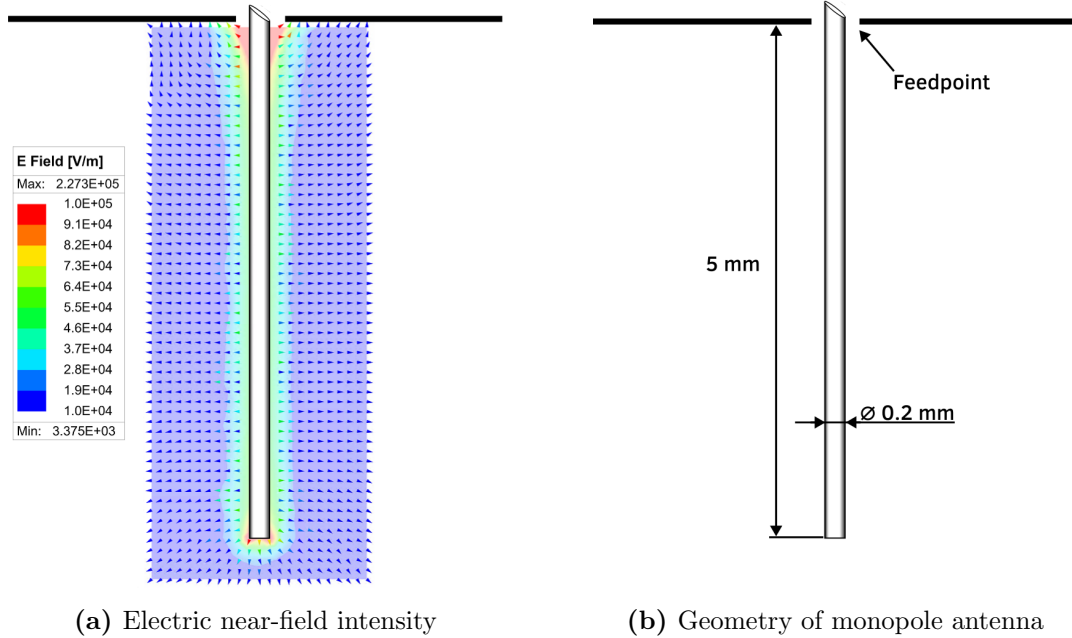


Figure 5.5 The geometrical aspects of the cylindrical monopole antenna, as implemented in the simulation model, with the respective electric near-field plot.

the equivalent dipole moments in ?? to validate the simulation models.

Lastly, the theoretical framework and numerical results established in this thesis are combined in Section 5.2.6 to construct an equivalent circuit model. The circuit model provides an analytical description and deeper understanding of the driving coupling mechanisms between the TEM cell and the monopole antenna.

5.2.2 Equivalent dipole moments

The corresponding equivalent electric and magnetic dipole moments, \mathbf{m}_e and \mathbf{m}_m , are analytically derived using Equations (3.46a) to (3.46b). The resulting \mathbf{m}_e shown in Figure 5.6 increases approximately linearly over frequency, while the magnetic dipole moment is negligible over the whole frequency range.

Furthermore, the phase difference between the power at the two output ports is zero across the entire frequency range. This observation is consistent with the assumption that a pure electric dipole moment introduces no phase shift between the output port powers, as discussed in subsubsection 3.5.2.

5.2.3 Current distribution on septum

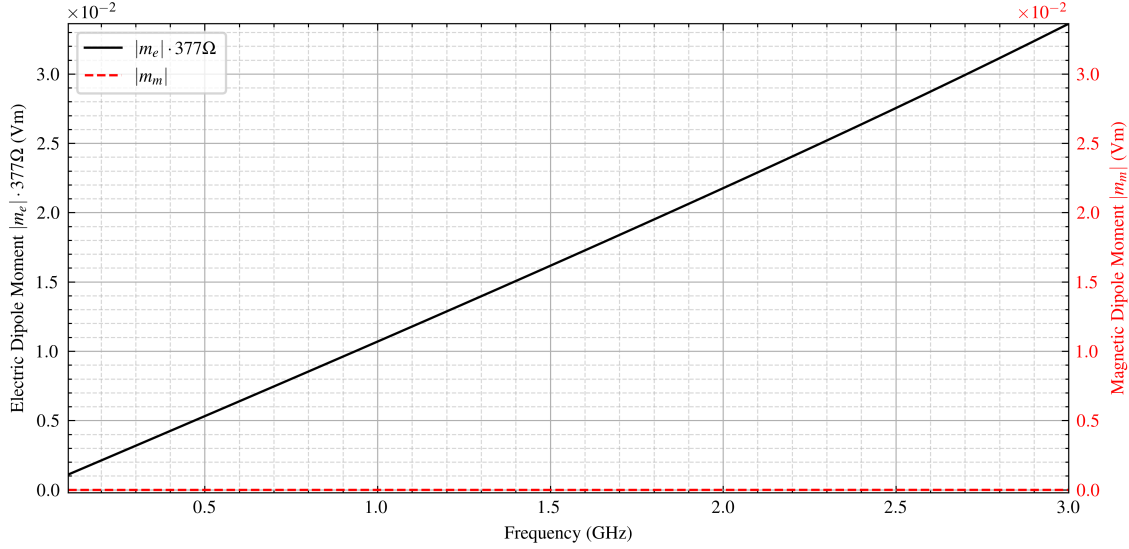


Figure 5.6 The equivalent electric and magnetic dipole moments analytically calculated with Equations (3.46a) to (3.46b). To enable direct comparison with the magnetic dipole moment, the electric dipole moment is weighted with the free space impedance Z_0 , as discussed in subsubsection 5.1.3.

Figure 5.7a shows the surface current density on the septum induced by the monopole antenna at 3 GHz. The current reaches both output ports in phase, confirming the absence of a phase shift between the output port powers.

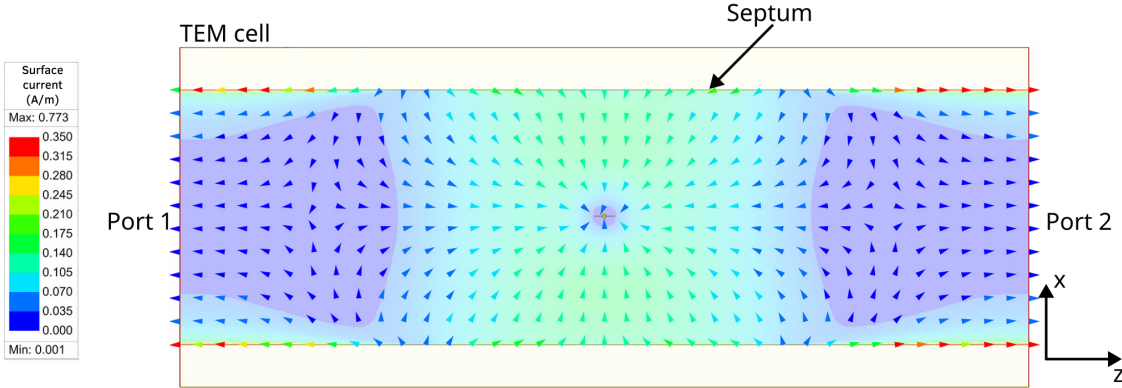
Figure 5.7b shows the current density of the septum at 3.3 GHz, with the TEM-mode compensated at the output ports. Due to the magnetic fields propagating in the z -direction, the current on the septum forms a pattern of swirls. However, at a frequency of 3 GHz, this pattern is not as pronounced, as the current in the swirls negligible, as shown in Figure 5.7a. Furthermore, the phase shift of the induced power between the output ports is π . This results from the magnetic field intensities of the TE_{01} -mode being in-phase at the output ports, opposed to the magnetic field intensities of the TEM-mode.

5.2.4 Feed voltage, current and impedance

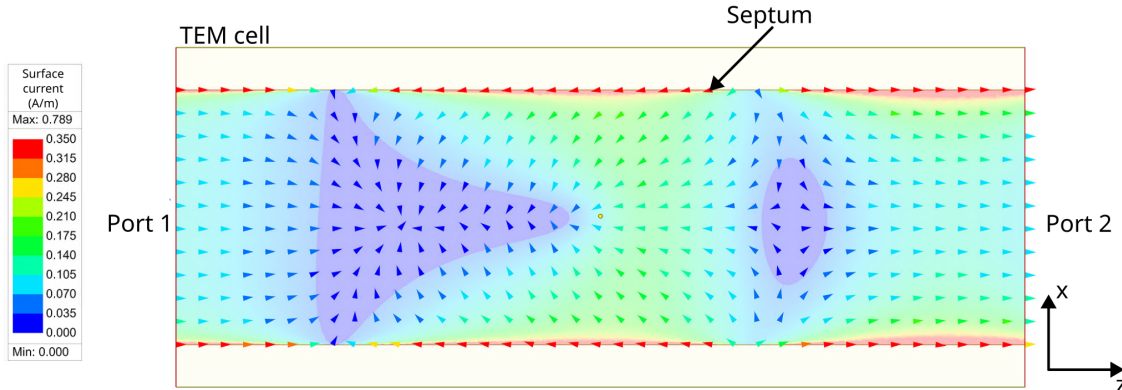
The feedpoint voltage V of the antenna, shown in Figure 5.8a, remains largely constant over the investigated frequency range. Consequently, the voltage induced between the antenna and the septum is negligible. This observation is consistent with the absence of a magnetic dipole moment \mathbf{m}_m , which is directly related to the induced voltage according to Equation 3.50.

The feedpoint current I , shown in Figure 5.8a, increases linearly. The entire current contributes to displacement currents due to the absence of a return path. According to Equation 3.56, \mathbf{m}_e is proportional to the displacement current to the septum. The linear increase of \mathbf{m}_e and I are therefore related.

At low frequencies, the antenna impedance in Figure 5.8b shows a high magnitude, which



(a) Current surface density at 3 GHz, where mostly the TEM mode propagates.



(b) Current surface density of only the TE₀₁-mode at 3.3 GHz with the TEM mode compensated.

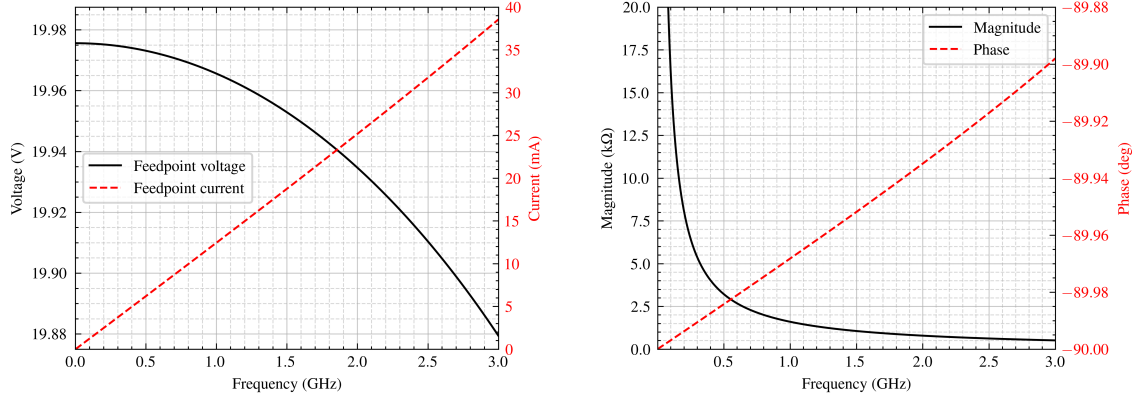
Figure 5.7 Current surface densities at different frequencies, below and above the cut-off frequency of the TE₀₁-mode.

rapidly decreases as frequency increases. Over the whole frequency range, it exhibits highly capacitive behavior, which is consistent with Equation 2.11 and the discussion in subsubsection 2.1.1.

Applying Equation 3.56 to determine \mathbf{m}_e requires knowledge of the magnitude of the displacement current to the septum. Another possibility of determining \mathbf{m}_e is the integration of the current I along the monopole antenna, as given in Equations (3.48a) to (3.48b). At a frequency of 3 GHz, this approach yields

$$\mathbf{m}_e(f = 3 \text{ GHz}) = \int_{b/2-5 \text{ mm}}^{b/2} I(y, f = 3 \text{ GHz}) dy = 85.69 \mu\text{Am} \cdot \hat{\mathbf{a}}_z, \quad (5.7)$$

which corresponds to $\mathbf{m}_e \cdot Z_0 = 3.23 \cdot 10^{-2} \cdot \text{Vm} \hat{\mathbf{a}}_z$ when normalized by the free-space wave impedance Z_0 . This approximates \mathbf{m}_e in Figure 5.6 at 3 GHz reasonably well, therefore supporting Equations (3.48a) to (3.48b).



(a) Voltage and current at feedpoint over frequency

(b) Antenna impedance over frequency

Figure 5.8 Magnitude of the voltage and current applied at the feedpoint of the monopole antenna over frequency, derived through the S-parameters with Equations (5.4) to (5.5), with the respective magnitude and phase of the antenna impedance over frequency, derived through the S-parameters with Equation 5.6.

The distribution of the current along the monopole antenna shown in Figure 5.11 is numerically derived by integrating the magnetic field intensity in a closed loop around the wire using Ampère's law,

$$\oint_L \mathbf{H} \cdot d\mathbf{l}' = I. \quad (5.8)$$

The current distribution at 3 GHz (see Figure 5.9) approximates that of a small electric dipole, as described in subsubsection 2.1.2. It shows an approximately linear decrease towards zero.

The current distribution at 1 MHz, shown in Figure 5.10, also decreases linearly along the monopole antenna. It can be approximated with an infinitesimal electric dipole, as discussed in subsubsection 2.1.1.

A fine mesh resolution, as discussed in subsubsection 5.1.4, is important for accurate results delivered by Equation 5.8. Consequences of a rough mesh is non-linear behavior near the feedpoint at 0 mm in Figure 5.11, which becomes apparent due to significant displacement currents and numerical artifacts in this region. This causes the current to exhibit a steeper decline with non-physical oscillations.

5.2.5 Output power

The derived equivalent dipole moments \mathbf{m}_e , \mathbf{m}_m in the TEM cell produce the output power over frequency shown in Figure 5.12b, where they are compared with the output power produced by the monopole antenna. The equivalent dipole moment approximation of the monopole antenna loses precision when approaching the cut-off frequency of the first

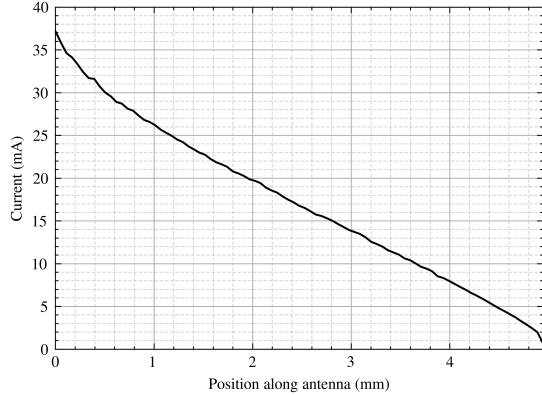


Figure 5.9 Current distribution at 3 GHz

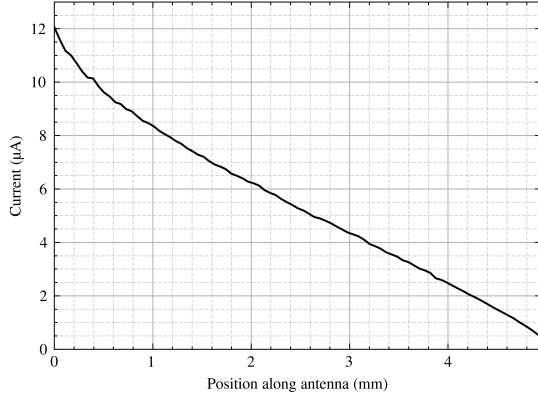
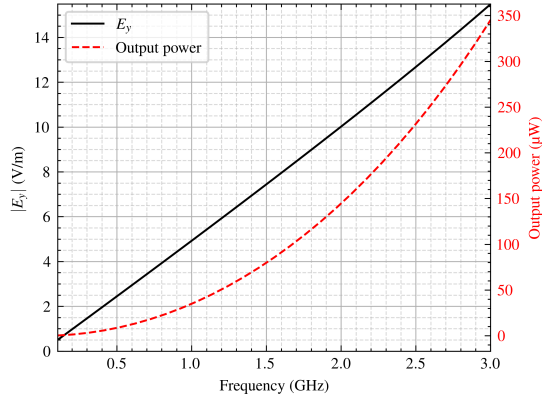


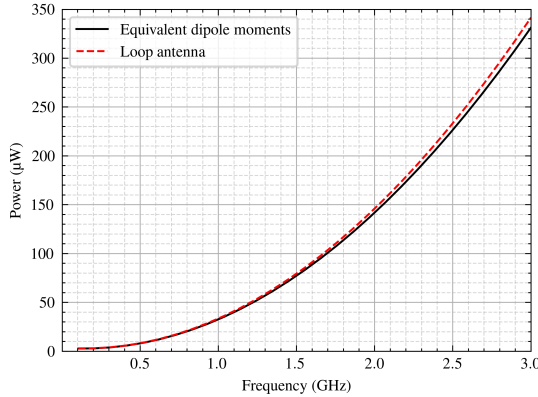
Figure 5.10 Current distribution at 1 MHz

Figure 5.11 The current distribution along the monopole antenna at 3 GHz and 1 MHz.

higher-order mode TE₀₁. Considering the coefficients $a_{\text{TE}01}$ and $b_{\text{TE}01}$ of the TE₀₁-moment increases accuracy, which is not done here.



(a) E_y and output power over frequency



(b) Comparison of output powers

Figure 5.12 Electric field in y-direction E_y at $x = 0, y = b/4, z = \pm l/2$, and power at one output port, derived with the S-parameters in Equation 5.2. The output power produced by the monopole antenna is compared to the output power produced by the equivalent dipole moments, to demonstrate validity of the model.

5.2.6 Equivalent circuit model

Equivalent circuit models of the antenna and the TEM cell are valuable tools for further analysis, as they enable analytical calculations and facilitate investigation and understanding of the observed coupling behavior. For the monopole antenna, a RLC serial circuit for a short electric dipole [13, pp. 59-60] is applied, as demonstrated in Figure 5.13, where R_A , L_A and C_A represent the impedance behavior of the antenna.

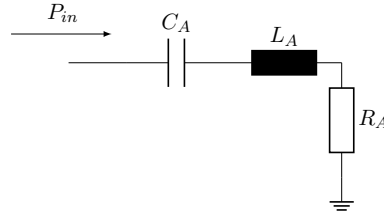


Figure 5.13 Equivalent circuit for a short electric dipole models the monopole antenna's behavior.

Although the resistance R_A generally represents conduction and radiation losses, it is omitted in this analysis. Conduction losses are non-existent due to the use of Perfect Electric Conductors (PEC). Additionally, the radiation resistance is disregarded because the radiation of the monopole on the free-space PEC plane in absence of the near-field coupling TEM cell is negligible. The antenna is therefore modeled as a lossless reactive network.

To determine L_A and C_A , the antenna model is placed on a PEC surface in an open space, as demonstrated in Figure 5.14. The inductance and capacitance are derived according to Equations (2.25a) to (2.25b), which leads to

$$L_A = 2 \frac{W_m}{I_{in}^2}, \quad (5.9a)$$

$$C_A = 2 \frac{W_c}{V_{CA}^2} = \frac{I_{in}^2}{2\omega^2 W_c}, \quad (5.9b)$$

where $V_{CA} = I_{in}/(j\omega C_A)$ denotes the current through the capacitor C_A . The resulting capacitance equals $C_A = 98.36 \text{ fF}$ the inductance amounts to $L_A = 1.14 \text{ nH}$.

The antenna equivalent circuit is extended in Figure 5.15 to incorporate the TEM cell's electrical characteristics. This cell is represented by a total inductance $L_T = L_{T1} + L_{T2}$ and capacitance $C_T = C_{T1} + C_{T2}$, as derived in Section 5.1.2. To maintain structural symmetry, the model utilizes split components where $L_{T1} = L_{T2}$ and $C_{T1} = C_{T2}$. It is important that this model is applied within the valid frequency range of the TEM cell equivalent circuit.

The equivalent circuits of the antenna and the TEM cell are coupled via C_k , which models the displacement current coupling, and the mutual inductances $M_{A,T1}$ and $M_{A,T2}$, which account for coupling through induced voltages. The mutual inductances are given by

$$\mathbf{V} = j\omega \begin{bmatrix} L_A & M_{A,T1} & M_{A,T2} \\ M_{T1,A} & L_{T1} & 0 \\ M_{T2,A} & 0 & L_{T2} \end{bmatrix} \mathbf{I}. \quad (5.10)$$

The near-field coupling between the antenna and the TEM cell is represented by the reactances C_k , $M_{A,T1}$, and $M_{A,T2}$, which renders the inclusion of a radiation resistance

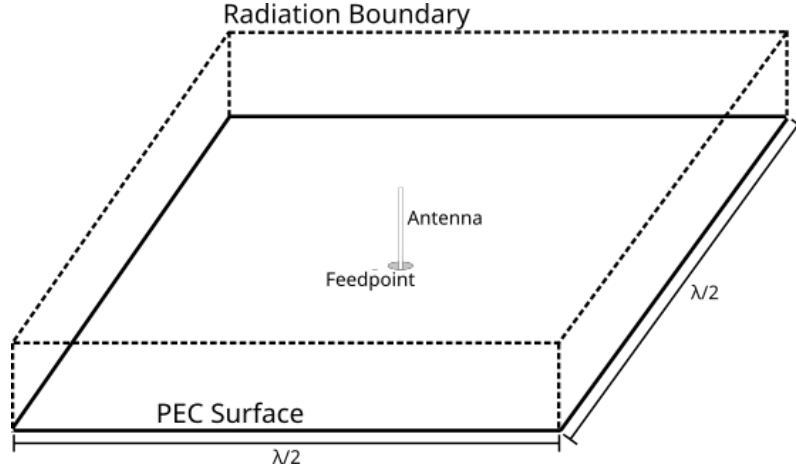


Figure 5.14 Model of the monopole antenna connected to a feedpoint mounted on a PEC surface with a side length of $\lambda/2$, where λ corresponds to the free-space wavelength of the solution frequency. This configuration enables the investigation of the monopole antenna reactance without influence of the TEM cell.

R_A again unnecessary. The magnetic dipole moment \mathbf{m}_m is derived from the induced voltages across L_{T1} and L_{T2} in accordance with Equation 3.50. Similarly, the electric dipole moment \mathbf{m}_e is determined from the displacement current flowing through C_k , as defined in Equation 3.56.

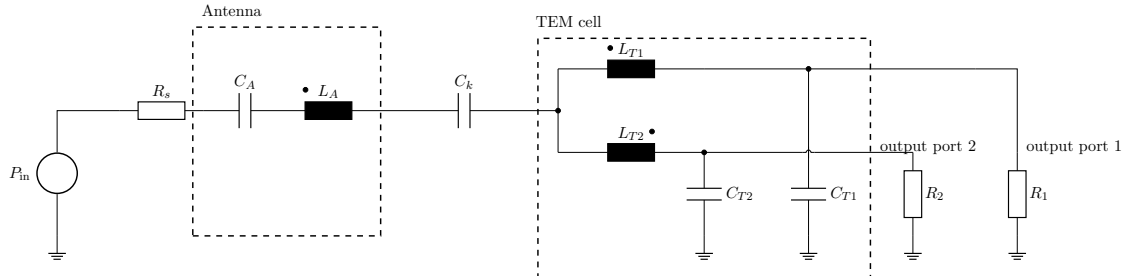


Figure 5.15 Circuit representing the TEM cell and the monopole antenna, with the additional components C_k and $M_{A,T1}$, $M_{A,T2}$ modeling their near-field coupling behavior.

The resulting \mathbf{m}_e and \mathbf{m}_m of the monopole antenna are depicted in Figure 5.16, which qualitatively agree with the dipole moments derived by the simulator over the investigated frequency range.

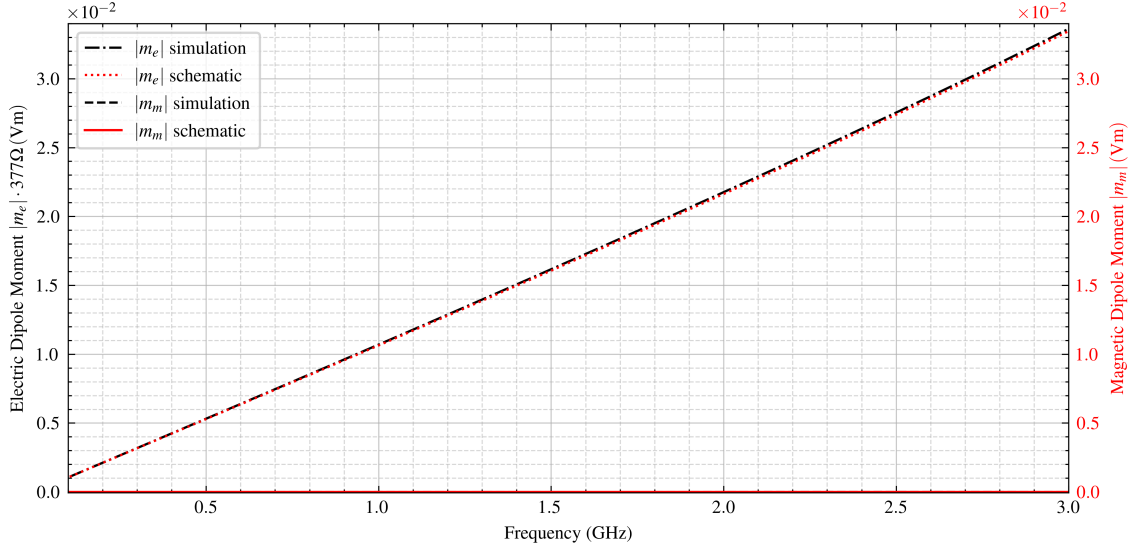


Figure 5.16 Equivalent dipole moments derived by the equivalent circuit depicted in Figure 5.2, compared to the derived dipole moments of the monopole antenna, shown in Figure 5.6. The electric dipole moment \mathbf{m}_e is weighted with η_0 for comparison purposes.

5.3 Loop antenna

5.3.1 Setup

A loop antenna is the most basic form of an antenna generating a mangetic dipole moment.

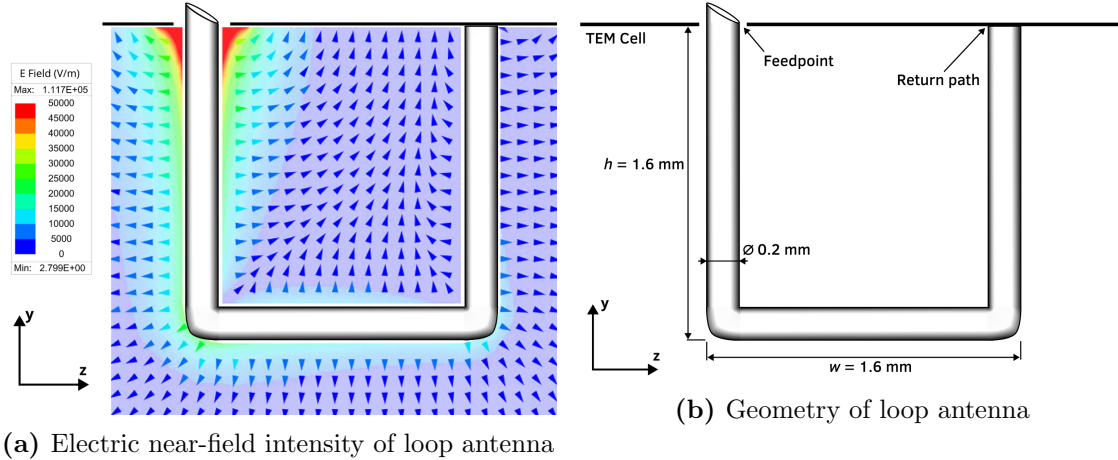
A square loop antenna is placed in the center of the TEM cell. It consists of four wires with a length of 1.6 mm each, and it is electrically short for frequencies up to 4.69 GHz. The square geometry is preferable to a round version in the numerical simulations, as it allows for more accurate meshes and enables a clearer investigation of the resulting dipole moments.

The normal vector of the loop surface points in x-direction, leading to a maximum coupling with the magnetic field of the TEM-mode. In contrast to the monopole antenna discussed in Section 5.2, a return path for the current exists, which generates a magnetic dipole moment.

5.3.2 Equivalent dipole moments

The equivalent dipole moments of the loop antenna are plotted in Figure 5.18a. The magnetic dipole moment \mathbf{m}_m dominates over the electric dipole moment \mathbf{m}_e . Opposed to the case of a monopole antenna, \mathbf{m}_e and \mathbf{m}_m demonstrate non-linear behavior over frequency, which is investigated further in Section 5.3.3.

Furthermore, the phases of the powers at the output ports, shown in Figure 5.18b, differ from one another. The phase shift in the low-frequency range approaches π , but gradually decreases with increasing frequency. This agrees with the analysis presented in Section 3.5.2, which predicts a phase shift of π when only \mathbf{m}_m is present, and a reduced



(a) Electric near-field intensity of loop antenna

(b) Geometry of loop antenna

Figure 5.17 The geometry of the loop antenna assimilates a square with round edges. The height and width of the antenna equal $h = w = 1.6$ mm. The return path leads back to the PEC surface of the TEM cell. The electric near-field shows large a displacement current and voltage drop near the feed-point. It has been derived with a refined mesh on the antenna surface and near the feedpoint, according to the discussion in Section 5.1.4.

phase shift as \mathbf{m}_e increases, as is the case here.

The power and E_y induced by the loop antenna at the output ports is shown in Figure 5.19a, and increases not as steeply as the output power of the monopole antenna exhibited in Figure 5.12a. This directly correlates with the decrease of \mathbf{m}_m with increasing frequency.

Figure 5.19b demonstrates the output power generated by the equivalent dipole moments \mathbf{m}_m , \mathbf{m}_e and the loop antenna. Their similarity support the validity of the model used.

5.3.3 Electrical characteristics

Calculating the electric and magnetic energy in the radiation boundary, as discussed in Section 2.3.2.

The current I in the loop antenna changes along the antenna wire as shown in Figure 5.21a, indicating displacement current coupling to the septum and back to the feedpoint. The difference between the feedpoint and return path current increases over frequency, translating to rising displacement currents. Furthermore, the decrease in feed current over rising frequency, shown in Figure 5.21a, also hints to the presence of increasing displacement currents. Consequently, \mathbf{m}_e gains a significant magnitude according to Equation 3.56, increasing the electric coupling of the antenna to the TEM cell.

The feedpoint current is derived with Equation (5.8), through integration of \mathbf{H} in a closed loop of radius 0.11 mm, measured 0.17 mm above the feedpoint. The return path current is processed with the same loop integration at the same height above the PEC surface. The results vary with height above the PEC surface due to the displacement currents in the near-field.

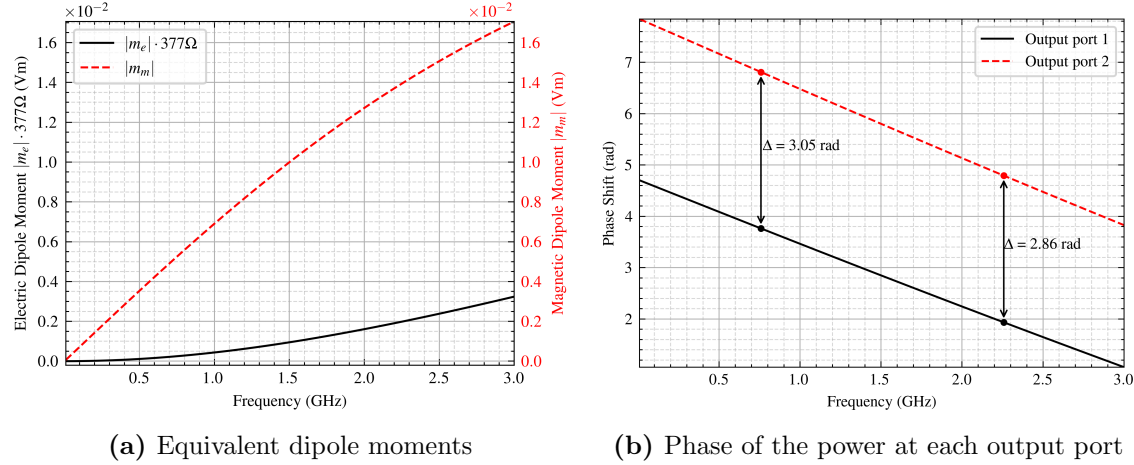


Figure 5.18 The equivalent dipole moments of the loop antenna are derived analytically with Equations (3.46a) to (3.46b), where the electric dipole moment \mathbf{m}_e is weighted with Z_0 to enable comparison with \mathbf{m}_m . The phases of the powers at output ports 1 and 2 are derived from the S-parameters, as discussed in Section 5.1.6. The analysis specifically focuses on the phase shift between the two ports, which provides information about the presence of \mathbf{m}_m and \mathbf{m}_e , as investigated in Section 3.5.2.

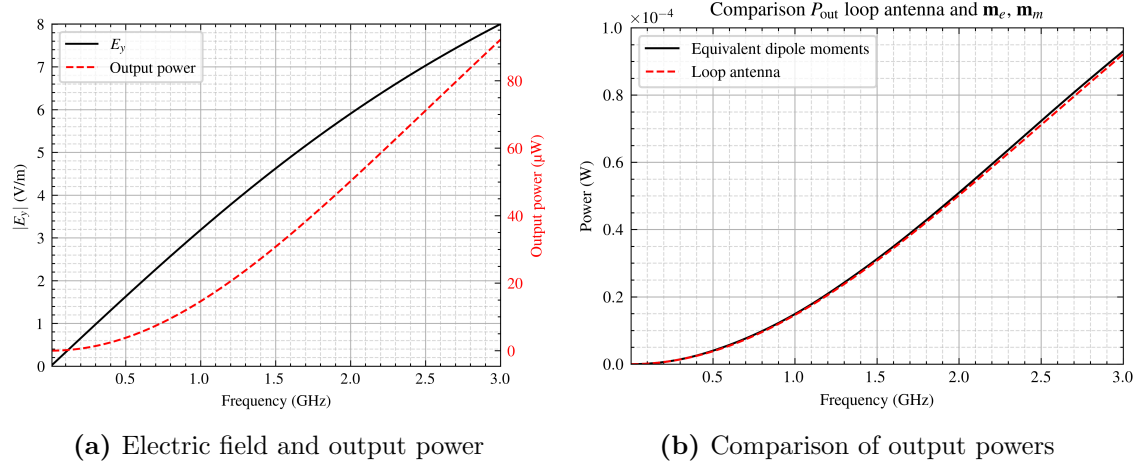


Figure 5.19 Electric field in y-direction E_y at $x = 0, y = b/4, z = \pm l/2$, and the closely related power at one of the output ports, derived with the S-parameters in Equation 5.2. The output power produced by the loop antenna is compared with that generated by the equivalent dipole moments.

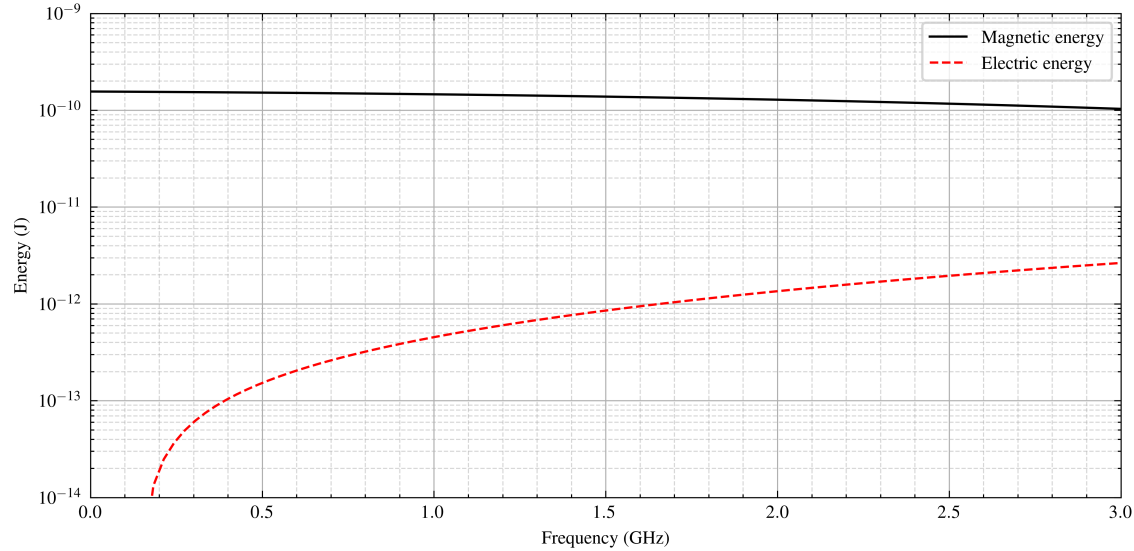


Figure 5.20 Electric and magnetic energy produced by the loop antenna in the TEM cell, derived with Equation 2.24 in the TEM cell volume.

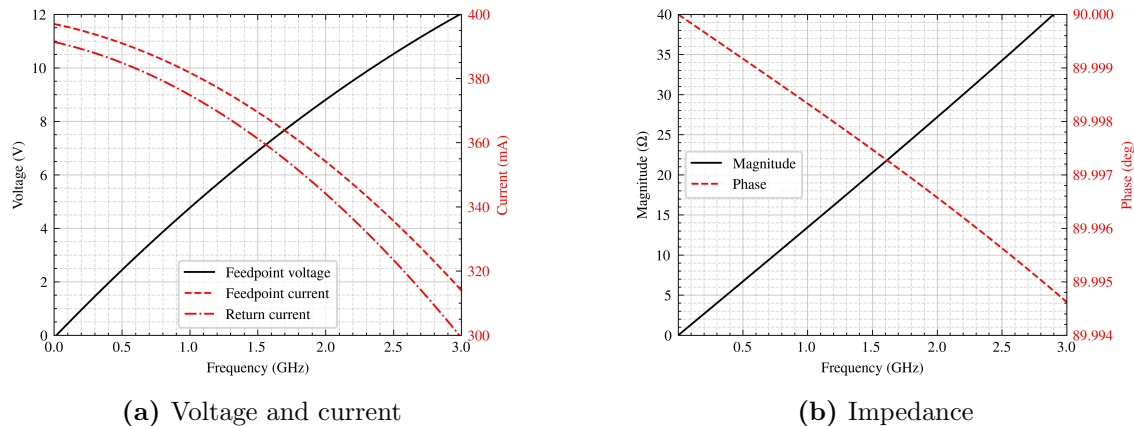


Figure 5.21 This figure demonstrates the voltage, current and impedance characteristics of the loop antenna. The difference between the current near the feedpoint and that on the return path increases with frequency, indicating a growing occurrence of displacement currents. The current on those paths are determined through magnetic near-field intensity, using Equation 5.8. The voltage across the feedpoint is obtained using Equation 5.5. Magnitude and phase of the impedance of the loop antenna are determined with Equation 5.6.

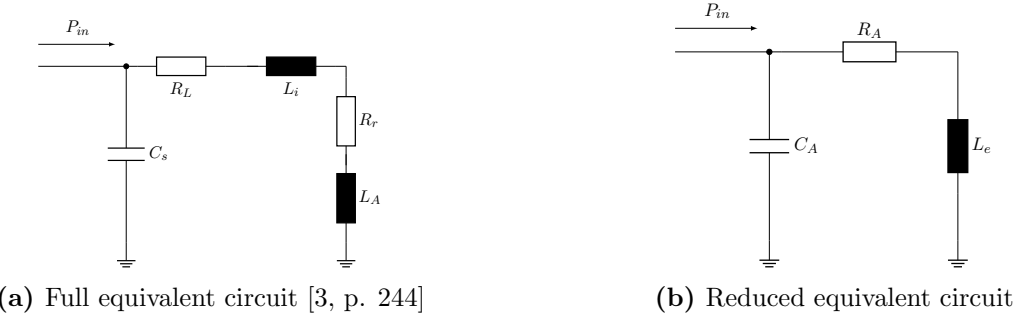


Figure 5.22 Equivalent circuits of the small loop antenna.

Figure 5.21a demonstrates the voltage at the feedpoint of the antenna, which significantly rises over the frequency, signaling increased induced voltage V_n . According to Equation 3.50, this directly correlates with \mathbf{m}_m , which furthermore becomes apparent when comparing their behavior shown in Figures 5.18a to 5.21a. The increase in voltage also correlates with the displacement current. It raises the potential on the loop antenna, therefore increasing the charge distributions and displacement currents.

The increases in voltage and decrease in current agrees with the impedance, depicted in Figure 5.21b. The loop antenna shows strongly inductive behavior.

5.3.4 Equivalent circuit model

Following the same approach established in Section 5.2.6, an equivalent circuit is derived for the small loop antenna. Figure 5.22a demonstrates the full equivalent circuit for the electrically small loop antenna in free space [3, p. 244], where

- C_s Stray capacitance of the loop antenna
- R_L Ohmic loss resistance of the antenna conductor
- R_r Radiation resistance of the loop antenna
- L_i Internal inductance of the loop antenna
- L_e External inductance of the loop antenna

As discussed in Section 5.1.1, the antenna is modeled as a perfect electric conductor, therefore R_L and L_e are neglected. Instead, the simplified equivalent circuit in Figure 5.22b is applied, where R_A , L_A and C_A represent the impedance behavior of the antenna.

To determine R_A , L_A and C_A , the antenna model is placed on a PEC surface in an open space, as demonstrated in Figure 5.23. The inductance and capacitance are derived according to Equations (2.25a) to (2.25b), which leads to

$$L_A = 2 \frac{W_m}{I_{LA}^2} = \frac{V_{in}^2}{2\omega^2 W_m}, \quad (5.11a)$$

$$C_A = 2 \frac{W_c}{V_{in}^2}, \quad (5.11b)$$

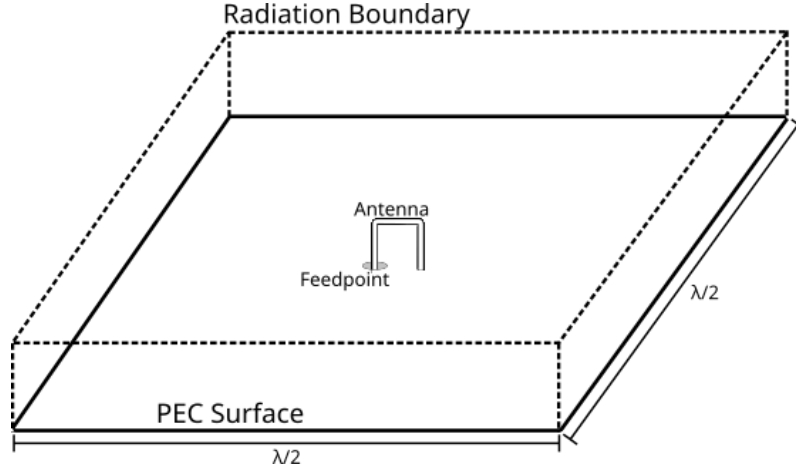


Figure 5.23 Model of the loop antenna connected to a feedpoint mounted on a PEC surface with a side length of $\lambda/2$, where λ corresponds to the free-space wavelength of the solution frequency. This configuration enables the investigation of the loop antenna reactance without influence of the TEM cell.

where $I_{LA} = V_{in}/(j\omega L_A)$ denotes the current through the inductor L_A . The resulting capacitance and inductance equal $C_A = 38.2 \text{ fF}$ and $L_A = 2.14 \text{ nH}$.

The antenna equivalent circuit is extended with the TEM cell coupling model introduced in Section 5.1.2, as shown in Figure 5.24. The coupling components C_k , $M_{A,T1}$ and $M_{A,T2}$ are defined analogously to Section 5.2.6.

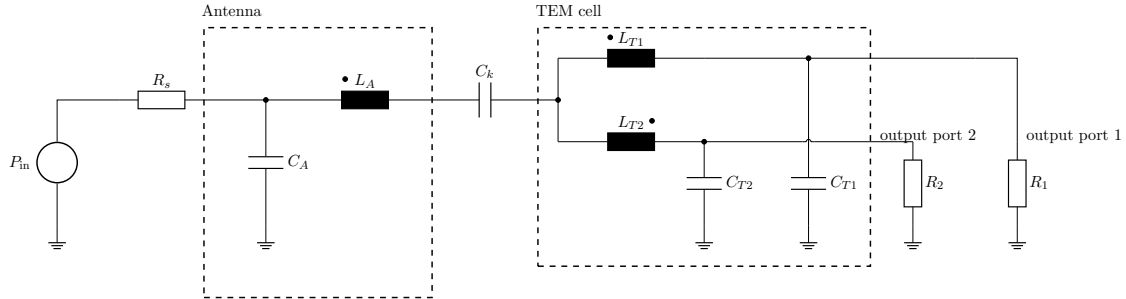


Figure 5.24 Circuit representing the TEM cell and the loop antenna, with the additional components C_k and $M_{A,T1}$, $M_{A,T2}$ modeling their near-field coupling behavior.

The resulting \mathbf{m}_e and \mathbf{m}_m are depicted in Figure 5.25, which are similar to the dipole moments derived by the simulator in the higher end of the frequency range. However, accuracy recedes in the low-frequency range.

5.3.5 Current distribution on septum and higher order modes

The radiating loop antenna induces surface currents on the septum of the TEM cell, as shown in Figure 5.26. At a frequency of 3 GHz, the currents reaching the output ports are out of phase, as illustrated in Figure 5.26a. This observation is consistent with the analysis

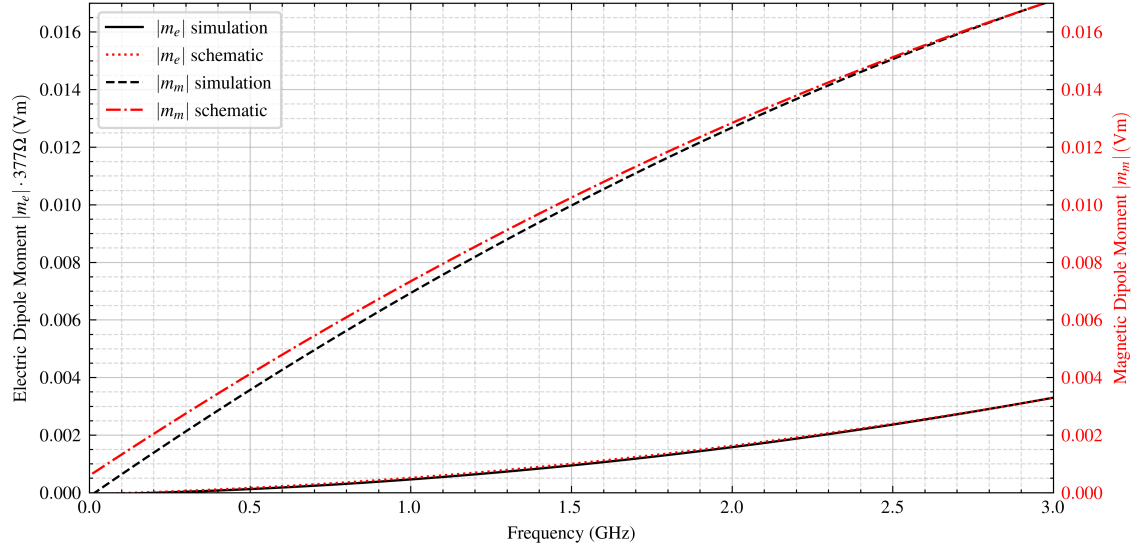
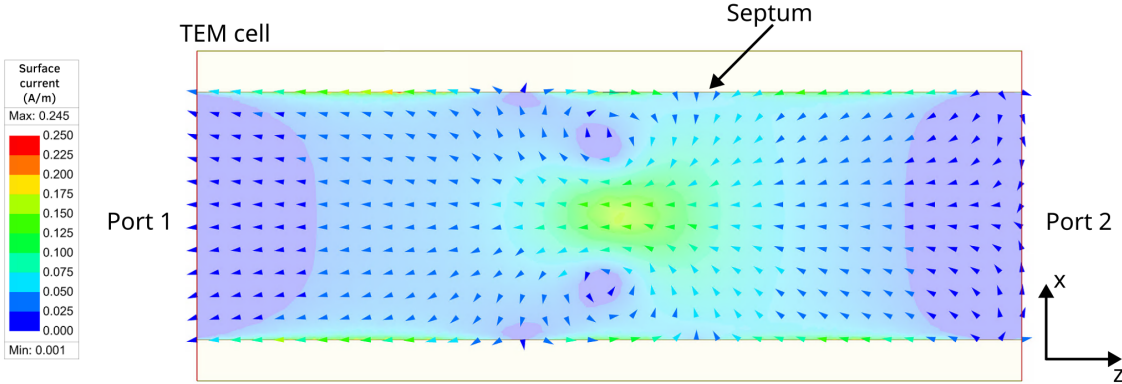


Figure 5.25 Equivalent dipole moments derived by the equivalent circuit depicted in Figure 5.24, compared to the dipole moments of the loop antenna, shown in Figure 5.18a. The electric dipole moment \mathbf{m}_e is weighted with η_0 for comparison purposes.

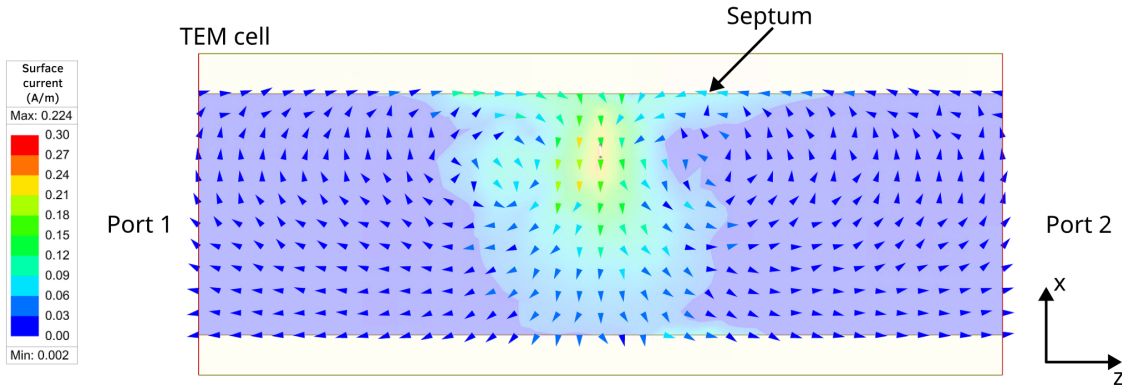
in Section 3.5.2, which predicts a phase shift of $\pm\pi$ between the output port powers in the presence of a magnetic dipole moment.

When the antenna is rotated by $\pm\pi/4$ and offset by $x = 7$ mm, power transmission at 3 GHz is insignificant. According to Equations (3.49a) to (3.49b) and Equation 3.50, efficient coupling requires the magnetic field intensity of the propagating TEM mode $\mathbf{h}_{\text{TEM}}^{\pm}$ to be aligned with the vector normal to the antenna surface. The current distribution Figure 5.26b demonstrates no excited waves in this configuration. Instead, the power produced by the surface current remains reactive, forming closed circulation patterns around the induced magnetic fields.

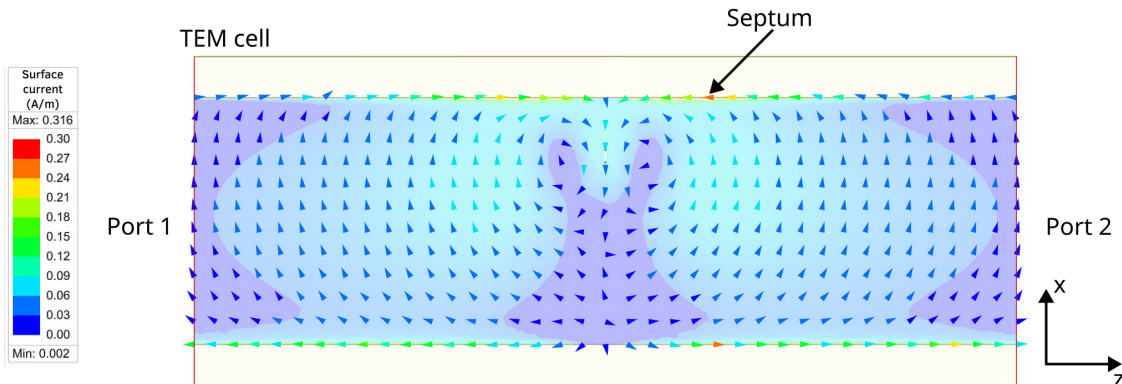
At a frequency of 3.3 GHz, the TE₀₁ mode propagates in the TEM cell. In this case, $\mathbf{h}_{\text{TE}01}^{\pm}$ aligns with the normal vector of the offset and rotated loop antenna surface. As shown in Figure 5.26c, a significant proportion of the current now reaches the output ports, resulting in transmission of power. In contrast to the previous case, the output powers are in-phase, as discussed in Section 3.5.2. The output power transmitted by the TE₀₁ mode increases sharply with frequency, as demonstrated in Figure 5.27.



(a) The centrally located loop antenna without offset or rotation at a frequency of 3 GHz, where mainly the TEM mode propagates.



(b) Loop antenna with offset of $x = 7$ mm and a $\pi/4$ rotation angle at 100 MHz, where only the TEM mode propagates. The currents passing to the output ports are negligible.



(c) Loop antenna with offset of $x = 7$ mm and a $\pi/4$ rotation angle at 3.3 GHz, where the TEM and TE₀₁ modes both propagate. The currents passing to the output ports produce significant power, as shown in Figure 5.27.

Figure 5.26 Surface current density on the septum induced by the loop antenna for different frequencies and positions of the antenna.

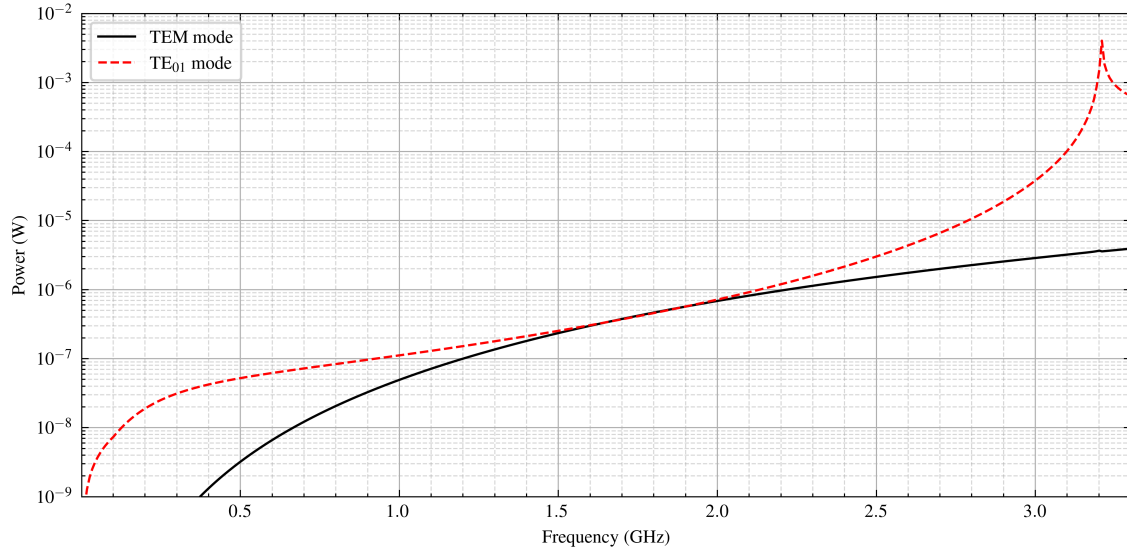


Figure 5.27 Output power transmitted by the antenna to the output port through the TEM and TE₀₁ modes, separately over frequency, determined through the S-parameters with Equation 5.2. At a frequency of $f = 3.21$ GHz a resonance in the TEM cell occurs, leading to the visible peak in the output power produced by the TE₀₁ mode.

5.3.6 Influence of antenna's geometry

The influence of the antenna's geometry on coupling behavior is investigated. The height h and width w of the loop antenna presented in Figure 5.17b is varied, and their dipole moments and power consumption compared in Figures 5.28a to 5.28b.

The loop area is identical in both configurations presented. Consequently, the behavior of the magnetic dipole moments \mathbf{m}_m are the same in both cases, which agrees with Equations (3.49a) to (3.49b). Nonlinear frequency dependence of \mathbf{m}_m persists in both configurations, due to the nearly constant capacitance of the antenna.

The electric dipole moment \mathbf{m}_e is strongly dependent on the antenna height h . The antenna with a height of $h = 2.16$ mm generates an electric dipole moment \mathbf{m}_e , more than twice as large as that of the antenna with $h = 1.2$ mm, as depicted in Figure 5.28a. This result supports validity of the used models and is consistent with Equation 3.56, which relates the displacement current between the antenna and septum to the electric dipole moment \mathbf{m}_e . Lastly, the output power produced by the antenna generating the larger electric dipole moment \mathbf{m}_e is also greater, as shown in Figure 5.28b.

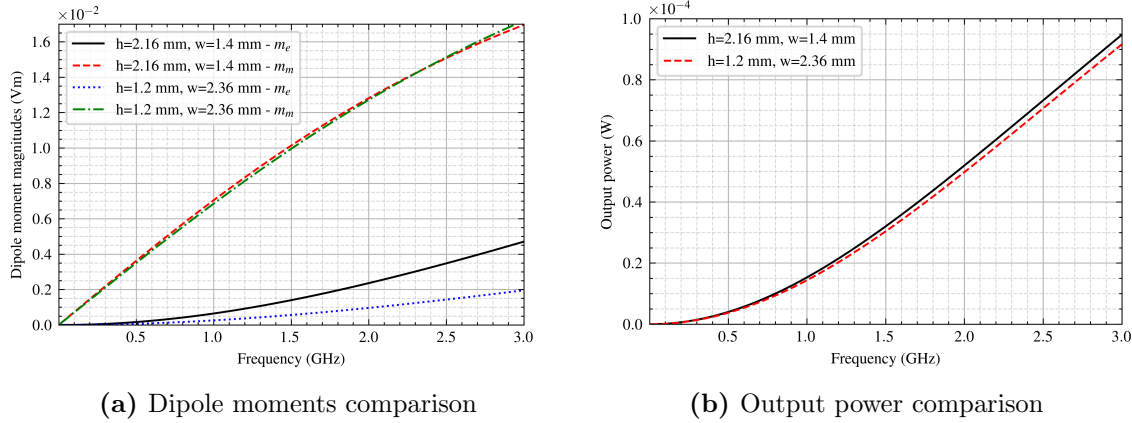


Figure 5.28 Dipole moments and output power comparisons of two different loop antenna configurations presented, one with $h = 2.16 \text{ mm}$, $w = 1.4 \text{ mm}$ and the other with $h = 1.2 \text{ mm}$, $w = 2.36 \text{ mm}$. The electric dipole moment \mathbf{m}_e is weighted with Z_0 for comparison purposes.

5.4 Loop antenna with gap

5.4.1 Setup and geometrical analysis

The geometry of the loop antenna with a gap is similar to that of the loop antenna discussed in subsection 5.3. It is electrically short for frequencies up to 4.69 GHz. A gap with a height of 10 μm is introduced in the return path, as shown in Figure 5.29b. The gap is intentionally kept small to emphasize specific coupling mechanics and to demonstrate the consistency of antenna analysis with the framework developed in this thesis, although such a small gap would be hard to implement in a physical antenna. Furthermore, manual mesh refinement is necessary around the gap region, as well as the feedpoint and the curved surfaces, as discussed in subsubsection 5.1.4.

The magnetic coupling is determined with Equations (3.49a) to (3.49b), just as is the case for the normal loop antenna. However, considering the gap region leads to

$$-\oint_C \boldsymbol{\tau} I(l) \cdot \mathbf{e}_n^\pm dl = - \int_{\text{wire}} \boldsymbol{\tau} I_{\text{wire}}(l) \cdot \mathbf{e}_n^\pm dl - \int_{\text{gap}} \boldsymbol{\tau} I_{\text{gap}}(l) \cdot \mathbf{e}_n^\pm dl. \quad (5.12)$$

The electric current across the gap is $I_{\text{gap}} = 0 \text{ A}$, while the current in the antenna wire I_{wire} is significantly reduced due to the interrupted current path. Consequently, the magnetic coupling between the loop antenna with a gap and the TEM cell is expected to be weaker than that of the loop antenna without a gap, but still more present than the monopole antenna discussed in subsection 5.2. Furthermore, reducing the gap height increases magnetic coupling and the magnitude of the magnetic dipole moment \mathbf{m}_m , attributable to the correlated increase of I_{wire} .

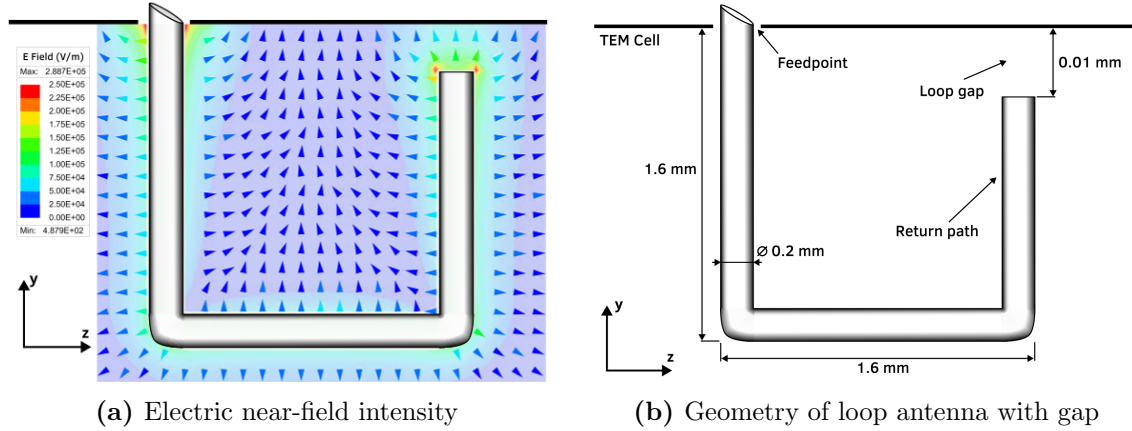


Figure 5.29 Geometry of the loop antenna with a gap in the return path inserted in the TEM cell. The gap height is exaggerated for demonstration purposes.

The conductors adjacent to the gap behave as capacitors plates, accumulating charges on both either side. According to Equations (3.55a) to (3.55b), these accumulated charges lead to electric coupling with the septum. A smaller gap height increases the amount of accumulated charges, and consequently leads to an increase in the electric dipole moment \mathbf{m}_e . Lastly, the absence of a conductive return path for the current leads to expect capacitive behavior of this electrically small antenna, similar to the monopole antenna analyzed in subsection 5.2.

5.4.2 Equivalent dipole moments

The equivalent dipole moments of the loop antenna with gap are shown in Figure 5.30a, where the electric dipole moment \mathbf{m}_e is larger than the magnetic dipole moment \mathbf{m}_m . The dipole moments behave non-linearly over the frequency.

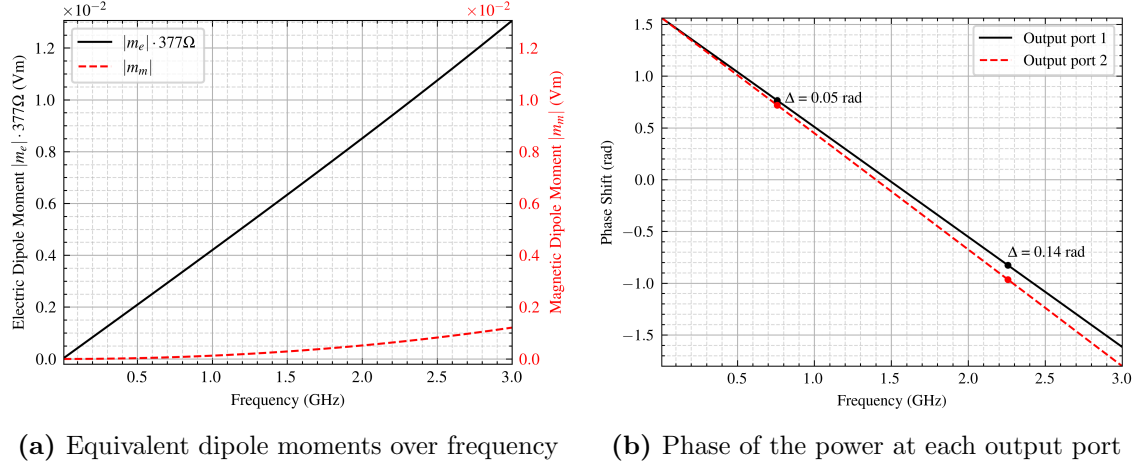
Figure 5.31a demonstrates the effect of the gap height on the dipole moment behavior. As discussed in subsubsection 5.4.1, the reduction of the gap height leads to an increase of both dipole moments, \mathbf{m}_e and \mathbf{m}_m . Their magnitudes correlate with the output power, as shown in Figure 5.31b.

An increase in gap height reduces the non-linearities in \mathbf{m}_e and \mathbf{m}_m . The voltage drop across the gap and the charge accumulation remains more stable over frequency.

5.4.3 Electrical characteristics

The impedance of the loop antenna with gap is capacitive, shown in Figure 5.32b. The inductance of this antenna is not negligible, opposed to the case of the monopole antenna in subsection 5.2. This causes a significant magnitude of \mathbf{m}_m in Figure 5.30a and a stronger decline in impedance magnitude of the loop antenna with gap, compared to the monopole antenna's impedance, demonstrated in Figure 5.8b.

The feedpoint voltage decreases more rapidly over frequency compared to that of the monopole antenna, see Figures 5.32a to 5.21a. This behavior is a direct result of increased



(a) Equivalent dipole moments over frequency (b) Phase of the power at each output port

Figure 5.30 The equivalent dipole moments of the loop antenna with a gap, where the electric dipole moment \mathbf{m}_e is weighted with Z_0 to enable comparison with \mathbf{m}_m . The phases of the powers at output ports 1 and 2 are derived from the S-parameters, as discussed in Section 5.1.6. The analysis specifically focuses on the phase shift between the two ports, which provides information about the presence of \mathbf{m}_m and \mathbf{m}_e , as investigated in Section 3.5.2.

induced voltage, which correlates with the pronounced magnetic dipole moment \mathbf{m}_m , according to Equation 3.50. Furthermore, the feed current increases more slowly, resulting in a slower growth of the electric dipole moment \mathbf{m}_e with frequency, according to Equation 3.56. The magnitude of \mathbf{m}_e is additionally smaller than that of the monopole in Figure 5.6.

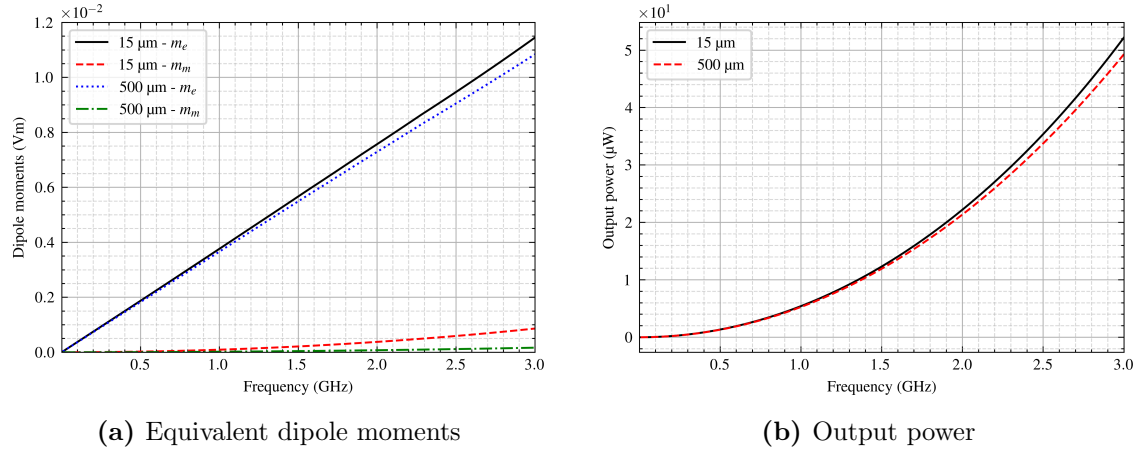


Figure 5.31 Comparison of dipole moments, where the electric dipole moment \mathbf{m}_e is weighted with η_0 to enable comparison with \mathbf{m}_m , and output power for different gap heights in the loop antenna.

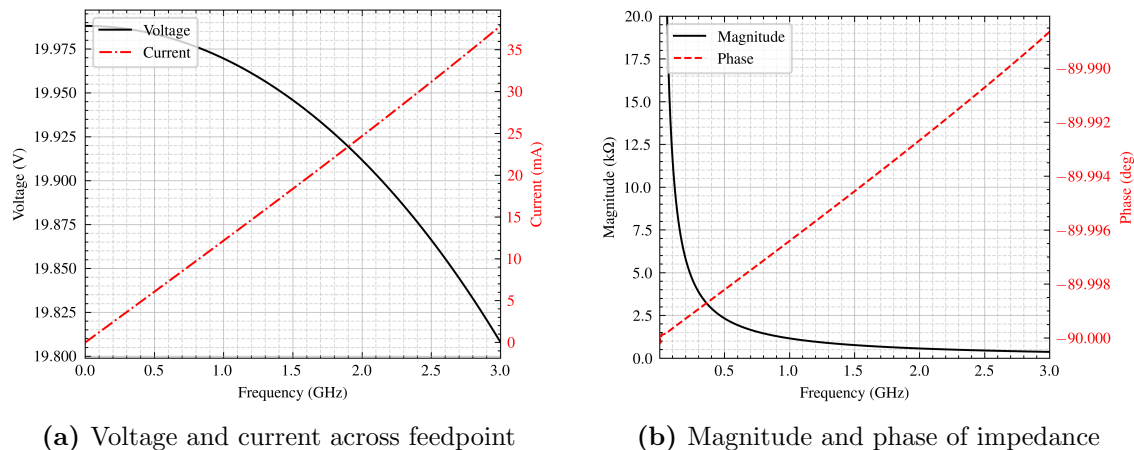


Figure 5.32 The voltage and current across the feedpoint, together with the related impedance of the loop antenna with gap.

5.5 Inverted-F and center-fed monopole antenna

5.5.1 Setup and geometrical analysis

The inverted-F antenna (IFA) and center-fed monopole antenna (CFM), shown in Figures 5.33a to 5.33b, are presented here together, because of their related geometry and similar electromagnetic behavior. Both have a maximum dimension of 5 mm, and are electrically small at frequencies up to 6 GHz. They exhibit an inductive nature, hence a similar behavior as the loop antenna in subsection 5.3 is expected. Both antennas consist of a loop of identical area to the loop antenna discussed in Section 5.3, to which a linear arm is connected. In the CFM, this arm is oriented toward the TEM cell septum, whereas in the IFA it is directed toward an output port.

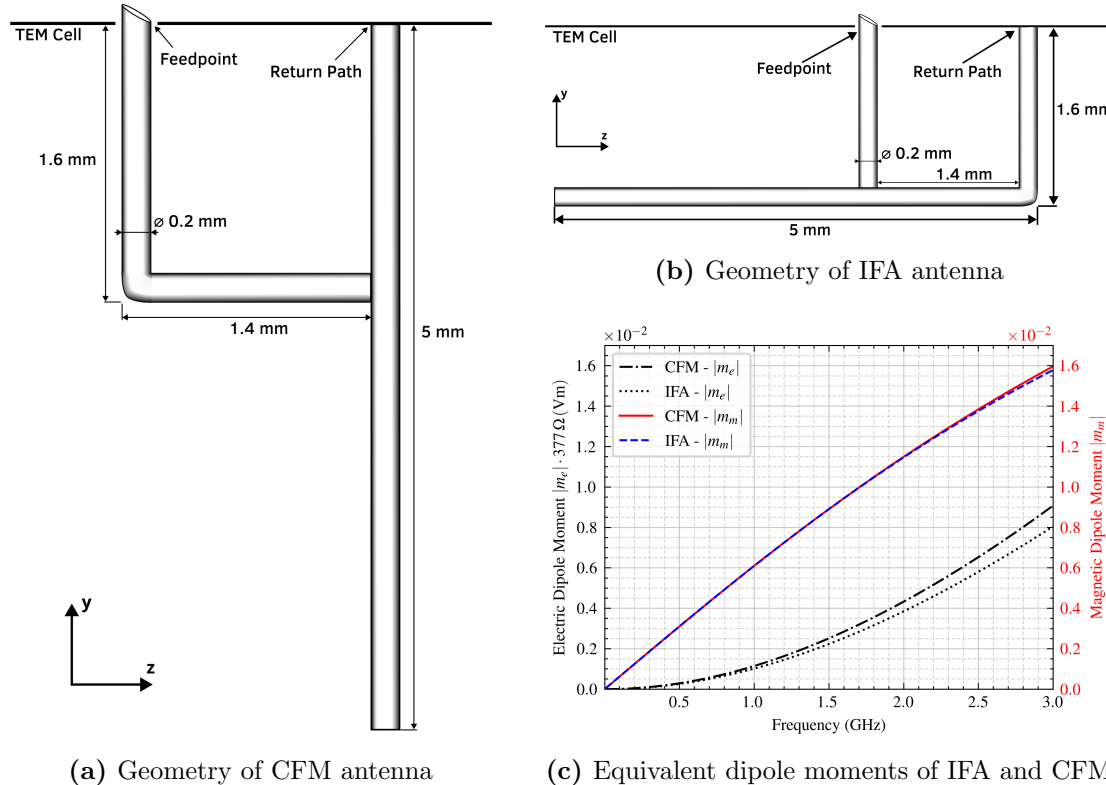


Figure 5.33 Geometries of IFA and CFM antenna, together with their equivalent dipole moments. the electric dipole moment \mathbf{m}_e is weighted with the free space impedance Z_0 to enable comparison with the magnetic dipole moment \mathbf{m}_m .

5.5.2 Equivalent dipole moments

The magnetic dipole moments \mathbf{m}_m of the CFM and IFA presented in Figure 5.33c are comparable to each other, but are smaller in magnitude than that of the loop antenna shown in Figure 5.18a. This reduction can be attributed to the linear arms of the CFM and IFA, which introduce additional capacitance. The increased capacitance enhances the displacement current while reducing the induced voltage. According to Equations (3.50)

to (3.56), this results in a decrease of magnetic dipole moment \mathbf{m}_m and an increase of the electric dipole moment \mathbf{m}_e .

Furthermore, for small loop and inductive antennas in general, ?? predicts that an increase in capacitance leads to a stronger non-linear frequency dependence of both \mathbf{m}_m and \mathbf{m}_e . This assumption is confirmed by comparing the dipole moments of the loop antenna with those of the CFM and IFA, shown in Figures 5.18a to 5.33c.

6 Application of Shielding Techniques in TEM Cells

6.1 ASTM ES7-83 method

A numerical model of a TEM cell is employed to determine the shielding effectiveness of barium titanate, ferrite, and silver, following the ASTM ES7-83 method described in Section 3.6.3. The electrical properties of these materials are listed in Table 6.1 and are chosen such that the individual contributions of high conductivity, lossy permeability, and lossy permittivity to the overall shielding performance can be investigated in isolation. Ferrite is additionally modeled with a magnetic loss tangent of $\tan \delta_m = 0.05$ and barium titanate with an electric loss tangent of $\tan \delta = 0.0095$.

The shielding material is modeled as a thin sheet of thickness $10\ \mu\text{m}$, positioned at the center of the TEM cell at $z = 0$. To reduce computational cost, the sheet is represented using impedance boundary conditions, which are valid and an accurate representation for this material thickness as discussed in Section 5.1.5. The ASTM ES7-83 method requires the definition of a reference power to evaluate the shielding efficiency according to (3.66), which is set to $P_{\text{ref}} = 1\ \text{W}$. The transferred power P_{load} between the TEM cell ports in the presence of the shielding material is then determined numerically, from which the shielding effectiveness as a function of frequency is computed for each material. The resulting shielding effectiveness are presented against frequency in Figure 6.1.

Material	Rel. permittivity ϵ_r	Rel. permeability μ_r	Conductivity σ
Ferrite	≈ 12	$\approx 1,000$	$0.01\ \text{S/m}$
Barium titanate	$\approx 2,000$	≈ 1	$3.64 \cdot 10^{-11}\ \text{S/m}$
Silver	≈ 1	≈ 1	$6.10 \cdot 10^7\ \text{S/m}$

Table 6.1 Electromagnetic properties of ferrite, barium titanate, and silver.

Silver, as a highly conductive material, exhibits a large reflection loss R_{dB} owing to the significant impedance mismatch between the material and the surrounding air. This mismatch decreases with increasing frequency, as the wave impedance of silver rises with frequency in accordance with (3.60). Simultaneously, the absorption coefficient A_{dB} grows with frequency, consistent with the reduction in skin depth at higher frequencies, as discussed in ???. At low frequencies, the multiple-reflection correction term B_{dB} is negative and partially offsets the reflection loss, as discussed in Section 3.6.1. As frequency increases, however, the sheet becomes electrically thicker, rendering B_{dB} negligible while the absorption term A_{dB} increases. Nonetheless, within the frequency range considered,

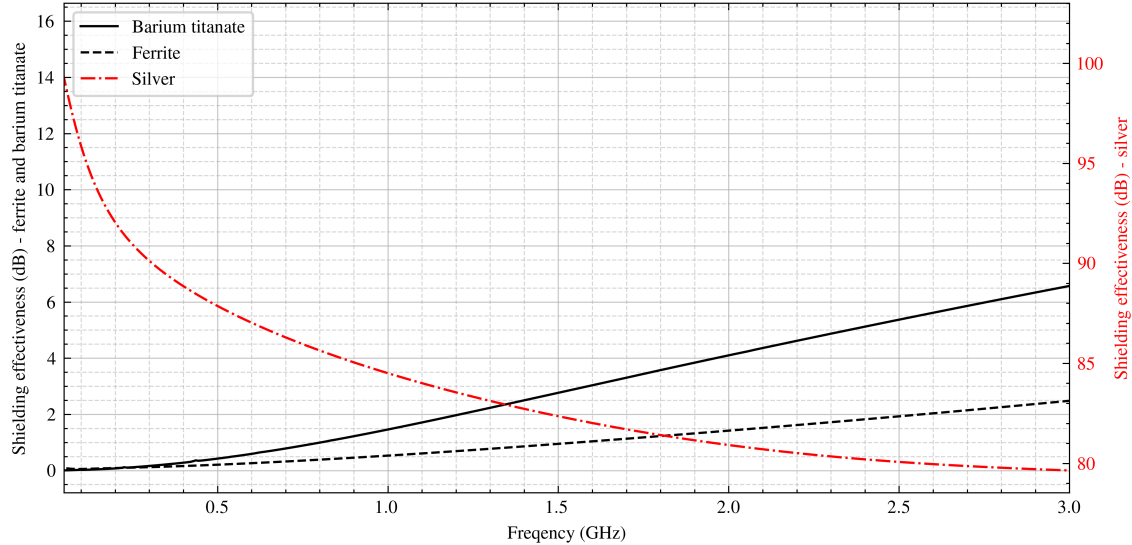


Figure 6.1 Shielding effectiveness of a thin sheet of ferrite, barium titanate, and silver as a function of frequency, determined using the ASTM ES7-83 method.

the decrease in reflection loss is more pronounced than the increase in absorption, resulting in an overall reduction in shielding effectiveness with frequency.

Ferrite exhibits moderate shielding effectiveness over the investigated frequency range. Its high relative permeability μ_r raises the material wave impedance in accordance with (3.60), increasing the impedance mismatch with air and thus the reflection loss R_{dB} . At low frequencies, the multiple-reflection correction term B_{dB} almost completely compensates the reflection loss. The absorption coefficient A_{dB} is limited by its low bulk conductivity σ and magnetic losses parameterized by $\tan \delta_m$, so that the shielding performance is primarily governed by reflection.

Barium titanate, with its very high relative permittivity and near-unity permeability, exhibits a comparatively low wave impedance and therefore a high reflection loss R_{dB} . Its negligible conductivity results in minimal absorption at low frequencies, while the multiple-reflection correction term B_{dB} almost completely compensates the reflection loss. As frequency increases, the growing electrical thickness of the sheet reduces the negative contribution of the multiple-reflections term B_{dB} while the dielectric loss tangent $\tan \delta$ gives rise to an increasing absorption contribution A_{dB} , leading to a gradual improvement in shielding effectiveness with frequency.

6.2 Dual TEM cell

A simulation model of two coupled TEM cells, as shown in Figure 3.14, is constructed based on the individual cell model presented in Section 5.1.2. The aperture separating the two cells is modeled as an empty square opening with a side length of $d = 10$ mm, ensuring that it remains electrically small up to a frequency of approximately 3 GHz. To achieve accurate results, sufficient mesh resolution in the aperture region is critical, as highlighted in Section 5.1.4. Accordingly, 10 to 15 mesh elements across the aperture

width are maintained throughout all simulations. Following the procedure outlined in Section 3.6.4, the electric and magnetic shielding effectiveness of ferrite, barium titanate, and silver are derived.

Port 1 excites the TEM cell with a constant input power of 1 W. The sum P_{sum} and difference P_{diff} of the powers received at ports 3 and 4 are then computed following [32] as

$$P_{\text{sum}} = (a + b)(a + b)^*, \quad (6.1a)$$

$$P_{\text{diff}} = (a - b)(a - b)^*, \quad (6.1b)$$

where a and b are the complex field amplitudes at ports 3 and 4, respectively. Evaluated for an empty aperture, these quantities serve as the reference values $P_{\text{ref,sum}}$ and $P_{\text{ref,diff}}$ required to compute the electric and magnetic shielding effectiveness according to (3.68a) and (3.68b). They are shown against frequency in Figure 6.2.

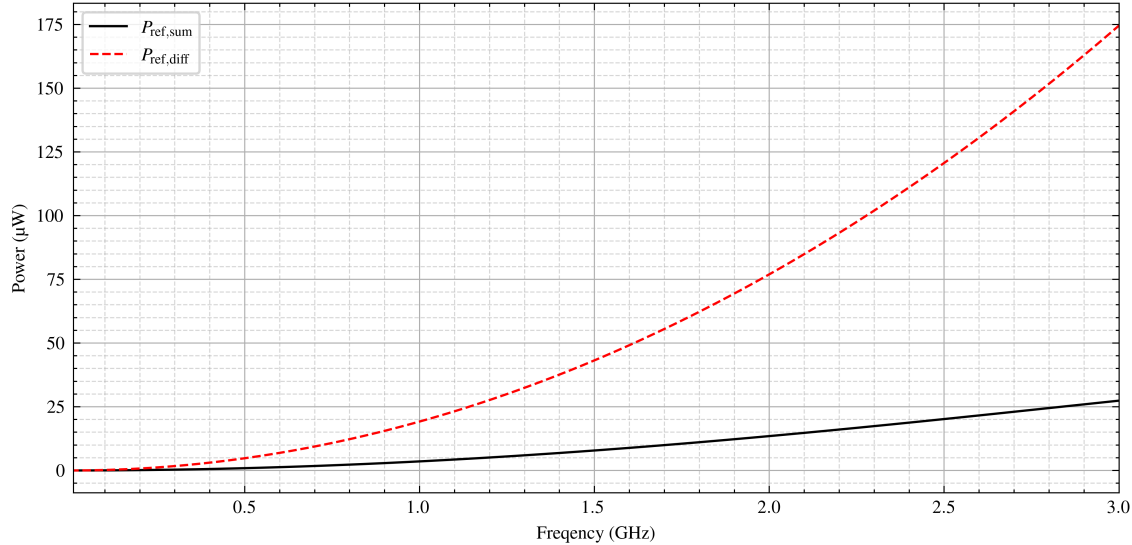


Figure 6.2 The sum $P_{\text{ref,sum}}$ and difference $P_{\text{ref,diff}}$ of the reference power, measured with an empty aperture and calculated with phase information considered.

The aperture is then filled with each shielding material under investigation in turn, with a material thickness of $t = 10 \mu\text{m}$. The sum $P_{\text{load,sum}}$ and difference $P_{\text{load,diff}}$ of the powers at ports 3 and 4 are computed and used as the load power to derive the electric and magnetic shielding effectiveness of each material according to (3.68a) and (3.68b). The derived powers for all investigated materials are shown against frequency in Figures 6.3a and 6.3b.

The distinction between electric and magnetic shielding effectiveness is particularly significant in the near-field regime, where the wave impedance of the source field deviates substantially from the free-space impedance η_0 . Electric near-field sources produce high-impedance fields, whereas magnetic near-field sources produce low-impedance fields, as mentioned in Section 3.6.1. The shielding performance of a material depends not only on its electric properties but also on the degree of impedance mismatch between the material and the incident near-field, as expressed by (3.59).

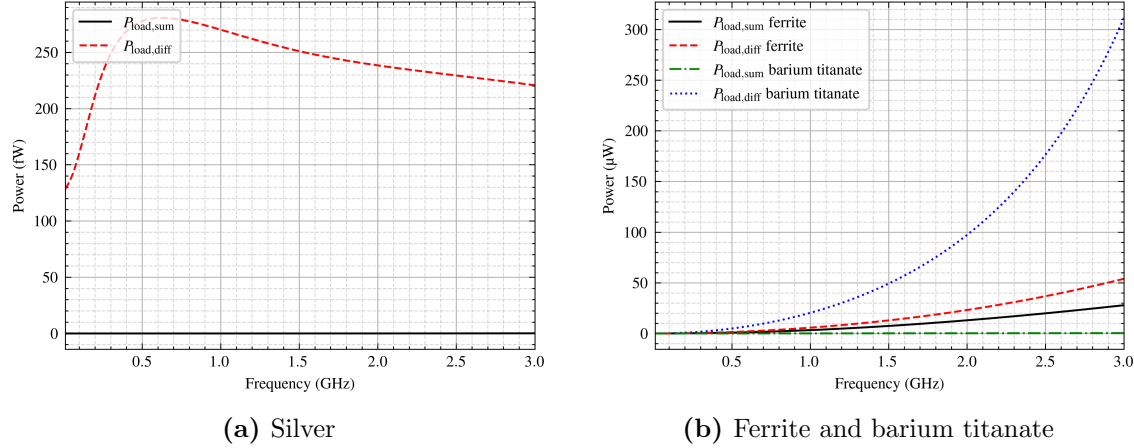


Figure 6.3 The sum $P_{\text{load,sum}}$ and difference $P_{\text{load,diff}}$ of the output power measured at ports 3 and 4 with phase information considered.

Ferrite exhibits higher power transfer than barium titanate, indicating lower overall shielding effectiveness. For both materials, the power transfer increases with frequency, which can be attributed to their low bulk conductivity. Silver, by contrast, exhibits power transfer several orders of magnitude lower and is therefore presented in a separate plot for clarity. The resulting electric and magnetic shielding effectiveness spectra are shown in Figure 6.4.

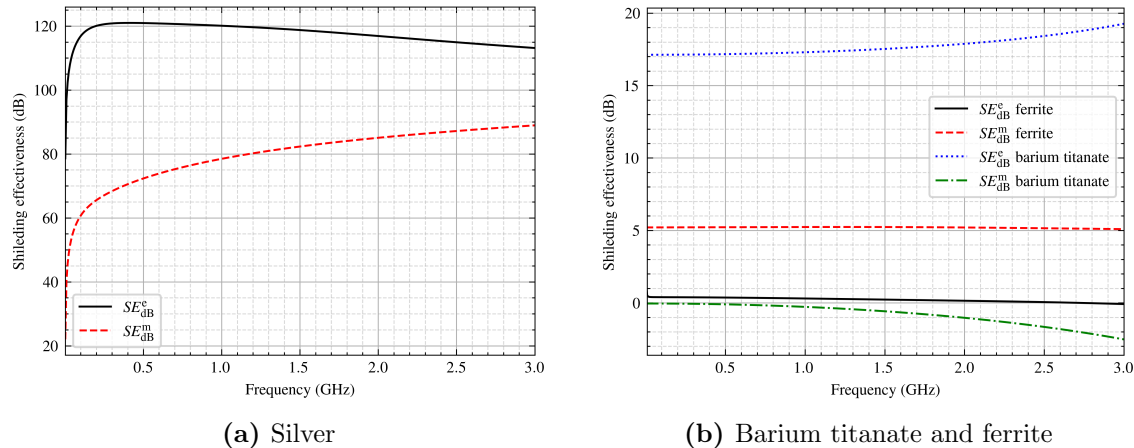


Figure 6.4 Electric SE_{dB}^e and magnetic SE_{dB}^m shielding effectiveness of (a) silver and (b) barium titanate and ferrite, derived according to (3.68a) and (3.68b).

Barium titanate exhibits good electric shielding characteristics but a negative SE_{dB}^m , indicating poor magnetic shielding. Negative magnetic shielding effectiveness values are physically possible and arise from interference effects at the loaded aperture, which cause the field amplitude a and the received power at port 3 to increase [38, 16, p. 63]. The high relative permittivity of barium titanate lowers its material wave impedance (see (3.60)), increasing the impedance mismatch with high-impedance electric source fields

and thereby yielding a high electric shielding effectiveness. Conversely, this low material wave impedance reduces the mismatch with low-impedance magnetic near-field sources, which accounts for the poor and eventually negative magnetic shielding effectiveness with increasing frequency.

Ferrite, on the other hand, demonstrates a higher magnetic shielding effectiveness SE_{dB}^m but a low or negative electric shielding effectiveness SE_{dB}^e . Its high relative permeability raises the material wave impedance (see (3.60)), enhancing reflections of incident magnetic near-fields whose low wave impedance results in a large mismatch at the material surface. However, this elevated material wave impedance reduces the mismatch with high-impedance electric source fields, rendering ferrite a poor electric shield.

Silver demonstrates the highest overall shielding effectiveness among the materials investigated. Its high conductivity produces a very low material wave impedance, which leads to a strong impedance mismatch with electric near-field sources, as discussed in Section 6.1. At low frequencies, the magnetic shielding effectiveness increases monotonically across the inspected frequency range, driven by the growing absorption contribution as the skin depth decreases steeply (see (3.61)). The electric shielding effectiveness, by contrast, begins to decline at higher frequencies, as the wave impedance of the material surface increases toward that of the high-impedance electric source field, reducing the impedance mismatch and the associated reflection loss R_{dB} in accordance with (3.59).

6.3 Antennas in shield enclosure

Following the near-field shielding investigations, the loop and monopole antennas from Sections 5.2 and 5.3 placed inside a hollow cubic enclosure are examined, as shown in Figures 6.5a and 6.5b. The enclosure has a wall thickness of 10 μm and a side length of 6 mm.

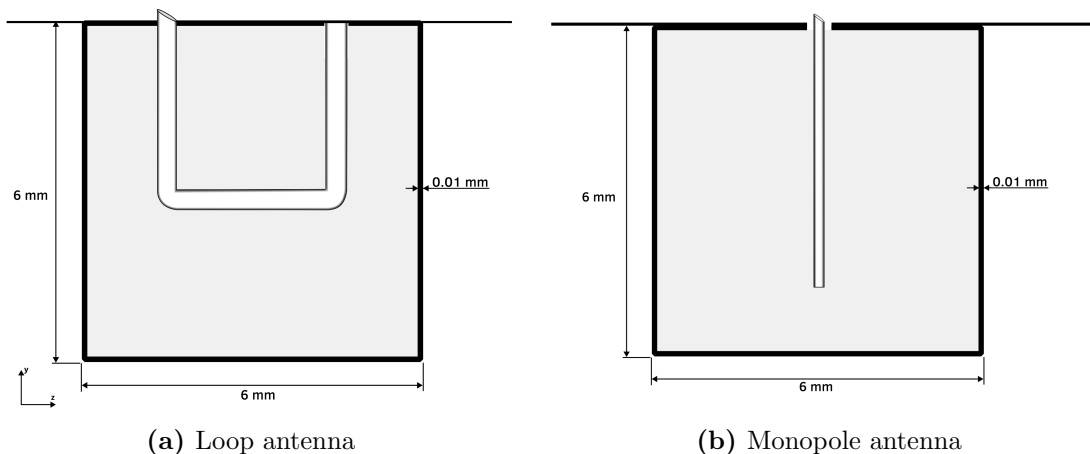


Figure 6.5 Investigated antennas placed inside a hollow cubic enclosure within the TEM cell.

Figure 6.6a shows the radiated power from the antennas with and without a barium titanate enclosure. The output power of the loop antenna increases because the barium

titanate enclosure capacitively loads the antenna, resulting in a reduction of the resonance frequency. This effect shifts the antenna toward a more efficient operating point within the investigated frequency range, as discussed in Section 5.3. In contrast, the enclosure effectively shields the radiation of the monopole antenna. These results are consistent with the near-field of the monopole antenna being predominantly electric, as given in (2.11), while that of the loop antenna is predominantly magnetic, as given in (2.19), and are in agreement with the near-field shielding investigations presented in Section 6.2.

Figure 6.6b shows the corresponding radiated power for the ferrite enclosure. Here, the roles of the two antennas are reversed. The output power of the monopole antenna increases due to the ferrite enclosure inductively loading the antenna, while the loop antenna's radiation is attenuated.

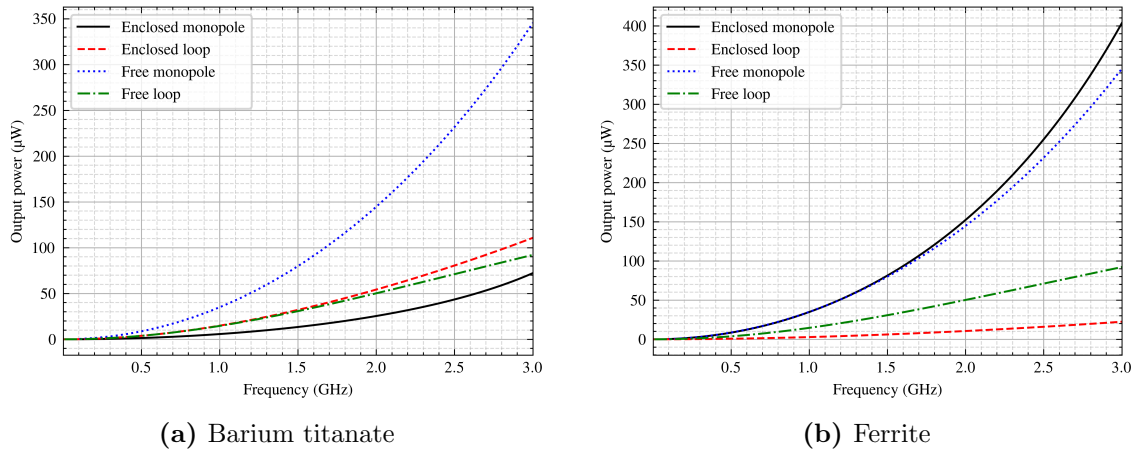


Figure 6.6 Radiated power as a function of frequency for the loop and monopole antennas with and without enclosure.

The influence of enclosure wall thickness on the radiated power is examined in Figure 6.7, where silver is now additionally included as a shielding material. As expected, increasing the wall thickness reinforces the shielding effects observed in Figure 6.6. Silver yields the lowest power transfer among all investigated materials, consistent with the high shielding effectiveness found and discussed in Sections 6.1 and 6.2. The output power of the monopole antenna within the silver enclosure increases with frequency, which is associated with the declining electric shielding effectiveness at higher frequencies. Conversely, the loop antenna produces less output power with increasing frequency, consistent with the monotonically increasing magnetic shielding effectiveness of silver.

Additionally, resonances are observed for thick enclosures, manifesting as a pronounced peak in the transmitted power at approximately 2.5 GHz for the barium titanate enclosure with a wall thickness of 100 μm . A similar trend is observed for the thickest ferrite enclosure, where the resonance frequency lies just outside the investigated frequency range. As shown in Figure 6.8, this effect corresponds to a half-wavelength resonance established within the enclosure cavity. The excitation of such resonant waves requires, among other things, that internal reflections are not fully suppressed. This proposition in turn demands that the multiple-reflection correction term B_{dB} remains sufficiently small in magnitude,

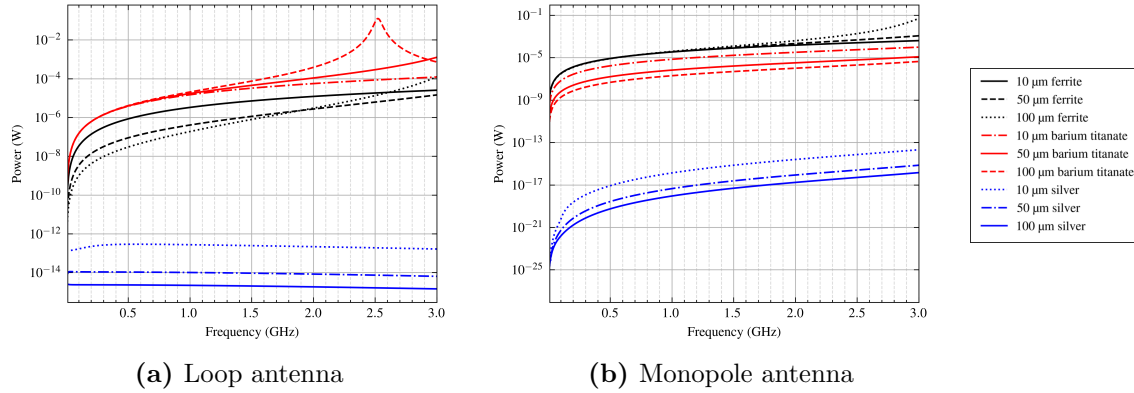


Figure 6.7 Radiated power as a function of frequency for the loop and monopole antennas with varying enclosure wall thickness.

as discussed in Section 3.6.1. A larger wall thickness supports this condition by increasing the electrical thickness of the enclosure walls.

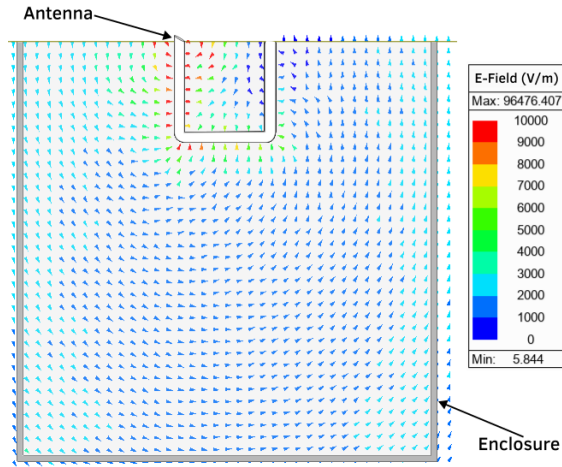


Figure 6.8 Electric near-field distribution of the loop antenna at the resonance frequency of 2.5 GHz, with a barium titanate shielding enclosure of 100 μm wall thickness.

6.4 Dipole moments in shield enclosure

Replacing electrically small antennas with equivalent dipole moments inside shielding enclosures enables investigation of shielding performance with reduced computational effort. For this purpose, the equivalent dipole moments of the monopole and loop antennas derived in Sections 5.2.2 and 5.3.2 are used in place of the full antenna models within the enclosures depicted in Figure 6.5. The radiated power produced by these dipole moments for different enclosure materials at a constant material thickness of $10\text{ }\mu\text{m}$ is shown in Figure 6.9.

The dipole approximation agrees well with the full antenna model for the loop antenna in barium titanate and for the monopole antenna in ferrite. As the shielding effectiveness of

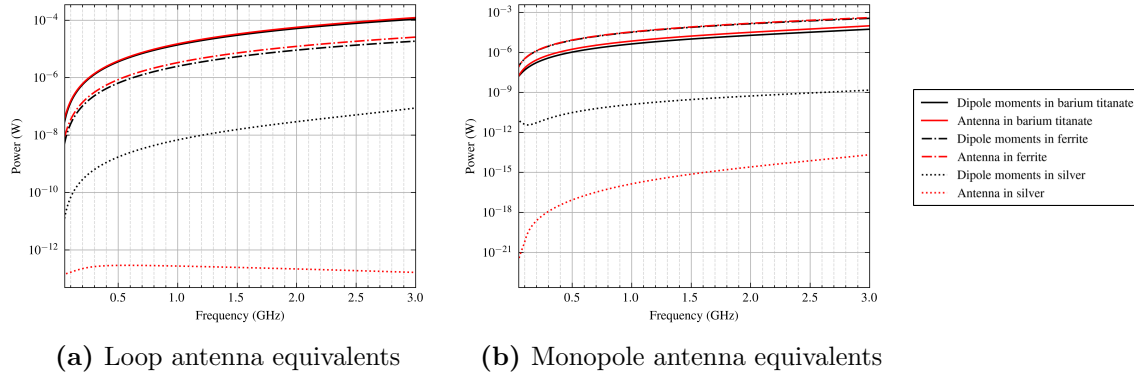


Figure 6.9 Radiated power as a function of frequency for the loop and monopole antenna equivalent dipole moments in enclosures of different materials at a constant wall thickness of 10 µm.

the enclosure material increases relative to the respective antenna, however, the accuracy of the approximation decreases, indicating that the equivalent dipole moments must be adjusted accordingly to account for the interaction between the source and the enclosure.

7 Conclusion

This thesis presents investigations of electrically small antennas and their coupling with a TEM cell using the finite element method. It further discusses applications of the framework created.

In this thesis, dipole moments equivalent to the electrically small antennas are calculated, whose magnitudes directly correlate with the electric and magnetic coupling of the antenna with the TEM cell. It finds, that the electric dipole moment correlates directly to the displacement current towards the septum, and the magnetic dipole moment to the voltage induced on the septum. An equivalent circuit model, both for capacitive and inductive antennas coupling to the TEM cell, is developed.

The relation of different geometrical and electrical antenna parameters to the equivalent dipole moments is investigated. An increase in Q-factor or decrease in resonance frequency of the antenna has been found to increase non-linear dipole moments frequency-behavior. The electric dipole moment generated by an antenna increases primarily with its physical height, due to increased displacement currents toward the septum. The magnetic dipole moment increases with the loop area normal to the magnetic field intensity of a propagating mode in the TEM cell. If the loop is not closed, a magnetic dipole moment can still exist due to curling electric field intensities $\nabla \times \mathbf{E} \neq 0$ forming perpendicular to the magnetic field intensity.

Further research could involve the measurement of such antennas with a real TEM cell, or the numerical analysis with other waveguides, such as the IC stripline. The framework in this thesis could be used to increase EMC of electronic systems containing electrically small, radiating structures, or represent them with dipole moments for less computational effort in complex simulation models.

References

- [1] George B. Arfken, Hans-Jurgen Weber, and Frank Harris. *Mathematical methods for physicists*. Academic, 2013.
- [2] Constantine A. Balanis. *Advanced Engineering Electromagnetics*. John Wiley Sons, 2012.
- [3] Constantine A. Balanis. *Antenna theory: Analysis and design*. Buch Constantine A. Balanis. 3rd. Wiley, 1997.
- [4] C. Buccella et al. “Magnetic field computation in a physically large domain with thin metallic shields”. In: *IEEE Transactions on Magnetics* 41.5 (2005), pp. 1708–1711. DOI: 10.1109/TMAG.2005.846059.
- [5] Z. Cendes and D. Shenton. “Adaptive mesh refinement in the finite element computation of magnetic fields”. In: *IEEE Transactions on Magnetics* 21.5 (1985), pp. 1811–1816. DOI: 10.1109/TMAG.1985.1063929.
- [6] Z.J. Cendes. “Vector finite elements for electromagnetic field computation”. In: *IEEE Transactions on Magnetics* 27.5 (1991), 3958–3966. DOI: 10.1109/20.104970.
- [7] Z.J. Cendes and J.-F. Lee. “The transfinite element method for modeling MMIC devices”. In: 1988., *IEEE MTT-S International Microwave Symposium Digest* (1988), 623–626. DOI: 10.1109/mwsym.1988.22111.
- [8] Robert E. Collin. *Field theory of guided waves*. IEEE Press, 2015.
- [9] Saju Daniel and Sabu Thomas. “Shielding Efficiency Measuring Methods and Systems”. In: *Advanced Materials for Electromagnetic Shielding: Fundamentals, Properties, and Applications*. 2019, pp. 61–87. DOI: 10.1002/9781119128625.ch4.
- [10] Alexander V. Demakov and Maxim E. Komnatnov. “TEM cell for Testing Low-profile Integrated Circuits for EMC”. In: *2020 21st International Conference of Young Specialists on Micro/Nanotechnologies and Electron Devices (EDM)*. 2020, pp. 154–158. DOI: 10.1109/EDM49804.2020.9153508.
- [11] David J. Griffiths. *Introduction to electrodynamics*. Cambridge University Press, 2024.
- [12] C. Groh et al. “TEM waveguides for EMC measurements”. In: *IEEE Transactions on Electromagnetic Compatibility* 41.4 (1999), pp. 440–445. DOI: 10.1109/15.809846.
- [13] Robert C. Hansen and Robert E. Collin. *Small antenna handbook*. Wiley, 2013.
- [14] K.H. Huebner et al. *The Finite Element Method for Engineers*. A Wiley-Interscience publication. Wiley, 2001. ISBN: 9780471370789. URL: <https://books.google.at/books?id=f3MZE1BYq3AC>.
- [15] John David Jackson. *Classical Electromagnetism*. 2nd ed. Wiley.
- [16] Maciej Wladyslaw Jaroszewski, Sabu Thomas, and Ajay V. Rane. *Advanced materials for electromagnetic shielding: Fundamentals, properties, and applications*. Wiley, 2019.
- [17] J.P. Karst, C. Groh, and H. Garbe. “Calculable field generation using TEM cells applied to the calibration of a novel E-field probe”. In: *IEEE Transactions on Electromagnetic Compatibility* 44.1 (2002), pp. 59–71. DOI: 10.1109/15.990711.
- [18] M. Koch, C. Groh, and H. Garbe. “Exact Determination of Resonant Frequencies in TEM Cells”. In: *13th International Zurich Symposium and Technical Exhibition on Electromagnetic Compatibility*. 1999, pp. 653–658. DOI: 10.23919/EMC.1999.10791592.

- [19] Galen H Koepke. "Theory and measurements of radiated emissions using a TEM cell". In: (1989). DOI: 10.6028/nist.tn.1326.
- [20] Dominik Kreindl et al. "A Simulation Workflow for Predicting IC Stripline Radiated Emissions of Bond Wire-Based Systems". In: *2024 14th International Workshop on the Electromagnetic Compatibility of Integrated Circuits (EMC Compo)*. 2024, pp. 69–73. DOI: 10.1109/EMCCompo61192.2024.10742020.
- [21] Dominik Kreindl et al. "Evaluation of an analytical equivalent Hertzian dipole representation in tem cells applying the finite element method". In: *IEEE Transactions on Magnetics* 60.3 (2024), 1–4. DOI: 10.1109/tmag.2023.3324698.
- [22] Dominik Kreindl et al. "Measurement and Simulation Methodology for Characterizing the Shielding Effectiveness of Coating Materials for Optical Sensors". In: *2023 International Symposium on Electromagnetic Compatibility – EMC Europe*. 2023, pp. 1–6. DOI: 10.1109/EMCEurope57790.2023.10274360.
- [23] Ján Kruželák et al. In: *Electrical conductivity, EMI absorption shielding performance, curing process and mechanical properties of rubber composites* (2024). DOI: 10.20944/preprints202401.1547.v1.
- [24] J.-F. Lee, D.-K. Sun, and Z.J. Cendes. "Full-wave analysis of dielectric waveguides using tangential vector finite elements". In: *IEEE Transactions on Microwave Theory and Techniques* 39.8 (1991), pp. 1262–1271. DOI: 10.1109/22.85399.
- [25] J.F. Lee, D.K. Sun, and Z.J. Cendes. "Tangential vector finite elements for electromagnetic field computation". In: *IEEE Transactions on Magnetics* 27.5 (1991), pp. 4032–4035. DOI: 10.1109/20.104986.
- [26] M.F.N. Mohsen. "Some details of the Galerkin Finite Element Method". In: *Applied Mathematical Modelling* 6.3 (1982), 165–170. DOI: 10.1016/0307-904x(82)90005-1.
- [27] Cristian MORARI and Cristian BĂLAN. In: *Methods for determining shielding effectiveness of materials* (2015).
- [28] H. Taconi D. Gravino N. Disages K. Mojail H.R. Mira and P.K. Nestaris. "Understanding Capacitance and Inductance in Antennas". In: *National Journal of Antennas and Propagation* 4.2 (2022). DOI: 10.31838/njap/04.02.07.
- [29] Clayton R. Paul, Robert C. Scully, and Mark A. Steffka. *Introduction to electromagnetic compatibility*. Wiley, 2023.
- [30] S. A. Schelkunoff. "The impedance concept and its application to problems of reflection, refraction, shielding and power absorption". In: *Bell System Technical Journal* 17.1 (1938), 17–48. DOI: 10.1002/j.1538-7305.1938.tb00774.x.
- [31] D. Shenton and Z. Cendes. "Three-dimensional finite element mesh generation using Delaunay tessellation". In: *IEEE Transactions on Magnetics* 21.6 (1985), 2535–2538. DOI: 10.1109/tmag.1985.1064165.
- [32] Ippalapalli Sreenivasiah, David Chang, and Mark Ma. "Emission characteristics of electrically small radiating sources from tests inside a tem cell". In: *IEEE Transactions on Electromagnetic Compatibility* EMC-23.3 (1981), 113–121. DOI: 10.1109/temc.1981.303930.
- [33] GILBERT STRANG. *Analysis of the finite element method*. WELLESLEY-CAMBRIDGE Press, 2018.

- [34] John C Tippet, David C Chang, and Myron L Crawford. In: *An analytical and experimental determination of the cutoff frequencies of higher-order te modes in a Tem cell* (1976). DOI: 10.6028/nbs.ir.76-841.
- [35] C.M. Weil and L. Gruner. “High-order mode cutoff in rectangular striplines (short papers)”. In: *IEEE Transactions on Microwave Theory and Techniques* 32.6 (1984), 638–641. DOI: 10.1109/tmtt.1984.1132745.
- [36] Perry F Wilson. “Excitation of a tem cell by a vertical electric Hertzian dipole”. In: (1981). DOI: 10.6028/nbs.tn.1037.
- [37] Perry F. Wilson, David C. Chang, and Mark T. Ma. “Input Impedance of a Probe Antenna in a TEM Cell”. In: *IEEE Transactions on Electromagnetic Compatibility* EMC-26.4 (1984), pp. 154–161. DOI: 10.1109/TEMC.1984.304216.
- [38] Perry F. Wilson and Mark T. Ma. “Shielding-Effectiveness Measurements with a Dual TEM Cell”. In: *IEEE Transactions on Electromagnetic Compatibility* EMC-27.3 (1985), pp. 137–142. DOI: 10.1109/TEMC.1985.304277.
- [39] Perry F. Wilson and Mark T. Ma. “Simple approximate expressions for higher order mode cutoff and resonant frequencies in TEM cells”. In: *IEEE Transactions on Electromagnetic Compatibility* 28.3 (1986), 125–130. DOI: 10.1109/temc.1986.4307269.